Time-Resolved Microscopy of Near-Infrared to Visible Waveforms

Mikhail Mamaikin

München 2020

Time-Resolved Microscopy of Near-Infrared to Visible Waveforms

Mikhail Mamaikin

Dissertation
an der Fakultät für Physik
der Ludwig–Maximilians–Universität
München

vorgelegt von
Mikhail Mamaikin
aus Cheboksary, Russland

München, den 27.04.2020

Contents

Abstract

Laser pulses, since their first demonstration in 1960, have reached an unprecedented level of temporal confinement: light fields on a femtosecond timescale are widely available and routine in modern experiments. Nowadays, ultrashort few-cycle electric fields can be utilized to generate even shorter, attosecond (1×10^{-18} s) pulses, establishing a new direction of optics called attosecond physics. Such short light localization provides incredibly high temporal resolution, enabling direct observation of sub-cycle dynamics of the interaction of the fundamental waveform with matter in pump-probe measurements. Generation of attosecond pulses is an extremely sophisticated task, involving highly nonlinear processes and requiring a vacuum environment. Therefore, free-space methods that allow for the reconstruction of the time-varying field oscillations and direct performance of experiments with attosecond temporal precision are being developed.

As the electric field is a function of time and space, the time-varying component is not always able to fully characterize the pulse. The large bandwidth associated with ultrashort pulses can be a reason for the formation of harmful spatio-temporal distortions. They often lead to a significant peak intensity reduction and unexpected experimental outcomes. The lack of direct access to the spatio-temporal evolution of near-infrared and visible few-cycle pulses is indeed of great concern. A potential spatio-temporal metrology technique can not only detect various distortions but also probe the properties of spatially inhomogeneous samples, extending the field-resolved spectroscopic toolbox to include spatial dimensions.

This dissertation aims to advance a revolutionary metrology approach for absolute space-time characterization of electric fields by extending its capacity to the near-infrared and visible spectral regions. Its application in microscopy yields detection of subwavelength-localized structures in a wide-field geometry and extraction of spatio-temporal light-matter interaction with sub-cycle temporal resolution.

This work is based on a well-established technique for complete field reconstruction, referred to as *electro-optic sampling*. The concept of electro-optic sampling relies on a phase-stable test field to be sampled that is coincident with an ultrashort probe pulse in an electro-optic crystal. Their nonlinear interaction induces a polarization rotation of the probe pulse that is sensitive to the strength and sign of the test electric field at a given instant. By varying the time delay between the pulses and employing dedicated instruments to read out the polarization rotation, it is possible to completely reconstruct the test field. Such instruments typically average over the spatial variations of the polarization rotation, yielding a single temporal waveform. Therefore, the assumption about homogeneous spatial distribution of the investigated field has to be made in these measurements.

Alternatively, the dependence of the polarization rotation on the spatial coordinates in electro-optic sampling can be recorded using a standard imaging system. In this case, absolute spatio-temporal field information about the test electric field including the carrier envelope phase can be measured. We refer to this technique as *electro-optic imaging*.

The optical scheme for electro-optic imaging was first introduced with relatively long pulses, in the terahertz spectral range (0.1-10 THz). In the present thesis, we dramatically extend the detection limits of electro-optic imaging towards shorter wavelengths, as low as 670 nm (450 THz). For the first time, the imaging technique is applied to demonstrate the full spatio-temporal reconstruction of few-cycle pulses in the near-infrared and visible regimes. Arbitrary spatio-temporal distortions of the laser pulses are detected and analyzed by converting time-dependent field snapshots into a hyperspectral image.

Direct access to spatio-temporal dynamics of the electric field is utilized to investigate innovative metasurface optical devices and their incredible control over light properties. Metasurface optics allow diffraction-limited performance to be realized without cumbersome optical designs. The imaging apparatus can open a new door to comprehensive studies of absolute space-time light confinement after the interaction of metasurface optics with an incident broadband field.

It is particularly intriguing that not only the far-field but also near-field radiation can be accessed with electro-optic imaging in real time. This has been demonstrated in terahertz range, where microscopic samples placed directly on a thin electro-optic crystal were imaged with subwavelength resolution. A proof-of-concept of near-field detection in the near-infrared range is shown by utilizing field enhancement with spherical microparticles.

The imaging apparatus presented in this dissertation is expected to enrich the tools of attosecond metrology by including spatial dimensions. Additionally, this field-resolved microscopy method opens a novel path towards wide-field hyperspectral and label-free imaging with subwavelength resolution for applications in nanoscience and biology.

Zusammenfassung

Seit ihrer ersten Demonstration im Jahr 1960 haben Laserpulse ein noch nie dagewesenes Niveau der zeitlichen Begrenzung erreicht: Lichtfelder auf der Zeitskala von Femtosekunden sind weithin verfügbar und in modernen Experimenten Routine. Solche ultrakurze elektrische Felder mit nur wenigen Schwingungszyklen können z.B. dazu genutzt werden, um noch kürzere Pulse, Attosekunden-Pulse (1×10^{-18} s), zu erzeugen, wodurch eine neue Richtung der Optik etabliert wurde, die Attosekunden-Physik. Eine solche kurze Lichtlokalisierung bietet eine extrem hohe zeitliche Auflösung und ermöglicht die direkte Beobachtung der Subzyklus-Dynamik zwischen Licht und Materie mit Hilfe von Pump-Probe-Messungen. Die Erzeugung von Attosekunden-Pulsen ist eine äußerst anspruchsvolle Aufgabe, die hochgradig nichtlineare Prozesse beinhaltet und eine Vakuumumgebung erfordert. Daher werden Techniken entwickelt, die die Rekonstruktion der zeitvariablen Feldschwingungen und die direkte Durchführung von Experimenten mit Attosekunden-Zeitgenauigkeit in Normalbedingungen ermöglichen.

Da das elektrische Feld eine Funktion von Zeit und Raum ist, kann eine Reduktion auf die zeitliche Komponente alleinden Laserpuls im Allgemeinen nicht vollständig charakterisieren. Die große Bandbreite, die mit ultrakurzen Pulsen einher geht, kann ein Grund für die Bildung von störenden raum-zeitlichen Verzerrungen sein. Diese können zu einer signifikanten Verringerung der Spitzenintensität und zu unerwarteten experimentellen Ergebnissen führen. Das nicht Vorhanden sein einer Möglichkeit die raum-zeitlichen Entwicklung von ultrakurzen Pulsen im nahen Infrarot und Sichtbaren direkt zu bestimmen ist bedauernswert. Eine solche raum-zeitliche Messtechnik könnte nicht nur verschiedene Verzerrungen quantifizieren, sondern erlaubt es auch die Eigenschaften räumlich inhomogener Proben auf die Pulse zu untersuchen und erweitert die feldaufgelöste spektroskopische Toolbox auf die räumliche Ausdehnung der Pulse.

Ziel dieser Dissertation ist die Weiterentwicklung eines revolutionären Ansatzes zur absoluten Raum-Zeit-Charakterisierung elektrischer Felder, wobei seine Kapazität auf den nahen Infrarot- und Sichtbaren Spektralbereich ausgedehnt werden soll. Seine Implementierung in der Mikroskopie ermöglicht die Detektion von subwellenlängen-lokalisierten Strukturen in einer Weitfeldgeometrie und die Extraktion von raum-zeitlicher Licht-Materie-Wechselwirkung mit subzyklischer zeitlicher Auflösung.

Diese Arbeit basiert auf einer weit verbreiteten Technik zur vollständigen Feldrekonstruktion, die als *elektro-optische Abtasten* bezeichnet wird. Das Konzept des elektro-optischen Abtastens beruht auf einem phasenstabilen Testfeld, das mit einem ultrakurzen Abfragepuls in einem elektro-optischen Kristall koinzidierend vermessen wird. Ihre nicht-

lineare Wechselwirkung induziert eine Polarisationsdrehung des Abfragepulses, die proportional zur Stärke und Richtungs des vorliegenden elektrischen Testfeldes ist. Durch Variation der Zeitverzögerung zwischen den Pulsen und durch den Einsatz spezieller Instrumente zum Auslesen der Polarisationsdrehung ist es möglich, das Testfeld vollständig zu rekonstruieren. Typischerweise mitteln solche Instrumente über die räumlichen Verteilung der Polarisationsdrehung, was zu einer einzigen zeitlichen Wellenform führt. Daher muss bei diesen Messungen die Annahme einer homogenen räumlichen Verteilung des untersuchten Feldes getroffen werden.

Alternativ kann die Abhängigkeit der Polarisationsdrehung von den Raumkoordinaten bei der elektro-optischen Abtastung mit einem Standard-Bildgebungssystem aufgezeichnet werden. In diesem Fall kann die absolute raum-zeitliche Feldinformation über das elektrische Testfeld einschließlich der Phase zur Einhüllenden gemessen werden. Wir bezeichnen diese Technik als *elektro-optische Bildgebung.*

Das optische Schema für die elektro-optische Bildgebung wurde zuerst mit relativ langen Pulsen im Terahertz-Spektralbereich (0.1-10 THz) eingeführt. In der vorliegenden Arbeit erweitern wir die Nachweisgrenze der elektro-optischen Bildgebung dramatisch in Richtung kürzerer Wellenlängen, bis hinunter zu 670 nm (450 THz). Erstmals wird die bildgebende Technik dazu benutzt, um die vollständige räumlich-zeitliche Rekonstruktion von Impulsen mit wenigen Zyklen im nahen Infrarot und im sichtbaren Bereich zu demonstrieren. Beliebige räumlich-zeitliche Verzerrungen der Laserpulse werden durch die Umwandlung zeitabhängiger Feldaufnahmen in ein hyperspektrales Bild detektiert und analysiert.

Mit der direkten Charakterisierung der raum-zeitlichen Dynamik des elektrischen Feldes werden innovative Optiken, mit metastrukturierte Oberflächen, und deren unglaubliche Kontrolle über die Lichteigenschaften untersucht. Diese sogenannten Metasurface-Optiken erlauben beugungsbegrenzte Abbildungen durch eine einzige optische Komponente. Die elektro-optische Bildgebung bereitet den Weg zu umfassenden Untersuchungen der absoluten Raum-Zeit-Lichtverteilung eines breitbandigen einfallenden Lichtfeldes nach der Wechselwirkung mit der Metasurface-Optik.

Besonders faszinierend ist, dass nicht nur die Fernfeld-, sondern auch die Nahfeldstrahlung mit der elektro-optischen Bildgebung in Echtzeit zugänglich ist. Dies wurde im Terahertz-Bereich demonstriert, wenn mikroskopische Proben, die direkt auf einem dünnen elektro-optischen Kristall platziert sind, nicht beugungslimitiert abgebildet wurden. Ein proof-of-concept der Nahfelddetektion im nahen Infrarotbereich wird durch die Nutzung der Felderhöhung mit sphärischen Mikropartikeln gezeigt.

Der in dieser Dissertation vorgestellte bildgebende Apparat bereichert die Werkzeuge der Attosekunden-Metrologie durch die zusätzliche räumliche Auflösung. Darüber hinaus eröffnet diese feldaufgelöste mikroskopische Methode eine neue Möglichkeit einer hyperspektralen und markierungsfreien nicht beugungslimitierten Weitfeld-Bildgebung für Anwendungen in den Nanowissenschaften und der Biologie.

List of Abbreviations

AOPDF	acousto-optic programmable dispersive filter
BBO	beta-barium borate, β-BaB$_2$O$_4$
CCD	charge-coupled device
CEP	carrier envelope phase
CPA	chirped pulse amplification
DFG	difference-frequency generation
EOI	electro-optic imaging
EOS	electro-optic sampling
FL	focal length
FROG	frequency-resolved optical gating
FWHM	full width at half maximum
GDD	group-delay dispersion
GVD	group-velocity dispersion
HCF	hollow-core fiber
HHG	high harmonic generation
IR	infrared
LO	local oscillator
NA	numerical aperture
NIR	near-infrared
NPS	nonlinear photoconductive sampling
OPA	optical parametric amplification
OPCPA	optical parametric chirped pulse amplification
PPLN	periodically polled lithium niobate
SEM	scanning electron microscope
SFG	sum-frequency generation
SHG	second-harmonic generation
SNR	signal-to-noise ratio
STC	spatio-temporal coupling
TFP	thin-film polarizer

Ti:Sa	titanium-doped sapphire, $Ti^{3+}:Al_2O_3$
UV	ultraviolet
XFROG	cross-correlation frequency-resolved optical gating
XUV	extreme ultraviolet
Yb:YAG	ytterbium-doped yttrium aluminum garnet, $Yb^{3+}:Y_3Al_5O_{12}$
WGP	wire-grid polarizer

List of Figures

Introduction

We live in a distinctive universe, where every object has specific spatial dimensions and evolves in the temporal dimension. Unfortunately, an unaided human eye is not capable of detecting tiny objects of the micro- and nanoworld with typical sizes less than 0.1 mm. Thousands of years ago, Egyptians discovered that the fragments of crystal or obsidian can be used to better view small items. It is also well known that the Roman Emperor Nero utilized gemstones to distantly watch the performance of actors on a stage. The first magnifying glass for the scientific purpose is considered to be developed by the English philosopher Roger Bacon in the thirteenth century. He was a lecturer at Oxford University, who additionally described the properties of the convex lens and the basic laws of refraction and reflection. At that moment, lenses were primarily utilized to study tiny insects, reasonably called "flea glasses". Already in the sixteenth century, the first primitive microscope as well as the first telescope were invented by arranging multiple lenses. This gave a huge boost to formation of the new field of science called microscopy.

Nowadays, microscopy embraces three well-established branches: optical, electron, and scanning probe microscopy. The successor of the oldest design, an optical microscope is based on the traditional light imaging system, providing spatial resolution confined by the diffraction limit of light. A more advanced configuration with higher resolving power is an electron microscope, the first prototype of which was created in 1931 by Ernst Ruska. The concept relies on the use of a beam of accelerated electrons rather than photons, bombarding a sample in vacuum. Electrons allow the spatial resolution to be dramatically improved, successfully resolving objects less than 1 nm [1]. Instead of the conventional glass lenses, the electrons are focused by shaped electromagnetic fields to produce the lensing effect. The third microscopy direction, scanning probe microscopy, was established with the invention of the first scanning tunnelling microscope in 1981 by Gerd Binnig and Heinrich Rohrer (the Nobel laureates in Physics 1986, jointly with Ernst Ruska) [2]. The approach relies on raster probe scanning of sampled surfaces using a sharp tip on very small distances from the surface. The resolving capabilities are mainly determined by the tip dimensions, providing a resolution that is significantly lower than the diffraction limit. Currently, alternative super-resolution techniques are of great interest in light microscopy like state-of-the-art approaches based on STED, PALM or SIM [3–5].

On the other hand, a fundamental tool to explore natural properties of matter such as physical structure, composition, etc., is spectroscopy. Access to rich information about material features can be obtained in the time domain using coherent irradiation. Time-domain spectroscopy is one of the most promising routes to probe the properties of matter,

utilizing a direct comparison of an incident electric field and modifications that a sample encoded into the amplitude and phase of the transmitted pulse [6–8]. With an ability to observe field oscillations on a femtosecond timescale, a variety of novel research directions related to the study of fundamental light-matter interaction have been formed. As the underlying interaction is usually confined to one oscillation cycle, time-domain metrology techniques with sub-cycle temporal resolution have been introduced [9, 10]. Previously, direct access to rapidly oscillating fields from the near-infrared to ultraviolet has relied on exploitation of high harmonic generation [11] or tunnel ionization [12], which provide attosecond temporal precision. At present, the technological progress has reached an unprecedented degree when attosecond metrology involves only a simple table-top setup [13].

A reasonable question can naturally emerge: is it viable to integrate a microscopy technique into a time-resolved spectroscopic experiment to detect ultrafast light-matter interaction in two and more dimensions with simultaneously high temporal and spatial resolution? Such a measurement would take advantage of both methods, providing profound insight into dynamical processes behind the light excitation of complex microscopic objects. In practice, this concept is extremely difficult to implement using the above-mentioned standard techniques. The main difficulty appears with the application of ultrashort broadband pulses to conventional imaging systems, resulting in a high degree of chromatic aberration. However, one exclusively optical metrology approach is capable of achieving this ambitious goal but, so far, it has been limited to the terahertz band.

Time-domain electro-optic sampling methodology [14] based on the second-order nonlinear process was first introduced in the terahertz region in 1982 [15] and later applied to mid-infrared pulses [16]. Only recently, the technique has shown promising routes to be extended towards shorter wavelengths: electro-optic sampling capable of resolving the field evolution of near-infrared and visible waveforms has been demonstrated, with the current limit in temporal resolution of about 1 fs [17, 18]. Due to its compactness and exceptional sensitivity, electro-optic sampling has become an exemplary and routine metrology technique for ultrafast time-domain field measurements. Interestingly, it has been also applied to reveal molecular composition of biological samples yielding vast information compared to traditional frequency-resolved spectroscopy [19].

To achieve the promising performance of field-resolved microscopy, terahertz electro-optic sampling was combined with scattering-type scanning optical microscope [20, 21]. In that case, spatial resolution below the diffraction limit was attained but required long raster scans with a metallic tip to extract two-dimensional information, which is not applicable to dynamic samples.

Alternatively, electro-optic sampling has been directly extended to an imaging configuration, providing not a single spatially-averaged temporal waveform but many time-resolved pixels over a wide area captured at the same time. Accordingly, electro-optic imaging systems can record the two-dimensional field-resolved interaction of different plasmonic or biological samples with light. This configuration, being a unique combination of spectroscopic and microscopic techniques, gives comprehensive spatio-temporal information about a sample under study. It is particularly important that this information is obtained with sub-cycle temporal and subwavelength spatial precision without raster scanning. As men-

tioned earlier, this imaging approach has been only limited to the terahertz spectral region. The current thesis aims to bring valuable properties of such imaging apparatus to telecom and optical bands, where the majority of modern laser sources operate.

This dissertation is organized as follows:

Chapter 1 provides a theoretical treatment of ultrashort pulses and their propagation in both linear and nonlinear regimes, necessary for the experimental part of the thesis. Furthermore, the description includes the case when the electric field of a pulse contains various spatio-temporal couplings. General metrology techniques are discussed both in the temporal and spatio-temporal domains. A special attention is devoted to electro-optic sampling as a central method of the thesis, with an extension to the space domain, yielding an innovative phase-resolved hyperspectral imaging in the near-infrared and visible. The last section introduces the operational principles of revolutionized metasurface optical elements used in Chapter 4.

Chapter 2 describes the utilized laser system, which is based on an optical chirped pulse amplification scheme, delivering phase-stable near-infrared waveforms. Moreover, the process of light synthesis is mentioned, as well, providing experimental conditions for the application of electro-optic imaging in the visible range. The extraction of the electric field as a series of snapshots is discussed with the limits of temporal and spatial resolution.

Chapter 3 introduces the first experimental evidence of field-resolved imaging, operating in the near-infrared and visible. The imaging technique is applied to measure spatio-temporal structure of two-cycle pulses, coming directly from the optical parametric amplifier. Spatio-temporal characterization of ultrabroadband sub-cycle synthesized waveforms is presented, as well. The complete information about the electric field is utilized to provide a straightforward route to observe various spatio-temporal pulse distortions. The chapter is finished with a discussion of various potential applications and further advancements of the introduced method of spatiotemporal metrology.

Chapter 4 contains experimental studies of metasurface optics that locally control behavior of the transmitted light. In the present work, meta-samples are employed to generate complex electric fields in the far-field. The emerged field patterns are recorded in the focus of the metasurface elements using electro-optic imaging. Temporal and spatial characteristics of such electric fields are demonstrated, with a comparison to a conventional refractive optic. The chapter is finished with a discussion of various potential applications and further advancements in assistance of the design of metasurface optics.

Chapter 5 transfers basic experimental principles of near-field terahertz real-time microscopy to the new spectral ranges. Accordingly, we present detection of near-field features created by a collection of silver microparticles in the near-infrared range. The measurement is implemented with sub-wavelength spatial and sub-cycle temporal resolution. The chapter is finished with a discussion of various potential applications and further advancements of real-time near-field electro-optic imaging.

Finally, Chapter 6 summarizes the results presented in the thesis. A short discussion about further applications and development prospects of the electro-optic imaging system concludes this dissertation.

Chapter 1

Theoretical Background

The aim of the current chapter is to briefly introduce the necessary theoretical background of the physical processes described in the present thesis. The work deals with ultrashort laser pulses on a few femtosecond time scale, spanning from the ultraviolet to near-infrared spectral regions.

Section 1.1 begins the theoretical overview with the fundamental pulse characteristics and light propagation in a dispersive medium in the linear regime. The description of the nonlinear optics, where the material response is no longer linearly proportional to the applied electric field, is mainly focused on second-order nonlinear effects. The principles of optical parametric amplification based on difference frequency generation, enabling the generation of powerful near-infrared wave packets in Chapter 2, are presented with an analytical interpretation. The case when the electric field of a pulse cannot be decomposed into purely temporal and spatial parts is addressed, as well, with a visualization of the focusing dynamics of a pulse carrying various spatio-temporal distortions. Section 1.2 introduces essential few-cycle pulse characterization schemes that allows the time-dependent component of rapidly-oscillating fields to be extracted, and modern spatiotemporal interferometric metrology techniques. Section 1.3 emphasizes and describes operational principles of one individual pulse retrieval technique, on which the entire thesis relies, in both time-domain and imaging configurations. Finally, Section 1.4 introduces the basic concepts of light propagation with phase discontinuities, which are important for understanding light shaping using metasurface optical elements in Chapter 4.

1.1 Physics of Ultrashort Pulses

The mathematical description is based on the electric field component of the electromagnetic wave, and the magnetic part is not treated explicitly. If needed, the magnetic field can be obtained from the known electric field via Maxwell's equations. For the calculations, the MKS system of units (SI) is employed. For a more detailed treatment of ultrashort pulses and their propagation phenomena, the reader may consider reading textbooks such as [22–25].

1.1.1   Fundamentals and Propagation of Ultrashort Pulses

For the beginning, the temporal function of the oscillating electric field E is assumed to be not coupled to spatial coordinates and polarization state. The basic conversion from a real electric field $E(t)$ to the complex spectrum $\tilde{E}(\omega)$ and then to complex electric field $\tilde{E}^+(t)$ can be done using the complex Fourier transform [22].

$$\tilde{E}(\omega) = \int_{-\infty}^{+\infty} E(t)e^{-i\omega t}dt, \tag{1.1}$$

$$\tilde{E}^+(t) = \frac{1}{2\pi} \int_0^{+\infty} \tilde{E}(\omega)e^{i\omega t}d\omega, \tag{1.2}$$

where $\tilde{E}^+(t)$ corresponds to the positive frequencies. It can be connected to the real electric field $E(t)$ and its complex Fourier transform $\tilde{E}(\omega)$ by the relations

$$E(t) = \tilde{E}^+(t) + \tilde{E}^-(t), \tag{1.3}$$

$$\tilde{E}(\omega) = \tilde{E}^+(\omega) + \tilde{E}^-(\omega), \tag{1.4}$$

where $\tilde{E}^-(t)$ and $\tilde{E}^-(\omega)$ correspond to the negative frequencies. The complex electric field as an analytic signal can be also calculated from the real quantity and its Hilbert transform

$$\tilde{E}^+(t) = E(t) + i\mathscr{H}\{E(t)\}. \tag{1.5}$$

This allows us to express the complex electric field $\tilde{E}^+(t)$ via the instantaneous amplitude $A(t)$ and phase terms $\Gamma(t)$:

$$\tilde{E}^+(t) = A(t)e^{i\Gamma(t)} = A(t)e^{i(\phi_0+\phi(t)+\omega_0 t)}, \tag{1.6}$$

where ω_0 is the carrier frequency of the laser pulse, which determines the rapidly varying component of the field. The main interest is focused on the phase and its constituents: the first constant phase term ϕ_0 is usually referred to as the carrier envelope phase (CEP). This quantity is of great importance in ultrafast physics and particularly the current thesis, as few-cycle pulses can no longer be described by the slowly varying envelope approximation. As an example, two pulses with 3 fs time duration and the same envelope are illustrated in Fig. 1.1a. The shape of the electric field has a strong dependence on the CEP, resulting in a higher peak amplitude for $\phi_0 = 0$. In contrast, if a pulse is relatively long (Fig. 1.1b), the CEP dependence can be neglected. The second phase term $\phi(t)$ is a time-dependent quantity, which defines the instantaneous frequency $\omega_{inst}(t)$ [26]:

$$\omega_{inst}(t) = \omega_o + \frac{d\phi(t)}{dt}. \tag{1.7}$$

The electric field can be also treated in the frequency domain $\tilde{E}(\omega)$. This representation is more intuitive to better understand the underlying pulse effects. As the positive- $E^+(\omega)$
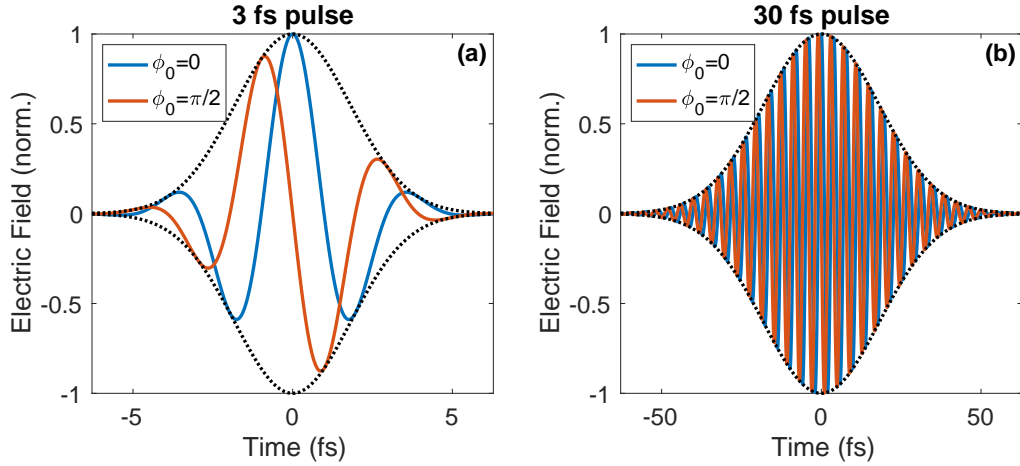
Figure 1.1: Carrier envelope phase ϕ_0 of a few-cycle pulse: **(a)** Shape of the electric field of a 3 fs pulse changes strongly with CEP, resulting in different peak amplitudes; **(b)** Shape of the electric field of a 30 fs pulse shows neglectable CEP dependence.

and negative-frequency components $E^-(\omega)$ contain the same information, the latter will be omitted. The spectral electric field can be expressed as

$$E^+(\omega) = \sqrt{S(\omega)}e^{i\psi(\omega)}, \tag{1.8}$$

where $S(\omega)$ is the spectrum and $\psi(\omega)$ is the spectral phase. It is common to expand the spectral phase in a Taylor series around ω_0 [27]:

$$\psi(\omega) = \psi(\omega_0) + \left.\frac{d\psi}{d\omega}\right|_{\omega_0}(\omega - \omega_0) + \frac{1}{2}\left.\frac{d^2\psi}{d\omega^2}\right|_{\omega_0}(\omega - \omega_0)^2 + \ldots \tag{1.9}$$

The first three terms in the Taylor expansion are the most relevant: the zeroth-order component simply corresponds to the CEP. The first-order term is often referred to as group delay (GD), which is just a shift in time of the envelope. The second-order part is the group-delay dispersion (GDD), which causes the formation of a temporal linear chirp when ω_{inst} increases linearly with time. In addition to the GDD, higher-order terms can also lead to pulse stretching, affecting the pulse shape by introducing nonlinear chirp, which induces the generation of satellite pulses and wings.

The propagation of laser pulses will be considered in a nonmagnetic, source-free ($\rho = 0$ and $\mathbf{J} = 0$) material, described by Maxwell's equations [23]

$$\nabla \cdot \mathbf{D} = 0, \qquad \nabla \cdot \mathbf{B} = 0, \tag{1.10}$$

$$\nabla \times \mathbf{E} = -\frac{\partial \mathbf{B}}{\partial t}, \tag{1.11}$$

$$\nabla \times \mathbf{H} = \frac{\partial \mathbf{D}}{\partial t}, \tag{1.12}$$

with the following matter equations:

$$\mathbf{D} = \epsilon_0 \mathbf{E} + \mathbf{P}, \qquad \mathbf{B} = \mu_0 \mathbf{H}, \tag{1.13}$$

where bold quantities are vectors, ϵ_0 and μ_0 are the permittivity and permeability of free space, respectively, and $\epsilon_0 \mu_0 = 1/c^2$. The nonlinear wave equation for $\mathbf{E}$ can be easily derived from Maxwell's equations, which in Cartesian coordinates looks like [22]:

$$\left(\frac{\partial^2}{\partial x^2} + \frac{\partial^2}{\partial y^2} + \frac{\partial^2}{\partial z^2} - \frac{1}{c^2} \frac{\partial^2}{\partial t^2} \right) \mathbf{E}(x, y, z, t) = \frac{1}{\epsilon_0 c^2} \frac{\partial^2}{\partial t^2} \mathbf{P}(x, y, z, t). \tag{1.14}$$

The right-hand part contains the polarization component $\mathbf{P}$, which characterizes the material response and its impact on the electric field. It is common to divide the polarization into two terms, depending on the strength of the applied electric field and resulting optical effects

$$\mathbf{P} = \mathbf{P}_L + \mathbf{P}_{NL}. \tag{1.15}$$

The nonlinear polarization and related optical phenomena will be discussed in the next subsection. The linear term $\mathbf{P}_L$, which induces refraction, dispersion, diffraction, etc., is coupled to the electric field by the relation:

$$\mathbf{P}_L = \epsilon_0 \chi^{(1)}(\omega) \mathbf{E}, \tag{1.16}$$

where $\chi^{(1)}(\omega)$ is the linear term of the dielectric susceptibility $\chi(\omega)$. In this subsection, the case when the electric field can be decomposed into spatial and temporal components as $\mathbf{E}(x, y, z, t) = u(x, y, z)\mathbf{E}(z, t)$ is considered, i.e. spatio-temporal couplings are absent. The linearly polarized electric field is assumed to be a plane wave, i.e. no spatial component. Applying the Fourier transform to Eqn. 1.14 yields

$$\left(\frac{\partial^2}{\partial z^2} + \frac{n^2(\omega)}{c^2} \omega^2 \right) E(z, \omega) = 0, \tag{1.17}$$

where $n^2(\omega) = 1 + \chi^{(1)}(\omega)$. The refractive index $\tilde{n}(\omega)$ is generally a complex quantity, i.e. $\tilde{n}(\omega) = n(\omega) + i\kappa(\omega)$, where the real and imaginary parts are connected through the Kramers-Kronig relation. If the pulse envelope does not change substantially over a distance $\sim \lambda_0 = 2\pi/\omega_0$, the solution to Eqn. 1.14 for the case of a plane wave will be

$$E(z, t) = E_0(z, t) e^{i(\omega_0 t - k_0 z)}, \tag{1.18}$$

where the wave vector k_0 is determined as

$$k_0^2 = \omega_0^2 n^2(\omega_0)/c^2. \tag{1.19}$$

Now, we will consider the propagation of a beam with spatial dependence, $u(x, y, z)$. The fast variations of the electric field $E(x, y, z, t)$ along the z-direction are included in the exponential part of Eqn. 1.18. Thus, the z-dependence of $u(x, y, z)$ is supposed to
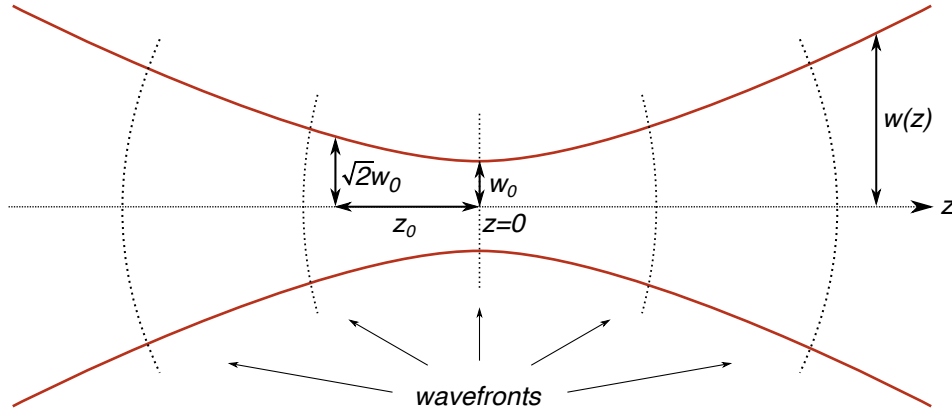
Figure 1.2: Propagation of Gaussian beam along the z axis focused at $z = 0$. The wavefronts around the focus are emphasized with dotted lines.

be slowly varying with z. The wave equation Eqn. 1.14 for the spatial component in the paraxial approximation would be

$$\left(\frac{\partial^2}{\partial x^2} + \frac{\partial^2}{\partial y^2} - 2ik_0 \frac{\partial}{\partial z} \right) u(x, y, z) = 0. \tag{1.20}$$

One of the fundamental solutions to Eqn. 1.20 is a Gaussian profile, which serves as an optimal model for the propagation description of most of the modern laser pulses [23, 28]

$$u(x, y, z) = u_0 \frac{w_0}{w(z)} e^{i\Theta(z)} e^{-(x^2+y^2)/w^2(z)} e^{ik_0(x^2+y^2)/2R(z)}, \tag{1.21}$$

where u_0 is the amplitude, $w(z) = w_0(1 + z^2/z_0^2)^{1/2}$ is the beam radius at distance z from the waist w_0, $z_0 = \pi w_0^2/\lambda$ is the Rayleigh range: the distance from w_0, where the area of the cross-section is doubled; $R(z) = z + z_0^2/z$ is the radius of the wavefront curvature and $\Theta(z) = \arctan(z/z_0)$ is the Guoy phase, which causes a phase shift of π while propagating through the focus. The propagation and the main parameters of the Gaussian beam are depicted in Fig. 1.2.

For the experimental part of the thesis, it is also useful to mention the propagation of Bessel beams, which are usually described in cylindrical coordinates (r, ϕ, z) by [29, 30]:

$$u(r, \phi, z) = u_0 J_n(k_r r) e^{\pm in\phi}, \tag{1.22}$$

where $k_r = (k_0^2 - k_z^2)^{1/2}$ is the radial wave vector, $J_n(a)$ is the nth-order Bessel function of the first kind, which can be expressed through the series expansion around $a = 0$

$$J_n(a) = \sum_{m=0}^{\infty} \frac{(-1)^m}{m!\Gamma(m+n+1)} \left(\frac{a}{2} \right)^{2m+n}, \tag{1.23}$$

where $\Gamma(b)$ is the gamma function. Eqn. 1.22 shows that the transverse distribution of Bessel beams is independent of the z coordinate, which implies that such beams possess non-diffracting features. The exponential factor in Eqn. 1.22 means that higher-ordered Bessel beams carry orbital angular momentum. Since a true Bessel beam is spatially unlimited, only a finite approximation of a zeroth-order Bessel beam J_0 known as a truncated Bessel or Bessel-Gaussian beam is studied in this work.

1.1.2   Nonlinear Optical Processes

The previous description of pulse propagation and the material response to an applied electric field has been explored in the framework of the linear regime. However, most of the key phenomena observed in the thesis correspond to the effects associated with nonlinear material response. When the incident electric field is comparable with the inner local fields of the material such as atomic and crystal fields, it can no longer be treated as negligibly small. The temporal component of the induced nonlinear polarization $\mathbf{P}_{NL}$ can be presented as [25]

$$P_{NL}(t) = \epsilon_0 \chi^{(2)} E^2(t) + \epsilon_0 \chi^{(3)} E^3(t) + \cdots + \epsilon_0 \chi^{(n)} E^n(t) + \ldots \qquad (1.24)$$

Our focus will be second-order nonlinear effects, which are observed in non-centrosymmetric materials with non-zero second-order susceptibility ($\chi^{(2)} \neq 0$). If an electric field with a temporal component $E(t)$ in the form

$$E(t) = E_0 e^{-i\omega_0 t} + \text{c.c.} \qquad (1.25)$$

is incident on a crystal with $\chi^{(2)}$ susceptibility, then the nonlinear polarization created by this field is

$$P^{(2)}(t) = 2\epsilon_0 \chi^{(2)} E_0 E_0^* + \left[\epsilon_0 \chi^{(2)} E_0^2 e^{-i2\omega_0 t} + \text{c.c.} \right]. \qquad (1.26)$$

The second-order nonlinear polarization comprises two parts: the first term with zero frequency and the second term with doubled frequency. The zero-frequency part leads to the case when the light induces a static electric field (DC component). This effect, called optical rectification, is usually quite weak, but under some conditions, it can generate intense terahertz radiation [31, 32]. The second part of Eqn. 1.26 can yield the generation of light at the second harmonic of the fundamental frequency, called second-harmonic generation (SHG) or frequency doubling. This nonlinear process can also be explained with the help of an energy level diagram, where two photons with the same energy result in the emission of a single photon with doubled energy (Fig. 1.3).

Let us consider the case when a light field, consisting of two distinct frequency components, is incident on a $\chi^{(2)}$ crystal:

$$E(t) = E_1 e^{-i\omega_1 t} + E_2 e^{-i\omega_2 t} + \text{c.c.}. \qquad (1.27)$$

The resulting nonlinear polarization of the material is

$$P^{(2)}(t) = 2\epsilon_0 \chi^{(2)} \left[E_1 E_1^* + E_2 E_2^* \right] + \epsilon_0 \chi^{(2)} \left[E_1^2 e^{-i2\omega_1 t} + E_2^2 e^{-i2\omega_2 t} \right]$$
$$+ \epsilon_0 \chi^{(2)} \left[2E_1 E_2 e^{-i(\omega_1+\omega_2)t} + 2E_1 E_2^* e^{-i(\omega_1-\omega_2)t} + \text{c.c.} \right]. \qquad (1.28)$$
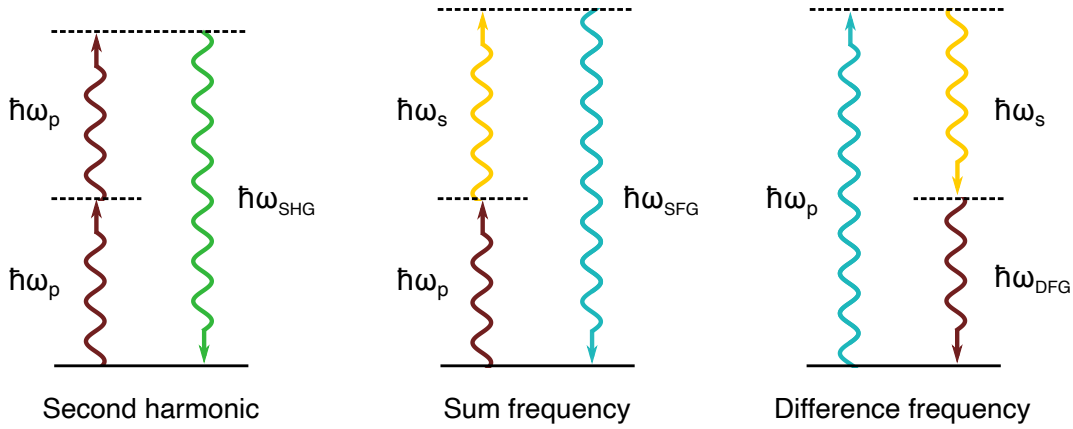
Figure 1.3: Second-order nonlinear processes described by energy level diagrams: second harmonic generation ω_{SHG}, sum frequency generation ω_{SFG} and difference frequency generation ω_{DFG}.

The first two terms of Eqn. 1.28 are likewise related to the optical rectification and SHG of both incident frequencies. In addition, the polarization leads to the generation of sum frequency (SFG) and difference frequency (DFG) of ω_1 and ω_2, as can be seen in the third term. The energy level diagram of these nonlinear processes is depicted in Fig, 1.3, as well. Both nonlinear phenomena are of great importance for this thesis and will be discussed in detail in the next sections. The DFG process is a fundamental principle of optical parametric amplification (Subsection 1.1.3) while SFG enables the realization of the pulse retrieval technique called electro-optic sampling (Section 1.3).

If we consider the position dependence of the interacting beams with wave vectors $\mathbf{k}_i$, $\mathbf{k}_j$, and $\mathbf{k}_k$, then momentum conservation must be also fulfilled:

$$\mathbf{k}_k = \mathbf{k}_i + \mathbf{k}_j \tag{1.29}$$

This condition, called phase-matching, determines the efficiency of a nonlinear process. It is generally difficult to achieve even for the collinear geometry, as the refractive index of most materials increases with a frequency (normal dispersion). The standard way to reach the phase-matching condition is the application of birefringent crystals. This approach relies on the dependence of the refraction index on the incident polarization direction of light. Interestingly, crystals with a cubic crystal system do not possess inversion symmetry but are non-birefringent, i.e. optically isotropic. A negative uniaxial crystal ($n_o > n_e$) provides two commonly used phase-matching angles: type-I (eoo) and type-II (eoe), where the order is $\omega_3 \geq \omega_2 \geq \omega_1$, and o and e are the ordinary and extraordinary axes of the crystal, respectively [25].

An alternative to the use of birefringent materials is quasi-phase-matching [33]. The most commonly used technique to achieve quasi-phase-matching is periodic poling, in which material's nonlinear susceptibility changes sign after every coherence length $L_{coh} = \pi/\Delta k$. Such materials can be directly grown or made of a ferromagnetic structure, where a static

electric field is applied to invert the orientation of the ferroelectric domains [34]. In the current work, a periodically poled lithium niobate crystal is utilized for the amplification scheme (see Chapter 2).

Third-order nonlinear processes include many important and interesting optical effects, as well, but in the present thesis, they will not be emphasized. However, a few basic facts are worth noting. The third-order susceptibility $\chi^{(3)}$ gives rise to optical phenomena such as four-wave mixing, third-harmonic generation, two-photon absorption, etc. In addition, the real part of $\chi^{(3)}$ also contributes to the refractive index by appending an intensity-dependent nonlinear term: $n = n_0 + n_2 I$, where n_0 is the linear refractive index and $n_2 = 3\chi^{(3)}/4n_0^2\epsilon_0 c$. This induces self-focusing when a localized beam, traveling through a medium with $n_2 > 0$, experiences a positive lensing effect (Kerr lens), enabling the realization of Kerr-lens mode-locked laser oscillators. Such oscillator is employed as the initial light source of the laser system of the present thesis. Similarly, a localized pulse in time is affected in a way that new frequencies are generated due to the intensity-dependent shift of the instantaneous phase. This phenomenon is called self-phase modulation, which is additionally accompanied by the self-steeping effect [35] and utilized in the thesis to create broadband fields.

One of the most intriguing optical phenomena occurring in a medium with the $\chi^{(3)}$ nonlinear susceptibility is associated with stable pulse propagation without changing the spatiotemporal shape. It takes place when linear impact of diffraction and dispersion is compensated by the nonlinear effects of self-focusing and self-phase modulation, respectively. As a result, spatiotemporally localized pulses can be formed that travel for long distances. These light wave packets are often referred to as spatio-temporal solitons or light bullets [36] and have been also studied in $\chi^{(2)}$ media [37]. Potential applications of light bullets cover many relevant scientific spheres including all-optical data processing [38] or highly precise interferometry [39]. Despite the fascinating features, these spatio-temporal objects are outside of the scope of the current work.

1.1.3   Optical Parametric Amplification

Laser sources like those based on Ti:Sapphire produce coherent light radiation in the near-infrared/visible spectral range with a central wavelength around 800 nm. To conduct experiments in different spectral regions, the nonlinear optical processes described in the previous subsection can be used. In particular, to create near-infrared to mid-infrared wave packets, DFG down-conversion can be implemented. However, the power of the generated light is generally not sufficient to perform strong-field measurements. Therefore, schemes based on optical parametric amplification (OPA) have been developed and are constantly being improved to provide powerful irradiation, beyond the spectral regime of traditional oscillators [40, 41].

To investigate the OPA process, we consider in detail the DFG term of the nonlinear polarization $P^{(2)}$ in Eqn. 1.28:

$$P_3^{(2)}(z,t) = 4\epsilon_0 d_{eff} E_1 E_2^* e^{-i\omega_3 t} = 4\epsilon_0 d_{eff} A_1 A_2^* e^{i[(k_1 - k_2)z - \omega_3 t]} + \text{c.c.} \qquad (1.30)$$
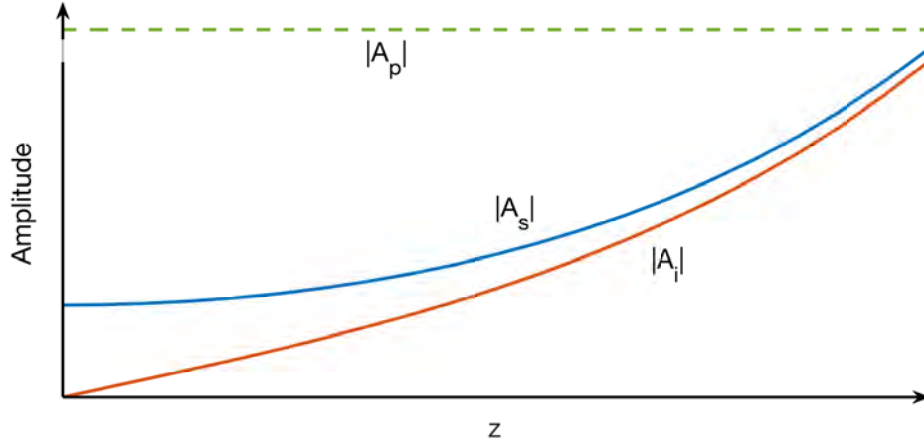
Figure 1.4: Evolution of signal A_s and idler A_i beams during the optical parametric amplification under conditions of perfect phase matching and undepleted-pump approximation.

where $\omega_3 = \omega_1 - \omega_2$ is the generated difference frequency component, $d_{eff} = \chi^{(2)}/2$ is the effective nonlinear coefficient and $E_i = A_i \exp(ik_i z)$, $i = 1, 2, 3$. Substitution of Eqn. 1.30 into the wave equation Eqn. 1.14 yields

$$\frac{d^2 A_3}{dz^2} + 2ik_3 \frac{dA_3}{dz} = \frac{-4d_{eff}\omega_3^2}{c^2} A_1 A_2^* e^{i(k_1 - k_2 - k_3)z}. \tag{1.31}$$

Applying the slowly varying amplitude approximation and repeating the procedure for A_1 and A_2, a set of coupled-wave equations for A_1, A_2 and A_3 can be obtained:

$$\frac{dA_1}{dz} = \frac{2id_{eff}\omega_1^2}{k_1^2 c^2} A_3 A_2^* e^{i\Delta kz}, \tag{1.32}$$

$$\frac{dA_2}{dz} = \frac{2id_{eff}\omega_2^2}{k_3^2 c^2} A_3 A_1^* e^{i\Delta kz}, \tag{1.33}$$

$$\frac{dA_3}{dz} = \frac{2id_{eff}\omega_3^2}{k_3^2 c^2} A_1 A_2^* e^{-i\Delta kz}, \tag{1.34}$$

where $\Delta k = k_3 - k_1 - k_2$ is the phase mismatch. For parametric amplification, it is common to use designations in terms of signal ($\omega_s \equiv \omega_1$), idler ($\omega_i \equiv \omega_2$) and pump ($\omega_p \equiv \omega_3$). Under conditions of perfect phase-matching ($\Delta k = 0$) and the pump wave being strong and constant in the process of amplification ($dA_p/dz = 0$), solutions for $A_s(z)$ and $A_i(z)$ can be derived in the following form [25]

$$A_s(z) = A_{s0} \cosh(\kappa z), \tag{1.35}$$

$$A_i(z) = i \left(\frac{n_s \omega_s}{n_i \omega_i} \right)^{1/2} \sinh(\kappa z), \tag{1.36}$$

where the boundary conditions $A_s(z=0) = A_{s0}$, $A_i(z=0) = 0$ were used, and

$$\kappa = \frac{4d_{eff}^2\omega_s^2\omega_i^2|A_p|^2}{k_s k_i c^4}. \tag{1.37}$$

According to Eqn. 1.35 and 1.36, both signal and idler waves experience an exponential growth with crystal distance if the gain is large $\kappa z \gg 1$ (Fig. 1.4). This is a distinctive feature of the optical amplifier. Additionally, the input phase of the signal wave is preserved in the process of amplification, while the resulting phase of the idler wave depends on both pump and signal wave packets.

To produce high-intensity ultrashort laser pulses, concepts based on a combination of OPA with chirped pulse amplification (CPA) have been established [42]. CPA is a technique for amplifying ultrashort pulses to a relatively high level, where an input pulse is first stretched in time by introducing a temporal chirp using, for example, a pair of gratings or prisms, then amplified and recompressed. This allows for a reduction of the pulse peak intensity in the gain medium, preventing potential material damages caused by self-focusing effects. Optical parametric chirped pulse amplification (OPCPA) incorporates the advantages of both techniques [43–45]. In the current thesis, OPCPA is employed to provide high power for few-cycle laser pulses centered at 1.9 µm wavelength (Chapter 2).

1.1.4   Spatio-Temporal Couplings of Pulses

So far, the propagation of laser pulses has been considered under the assumption that the electric field $E(x,y,z,t)$ can be uncoupled into the spatial and temporal components as $E(x,y,z,t) = u(x,y,z)E(z,t)$. This is not always the case, especially in the ultrashort regime when a pulse contains a large bandwidth. In practice, the spatio-temporal manipulation is routine, as many laboratories utilize optical devices such as prisms and gratings for pulse compression. However, even simple optical elements like transmitting windows, lenses, apertures, etc. or nonlinear optical processes can result in the creation of subtle connections between the spatial $u(x,y,z)$ and temporal components $E(z,t)$, so called spatio-temporal couplings (STCs), which modify and distort the pulse.

Three examples of the formation of STCs are illustrated in Fig. 1.5. One of the optical elements to operate with laser pulses is a flat window, which in case of a slight tilt produces a spatial color separation by refracting various frequency components differently due to the wavelength-dependent refractive index (Fig. 1.5a). If this spatially chirped pulse travels in a dispersive medium, which is usually the case unless vacuum equipment is applied, then the higher-frequency components retard with respect to the lower frequencies in the material with normal dispersion (Fig. 1.5c). In this case, the output pulse will gain another STC called pulse-front tilt. In Fig. 1.5b, an input pulse without STCs after passing through a prism possesses not only pulse-front tilt but also angular dispersion and spatial chirp.

Here, first-order spatio-temporal distortions are analytically studied, closely following the work introduced in [47, 48] as one of the best theoretical and numerical description of various spatio-temporal distortions. For more detailed analysis, the reader may consider
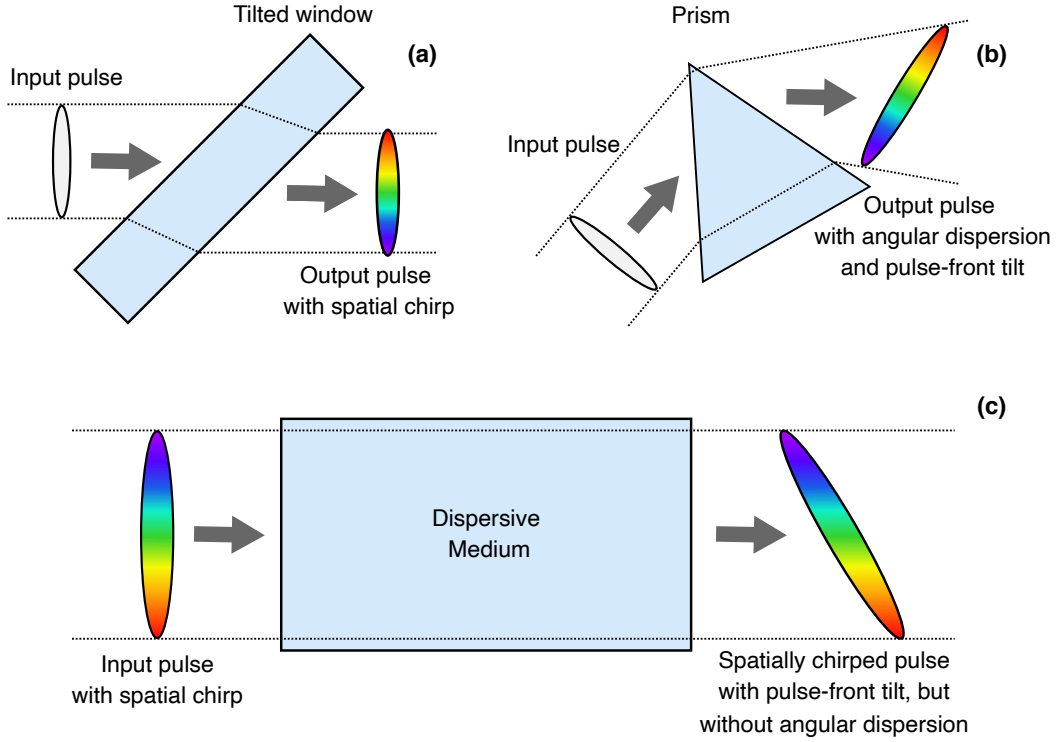
Figure 1.5: Formation of spatio-temporal couplings after passing through different optics. **(a)** Undistorted input pulse gains spatial chirp at the output of a tilted window. **(b)** A prism affects the input pulses causing angular dispersion and pulse-front tilt of the output pulse. **(c)** Spatially chirped input pulse propagating through a dispersive medium experiences pulse-front tilt. The picture is redesigned from [46].

reading the paper [49]. For the theoretical description of STCs, the electric field $E(x, y, z, t)$ of linearly polarized light is assumed to have the form as $E(x, t)$, neglecting the coordinates y and z. Then, a coupling-free electric field takes the form $E(x, t) = E(x)E(t)$. To introduce first-order coupling to the light pulse, the electric field can be re-written as

$$E(x, t) \rightarrow E(x, t + \zeta x), \tag{1.38}$$

where ζ is the parameter determining the coupling. Neglecting the higher-order terms of the temporal phase after the second order (linear chirp) and assuming a Gaussian approximation over space and time, the electric field can be presented as [47]

$$E(x, t) \propto \exp(Q_{xx}x^2 + 2Q_{xt}xt - Q_{tt}t^2), \tag{1.39}$$

where the complex coefficients Q_{xx} and Q_{tt} are associated with various spatial and temporal parameters, respectively:

$$Q_{xx} = -i\frac{\pi}{\lambda R(z)} - \frac{1}{w^2(z)} \qquad Q_{tt} = -i\beta + \frac{1}{\tau^2}. \tag{1.40}$$

The physical meaning of $R(z)$ and $w(z)$ in the spatial product Q_{xx} are the radius of curvature and the beam size along the z-axis, respectively. The temporal part consists of parameters β, which is responsible for the temporal chirp of the pulse, and τ, determining the pulse duration. The complex cross term Q_{xt} in Eqn. 1.39 corresponds to two spatio-temporal distortions. The real part of Q_{xt}, which contains the energy distribution, causes the position dependence of the intensity on the arrival time, i.e. the pulse-front tilt. The imaginary part leads to a distortion of the phase fronts, which in this case results in a rotation of the pulse wavefront in time — wavefront rotation.

The electric field in the space-time dimension $E(x,t)$ can be transferred to other domains using the Fourier transform, e.g. $E(x,\omega)$, $E(k,t)$ or $E(k,\omega)$, to study other forms of STCs. For the space-frequency domain, the electric field takes the form:

$$E(x,\omega) \propto \exp(R_{xx}x^2 + 2R_{x\omega}x\omega - R_{\omega\omega}\omega^2). \tag{1.41}$$

Similar to the previous example in the spatio-temporal domain, the cross-term $R_{x\omega}$ in Eqn. 1.41 yields the couplings in the spatio-spectral domain. The real part of $R_{x\omega}$ causes the spatial separation of different frequencies, referred to as spatial chirp. The physical meaning of the imaginary part of $R_{x\omega}$ is that various frequencies feature different tilts of the phase front - wave-front tilt dispersion. In the spatial frequency-time domain $(k - t)$, the electric field has the following form

$$E(k,t) \propto \exp(P_{kk}k^2 + 2P_{kt}kt - P_{tt}t^2), \tag{1.42}$$

In this case, the real part of the coupling term P_{kt} causes the change of propagation direction within the pulse duration. This effect is called ultrafast lighthouse. The imaginary part of P_{kt} results in the different relative phases of various propagation directions in the time scale of the pulse, i.e. the angular temporal chirp. Representation of the electric field in the $k - \omega$ domain yields

$$E(k,\omega) \propto \exp(S_{kk}k^2 + 2S_{k\omega}kt - S_{\omega\omega}\omega^2). \tag{1.43}$$

The real quantity of $S_{k\omega}$ induces the well-known optical effect called angular dispersion, which is generally utilized for pulse stretching or compression using a pair of prisms. The imaginary term leads to the effect called angular spectral chirp, where angles of propagation directions have different relative phases for the corresponding frequencies.

Since all the spatio-temporal distortions presented above are coupled among themselves, in the process of laser pulse propagation one can lead to the formation of the others. The work introduced in the paper [48] provides a possibility to observe the propagation dynamics of the first-order STCs under different practical conditions. As the visualization code used in [48] is freely distributed and available online, it is adapted here to perform numerical simulations of the propagation of pulses containing various spatio-temporal distortions. As in strong-field physics laser pulses are normally focused to achieve high intensities, we study the dynamics of 32 fs pulses in the regime when a radius of curvature of 15 mm is applied. The cases of pulse propagation in collimated and temporally-chirped regimes
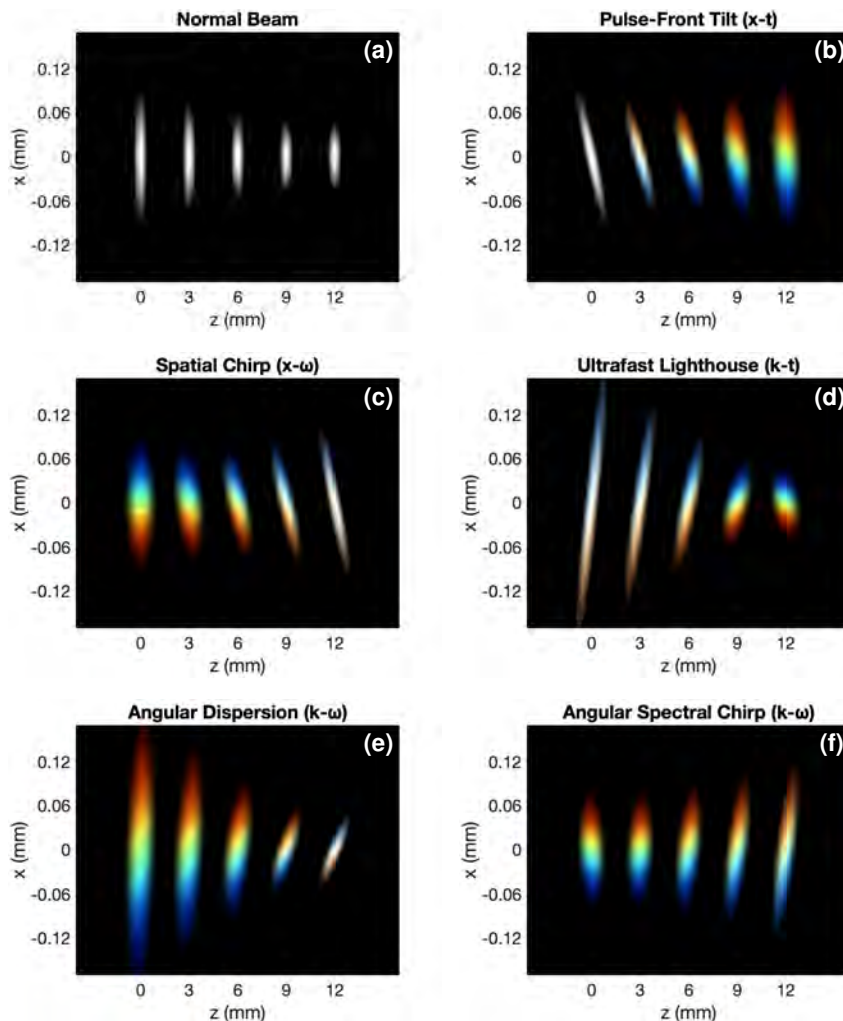
Figure 1.6: Numerical simulation of the focusing dynamics of a 32 fs pulse with different spatio-temporal distortions. **(a)** Normal beam without any spatio-temporal couplings. Input beam has a spatio-temporal distortion in the form of **(b)** pulse-front tilt, **(c)** spatial chirp, **(d)** ultrafast lighthouse, **(e)** angular dispersion, **(f)** angular spectral chirp. The visualization code is taken from [48].

as well as the detailed description and parameters of the numerical study can be found in [48]. The simulation of the focusing dynamics of the pulse with different STCs is shown in Fig. 1.6. As a reference, the beam without any distortions is depicted in Fig. 1.6a. Other images display pulse propagation with pulse-front tilt (Fig. 1.6b), spatial chirp (Fig. 1.6c), ultrafast lighthouse (Fig. 1.6d), angular dispersion (Fig. 1.6e), and angular spectral chirp (Fig. 1.6f). Although each spatio-temporal distortion has individual properties, color spreading at the focus is unavoidable, leading to longer and weaker pulses with respect to the transform- and diffraction-limited beams. Thus, methods to experimentally detect such couplings are highly requested in ultrafast and attosecond science.

1.2   Ultrafast Characterization Techniques

Laser pulses have promptly become the shortest reproducible technological events in time, which cannot be directly measured by relatively slow electronic detecting devices. Therefore, an extraordinary approach is needed to resolve femto- and attosecond field oscillations. In this section, we briefly discuss four major well-established techniques for few- and sub-cycle pulse characterization of the temporal field component $E(t)$. The ability to precisely reconstruct the electric field has enabled the study of the fundamental interaction of light with matter like the nonlinear polarization response and the dynamics of energy transfer $W(t)$ in solids, which can be expressed as [6]

$$W(t) = \int_{-\infty}^{t} E(t') \frac{d}{dt'} P_{NL}(t') dt', \tag{1.44}$$

where $E(t)$ is the incident electric field and $P_{NL}(t)$ is the nonlinear polarization. Direct access to oscillating fields can be also beneficial in other research areas [19, 50, 51].

However, in the presence of STCs, the time-dependent part of the electric field is not sufficient to fully characterize pulses. Moreover, some experiments require the spatial field component, as charges can migrate under strong-field excitation, with an option to form a complex spatio-temporal response in some cases. Since the purpose of the thesis is to present a technique for spatiotemporal field detection, a few state-of-the-art alternatives are also mentioned in this section.

1.2.1   Field Retrieval in Temporal Domain

Let us start with the most widespread method for time-domain pulse characterization - frequency-resolved optical gating (FROG) [27, 52]. The concept of the FROG technique relies on the pulse, scanned by a second time-delayed pulse, which is usually a replica of the original pulse. Their interaction is detected in the time-frequency domain through the generation of a nonlinear signal. Among many different FROG geometries, second harmonic FROG (SHG FROG) provides the best signal-to-noise ratio and the ability to measure relatively weak beams. The schematic is shown in Fig. 1.7a. A pulse under study is split into two arms, the relative arrival time of which is varied with a mechanical piezo-stage. The pulses typically interact non-collinearly in a $\chi^{(2)}$ crystal to spatially separate the generated second harmonic. The SHG signal is captured by a spectrometer yielding a spectrogram with the time dependence of the instantaneous frequency of the pulse. The FROG trace is defined as

$$I_{FROG}^{SHG}(\omega, \tau) = \left| \int_{-\infty}^{+\infty} E(t) E(t - \tau) e^{-i\omega t} dt \right|^2 \tag{1.45}$$

To retrieve the electric field $E(t)$ from Eqn. 1.45, the essentially unique solution must be found by solving the two-dimensional phase-retrieval problem [27]. Additionally, the FROG apparatus can also be modified to measure pulses with a single shot [53]. The temporal
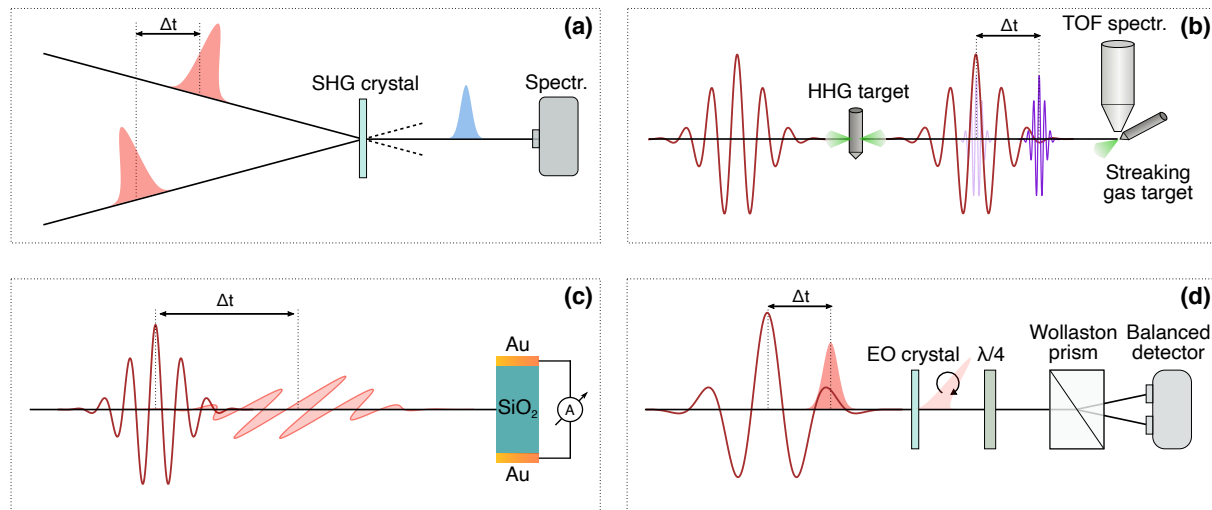
Figure 1.7: Principles of the major techniques for few-cycle pulse characterization: **(a)** second harmonic frequency-resolved optical gating; **(b)** attosecond streaking; **(c)** nonlinear photoconductive sampling; **(d)** electro-optic sampling.

resolution of FROG measurements is relatively high and depends on the beam geometry and the nonlinear process involved. The main effect that deteriorates the temporal resolution is geometrical smearing. FROG has certain phase ambiguities that, depending on the application, may be a problem. As we are interested in full reconstruction of the electric field waveform within a fixed time reference, the fact that FROG does not yield the CEP (ϕ_0) and arrival time (ϕ_1) of the pulse is a significant drawback. Although a new approach has been developed, combining FROG with another CEP-sensitive detection scheme [54], full reconstruction of the electric field with a pure FROG measurement is not feasible. In contrast, the detection methods that are discussed further are capable of extracting complete pulse information including CEP.

A fundamental metrology technique in attosecond science is streaking, which is based on the principles of the attosecond streak camera, with a requirement of a dedicated vacuum beamline [55]. The schematic of attosecond streaking is presented in Fig. 1.7b. First, the pulse under study is focused into a gas target for high harmonic generation (HHG). Although there are many variations of the HHG target including also solids (the first HHG experiment) and liquids [56, 57], the most efficient medium is considered to be a gas like neon. The emitted pulse train forms a plateau in the extreme ultraviolet (XUV) and soft X-ray region, with abrupt cut-off energy defined as $E_{max} = 3.17U_p + I_p$, where $U_p = e^2E^2/4m\omega^2$ is the ponderomotive energy and I_p is the ionization potential. The HHG process can be explained using a straightforward semi-classical concept relying on the three-step model [58]: 1) the superposition of the incident laser field and the Coulomb field modifies the binding potential of the electron allowing the electron to tunnel through the barrier at every half cycle of the laser oscillations. 2) Treated as a classical particle, the freed electron moves away from the ion accelerated by the laser field and is then driven back

when the laser field changes direction acquiring kinetic energy up to hundreds of electron volts. 3) The electron has a probability to recombine with the parent ion, releasing its kinetic energy and the binding energy as an XUV photon. A single attosecond pulse from the emerged pulse train can be isolated using techniques such as spectral filtering [9], attosecond lighthouse [59], polarization gating [60], ionization gating [61]. The resulting pulse can be exploited as a temporal gate for the detection of the fundamental laser field via streaking, with a temporal resolution determined by the duration of the gate attosecond pulse. Focusing both pulses on an atomic gas target, it is possible to measure a change in the momentum of the electrons freed by the XUV pulse and then driven by the fundamental pulse. The momentum change Δp is defined as

$$\Delta p = e \int_{t_0}^{\infty} E(t)dt = eA(t_0) \tag{1.46}$$

where $E(t)$ is the fundamental laser field and $A(t)$ is its vector potential. Varying the time delay between the two pulses and detecting the ejected photoelectrons via a time-of-flight spectrometer, full temporal evolution of the fundamental field as well as the XUV pulse information can be extracted from the streaking spectrogram using a retrieval algorithm similar to FROG [9,62]. At the moment, the shortest attosecond pulse obtained in streaking experiments is about 50 as [63]. In addition to the exceptional temporal precision of this metrology technique, the electric field is measured in absolute values. It has been also applied to resolve Bessel-like beams [64]. However, to perform streaking, the fundamental field must be sufficiently strong for the highly nonlinear process. Due to the requirement of vacuum apparatus, expensive photoelectron diagnostic tools and the extreme level of complexity of attosecond streaking, compact tabletop methods for few-cycle pulse characterization are in great demand in ultrafast and attosecond science.

An innovative metrology technique called nonlinear photoconductive sampling (NPS), which relies on the creation of a pair of charge carriers in a solid, has been recently demonstrated [13]. This detection method has a huge potential to fully replace attosecond streaking, proposing a new route to perform measurements with attosecond temporal resolution. The schematic of NPS is shown in Fig. 1.7c. In this configuration, a first few-cycle pulse called injection pulse E_i is incident on a dielectric sample, producing a strongly confined temporal gate through a high-order nonlinear process in a wide energy gap material. Particularly, the interaction of the injecting broadband light with crystalline quartz can induce the transition of electrons from the valence band to the conduction band. A second pulse called driving pulse E_d, which is much weaker than E_i ($E_d \ll E_i$) and orthogonal to the injection field polarization, displaces the injected electrons and holes in the band structure of the sample, allowing for the detection of the induced current by two electrodes attached to the sample in parallel to the driving field polarization. The measured signal S_d is

$$S_d = - \int_{-\infty}^{\infty} A_d G(t - \tau)dt, \tag{1.47}$$

which in the case of the sub-cycle injection confinement is proportional to the time-varying oscillations of the driving field $E_d(t)$, where A_d is the vector potential, τ is the delay

between the two pulses, $G(t) \propto E_i^{2n}(t-\tau_{inj})$ is the gate function with a physically unknown temporal delay of $\tau_{inj} \approx 75$ as [13]. The temporal resolution of NPS is determined by the nonlinear process of the carrier injection, providing sub-500-as temporal precision. The technique is capable of characterizing waveforms from the mid-infrared to the ultraviolet. The drawbacks of NPS include the requirement of a high-intensity injection field and a cross-polarized geometry for E_i and E_d. Nevertheless, an all-solid-state NPS modality with extremely high dynamic range and great sensitivity can become a simple, cost-effective and powerful tool to extract electric fields on the attosecond timescale.

Currently, one of the most popular metrology methods in ultrafast science is electro-optic sampling (EOS), which is the core technique of this thesis. The detection concept was first introduced in the low-frequency regime — in the terahertz spectral range [14, 15, 65]. In the present subsection, the physical principles of terahertz EOS are briefly discussed. After that, in Section 1.3, the theoretical description of EOS will be extended to the high-frequency regime, from the near-infrared to visible spectral region.

The schematic of the EOS detection is shown in Fig. 1.7d. A terahertz pulse, which can be generated through optical rectification, laser-induced plasma, etc. [66–68], is incident collinearly with a probe (sampling) pulse on an electro-optic crystal (EOS crystal) with a $\chi^{(2)}$ nonlinear susceptibility. The probe pulse is normally a weak portion of a Ti:Sapphire laser source centered at a wavelength of 800 nm. Based on the linear electro-optic effect known as the Pockels effect, the terahertz beam induces a refractive-index ellipsoid in the EOS crystal. As a result, the co-propagating linearly-polarized probe pulse experiences a polarization change. This change can be recorded using an ellipsometer consisting of a quarter-wave plate and a Wollaston prism by splitting the modified polarization of the probe beam into two orthogonal polarization states. The intensities of the resulting beams can be converted into a photocurrent using a balanced detector, which measures a difference between two photodiodes $\Delta I = I_a - I_b$. A common material for EOS detection in the far-infrared regime is a non-birefringent ZnTe crystal with cubic lattice since the refractive index of this crystal in the THz range is compatible with the one in the near-infrared. Taking into account the non-birefringent nature of ZnTe and its electro-optic tensor, we can obtain the photocurrent signal [69, 70]

$$\Delta I \propto I_p \frac{\omega^3 n E_{\text{THz}} r_{41} L}{2c} \tag{1.48}$$

where I_p is the probe intensity, ω is the probe angular frequency, n is the unperturbed refractive index, r_{41} is the electro-optic coefficient, L is the crystal length. The phase retardation induced by the THz electric field in other crystals can be found in [71]. Varying the relative time delay between the THz and probe pulses and enhancing the signal via lock-in apparatus, it is possible to reconstruct the temporal evolution of the THz waveform. The ease of use, outstanding sensitivity, and excellent dynamic range, involving only the second-order nonlinear effect have made this metrology technique the basis of time-resolved spectroscopic experiments in the THz spectral range [72–75]. Moreover, single-shot and noncollinear EOS detection schemes have been implemented [76–78]. Similar to EOS, the magnetic field can be measured using the Faraday effect in a magneto-optic medium [79].

1.2.2 Field Retrieval in Space-Time

As shown in Subsection 1.1.4, spatio-temporal distortions are very important optical effects in terms of laser pulse propagation and often cannot be ignored. In the ultrashort regime, this question should be considered with more care, as the large bandwidth of pulses in the femtosecond timescale can lead to a significant complexity of their structure in space and time if the spatio-temporal couplings are not corrected properly. Therefore, techniques that can detect STCs are essential in ultrafast and attosecond optics. Such optical approaches are often related to the spatio-temporal field reconstruction. Here, a few relevant methods for measuring the STCs and the electric field in space-time are described.

Perhaps the most straightforward technique for the detection of common STCs like pulse-front tilt and spatial chirp is GRENOUILLE [80], which is almost identical to SHG FROG, described in the previous subsection. In the standard FROG setup, a partial reflector is employed to split the beam into two identical pulses. In contrast, GRENOUILLE utilizes a Fresnel biprism to obtain two pulses through spatial splitting. In this case, an input pulse containing spatial chirp with separated frequencies in the cross-section results in the output beams carrying different frequency components. Therefore, the signal in a $\chi^{(2)}$ crystal will have a variation of wavelength over the time delay, yielding a shift in the trace proportional to the magnitude of the spatial chirp [81]. Likewise, an input beam with a pulse-front tilt is split into two constituents, consequently introducing a measurable shift of the intersection area in the crystal [82]. Although this technique does not provide the spatio-temporal electric field, it is still useful for the simple detection of one-dimensional spatio-temporal distortions.

A basic concept of metrology techniques for extracting the spatio-temporal field relies on a measurement of spatially-resolved spectral interference of a test field with a reference beam. One such interferometric approach is called Spatially Encoded Arrangement Temporal Analysis by Dispersing a Pair of Light Electric-fields (SEA TADPOLE) [83]. The pulse retrieval mechanism of SEA TADPOLE is based on the individual coupling of the test and reference pulses into short single-mode optical fibers, the output of which is collimated and crossed horizontally causing spatial fringes on a camera. Additionally, a grating is placed to map the wavelength to a spatial position. As a result, SEA TADPOLE measures a relative difference in the spectral phase between the reference and test pulses. The field $E(\omega)$ for one position (x_0, y_0) can be obtained by Fourier filtering the interferogram, similar to standard spectral interferometry. If the fiber entrance is sufficiently small compared with the test pulse dimensions, the scan of the fiber in x, y, z directions with a mechanical stage yields the spatio-spectral field $E(x, y, z, \omega)$. However, the technique requires an additional temporal measurement of the reference pulse: the pulse waveform $E_r(t)$ must be known to extract the test field $E(x, y, z, t)$ from the interferogram through the inverse Fourier transform of $E(x, y, z, \omega)$. The reader may also be interested in other detection schemes related to SEA TADPOLE [84, 85].

An alternative technique relying on combined principles of spectral interferometry and holography [86] often referred to as spatially-resolved Fourier transform spectrometry [87] has been recently presented. This approach does not require an additional reference beam
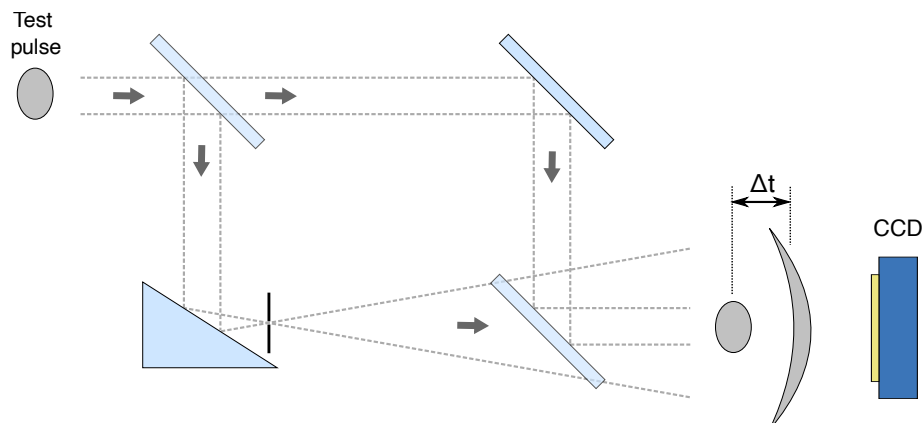
Figure 1.8: Operational principles of spatially resolved Fourier transform spectrometry.

but utilizes a spatially homogeneous portion of the original beam as a reference. In other words, this method is self-referenced, exploiting a special Mach–Zehnder interferometer as shown in Fig. 1.8. The reference arm with homogeneous structure can be generated by focusing the pulse and placing a pinhole at the focus [87] or by direct defocusing using a small convex mirror [88]. A small spatially filtered portion of the spreading beam represents a relatively unperturbed region without any potential spatio-temporal distortions that can be present in the original pulse. The interference pattern on a CCD can be recorded as a function of the time delay between the two arms. As a result, the linear cross-correlation function between the beams is measured at each pixel, allowing the application of an iterative algorithm for the extraction of the spectral phase of the test field. In analogy to the previous interferometric approach, the retrieval of the full spatio-temporal electric field requires temporal field characterization at a single point in space [87, 88].

Similarly, a recently developed interferometric scheme called INSIGHT allows for the characterization of focused pulses [89]. The conceptual model incorporates a test pulse and its time-delayed replica, enabling the measurement of spatially-resolved linear auto-correlation using a CCD. The procedure of calculating the corresponding spatio-spectral amplitude at the focus is repeated for two other positions along the propagation axis near the focus. With this set of data, an iterative algorithm can be applied to retrieve the spectral phase of the test field. However, a spatially-homogeneous spectral phase needs still to be measured using, for example, FROG to reconstruct the test field in space-time.

It has to be noted that none of the above-mentioned and other techniques like [90–93] for spatio-spectral/temporal field reconstruction have become popular in the community, as the level of complexity is still high, with a need for the application of phase retrieval algorithms. Besides, these methods primarily yield a spatio-spectral field, which is typically difficult to treat and analyze, with a requirement of an extra measurement to convert it into the spatio-temporal dimension. Accordingly, to determine the CEP of the test field, a CEP sensitive measurement must be performed to the reference pulse, making the exploitation of interferometric approaches even less attractive. For this reason, a simple and direct method for spatio-temporal metrology is in great demand at the moment.

1.3   High-Frequency Electro-Optic Sampling

This section proceeds with the introduction of the EOS operational principles in the high-frequency (broadband) regime, as the present thesis deals with laser pulses in the near-infrared (NIR) and visible. Since EOS is a purely optical methodology, spatially-resolved reconstruction of the test electric field can be implemented by integrating a standard imaging unit. The description of EOS imaging configuration establishes a theoretical platform for the experimental part of the thesis (Chapters 3-5).

1.3.1   Near-Infrared and Visible Regimes

The first experimental evidence of time-domain EOS operating in the near-infrared regime has been demonstrated in 2016 by our research group [17]. Already one year later, our team has shown a capability of the EOS technique to temporally resolve wavelengths as short as 670 nm in measurements involving lightwave synthesis, extending EOS to the visible spectral region [94]. Here, an alternative description of EOS is introduced, functioning under conditions when the rapidly oscillating field under study cannot be considered as quasi-static and the Pockels effect is not applicable.

The detection of short-wavelength fields like the near-infrared or visible relies on the use of broadband probe pulses. The interaction of the test field and the probe pulse in a $\chi^{(2)}$ nonlinear medium can be treated from the point of view of a three-wave mixing process: sum or difference frequency generation. Our analysis will be constrained to the generation of sum frequency, as the difference frequency might spectrally overlap with the test field. Moreover, silicon detectors are more suitable for SFG wavelengths. The SFG pulse emerging with an orthogonal polarization to the incident probe pulse can be interpreted as a spectrally up-shifted replica of that probe (Fig. 1.9). A certain spectral window of the original probe pulse will have spectral overlap with the newly generated SFG radiation if the probe bandwidth is sufficiently broadband. The overlapped part of the sampling spectrum is referred to as the local oscillator (LO), which contains the shortest wavelengths of the pre-existing probe pulse. Careful isolation of that spectral window using a band-pass filter leads to an ability to overcome the requirement of the probe pulse to be significantly shorter than a half cycle of the field oscillation. This enables the spectral cutoff of EOS to be dramatically extended to shorter wavelengths. In theory, the highest detectable frequency Ω of the test field can be calculated as $\Omega = \omega_{LO} - \omega_p$, where ω_{LO} and ω_p are the highest and lowest frequencies within the probe spectrum, respectively.

The detection scheme can be realized using a projection of the band-pass filtered light onto crossed polarization axes, causing interference of the LO and SFG, which depends on the strength and direction of the field oscillation. The projection itself can be done without a quarter-wave plate but through the rotation of the Wollaston prism by an angle of $45°$ to the input probe polarization. In analogy to the THz detection, a balanced photodiode is placed to measure the photocurrent and retrieve the electric field as a function of the time delay between two pulses. It is worth noting that balanced detection predominantly eliminates technical noise like laser fluctuations. The heterodyne detection can be performed
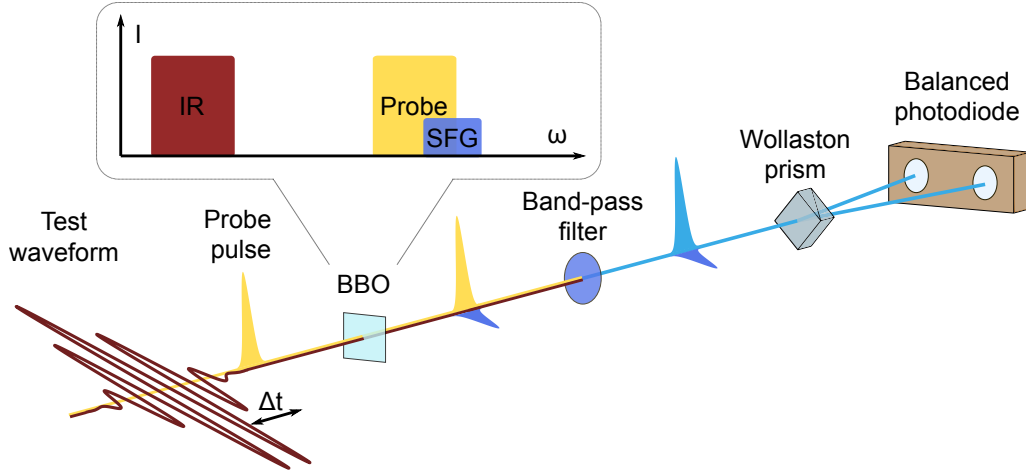
Figure 1.9: High-frequency time-domain electro-optic sampling.

through a lock-in amplifier with an amplitude or phase modulation of the test field using an optical chopper or a dedicated phase-controlling device, respectively (see Chapter 2).

One of the best materials for high-frequency EOS is beta-barium borate (BBO), which is commercially available and has broadband phase-matching characteristics, in addition to a high damage threshold. The generated SFG has an orthogonal polarization with respect to the probe pulse, under proper phase-matching conditions. In this matter, if the input test and probe beams have the same linear polarization and enter a BBO crystal with type-I phase-matching on the *o*-axis, the output SFG will be generated on the *e*-axis. A similar situation arises when the test and probe pulses are incident onto the crystal on the *e*-axis and *o*-axis, respectively, and a type-II BBO crystal is employed (Fig. 1.9). Correspondingly, a circularly polarized test field can be sampled, as well, using a combination of two measurements with type-I and type-II EOS crystals.

Introduced by Porer et al. [95] in terahertz EOS, spectral filtering facilitates extreme noise suppression and dramatic enhancement of the sensitivity of the system by eliminating the portion of the sampling light and SFG that is irrelevant and outside of the respective spectral window. Furthermore, the response function $R(\omega)$ of the detection system can be recalculated based on the transmitted spectrum and the material response of the photodiodes, allowing the frequency response $S(\Omega)$ of EOS to be determined [17]

$$S(\Omega) = \int_{\Omega}^{\infty} d\omega_{LO} R(\omega_{LO}) |E(\omega_{LO})| |E(\omega_{LO} - \Omega)| e^{i[\phi(\omega_{LO}) - \phi(\omega_{LO} - \Omega)]}, \qquad (1.49)$$

where $|E(\omega)| e^{i\phi(\omega)}$ is the complex spectral amplitude of the probe pulse. Thus, the detection bandwidth can be significantly shifted to higher frequencies. The application of spectral filtering has enabled the drastic extension of the bandwidth of the EOS technique first to 230 THz [17] and then to 450 THz with an appropriate sampling pulse in the ultraviolet-visible range [94]. However, the detection is valid only when the group delay dispersion

of all involved spectral components in the sampling spectrum is minimal, allowing for the coherent superposition of signal contributions. With the fulfillment of this requirement, a cost-efficient and compact setup with the large dynamic range for metrology measurements can be directly applied to light sources in the telecom and optical bands such as erbium-doped fiber laser or Ti:Sapphire-based laser systems, to temporal waveforms of which only attosecond streaking [11] and petahertz optical oscilloscope [96] previously had access. In addition, with high-frequency EOS, our research group has investigated the underlying interaction of light with a solid in the strong-field regime, revealing the exact timing of charge carrier injection that is confined within one optical cycle [13].

1.3.2   Extension to an Imaging Geometry

One particularly intriguing feature related to EOS is that the interaction of the test field and the sampling pulse is an exclusively optical process, which leads to the transferring of full information about one of the fields into the polarization state of another. It means that the dependence of the test field on the spatial coordinates is also recorded and carried by the band-pass filtered light. However, in the conventional time-domain EOS setup, the balanced photodiode simply averages this co-propagating spatial information by integrating and converting the incident intensity into a photocurrent. Alternatively, the underlying spatio-temporal interaction of two beams can be resolved through a standard imaging configuration, providing absolute space-time characterization or mapping of the field in the form that it constitutes in the EOS crystal [97–101].

Two-dimensional EOS imaging has been introduced in 1996 by Wu et al. [102], where spatial features of the amplitude and phase of terahertz beams have been extracted. This metrology technique enables the characterization of THz pulses even with complex structured spatial profiles including Bessel and vortex beams [103, 104]. A particularly interesting application of the THz EOS imaging has been found in near-field experiments, where sub-wavelength plasmonic structures can be resolved in a scanning probe configuration [105–107] or wide-field geometry without probe scan [108–112], including the detection of highly dynamic biological samples in real time under the illumination of THz irradiation. Currently, a spatial resolution reaching $\lambda/600$ is achieved in the THz range [113].

The primary mission of the current thesis is the transfer of the fundamental principles of THz two-dimensional EOS imaging to the new spectral ranges like near-infrared and visible using already established mechanisms of conventional time-domain EOS described in the previous subsection. The experimental layout of the high-frequency electro-optic imaging (EOI) is depicted in Fig. 1.10. For the description of EOI, a sampled field is assumed to contain frequencies in the near-infrared region (up to 230 THz) and a sampling pulse is a broadband white light with the spectral range of 500-1000 nm [17]. The extension to visible frequencies (up to 450 THz) requires a sampling pulse to also cover the ultraviolet (300-600 nm) [94]. It can be seen in Fig. 1.10 that the concept of imaging closely follows the standard time-domain EOS: the nonlinear interaction of ultrashort sampling white-light pulse and broadband NIR field generates an SFG pulse in the BBO crystal, leading to a polarization rotation of the spectrally overlapped region.
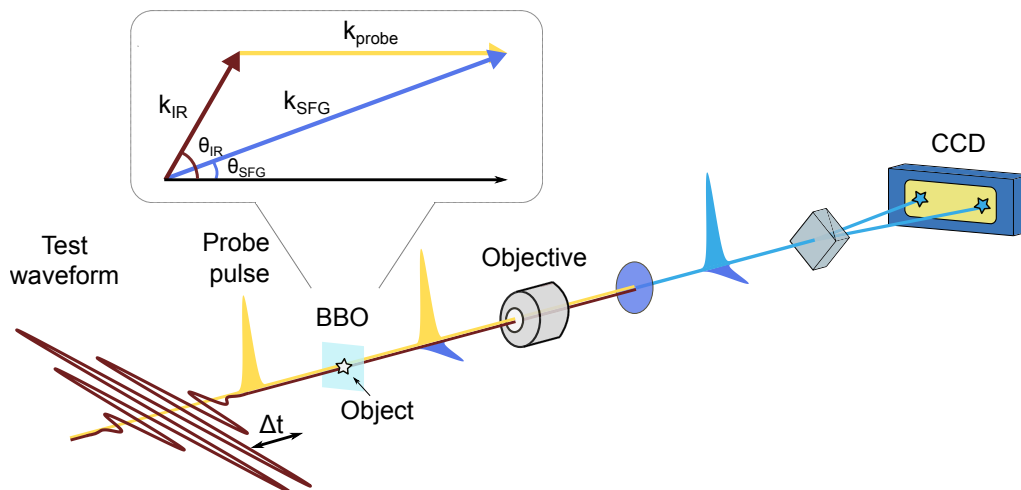
Figure 1.10: Extension of electro-optic sampling to an imaging geometry.

From the spatial perspective, a spatially inhomogeneous NIR field induces a spatially-varying rotation of the polarization in the pass-band filtered light. To resolve this rotation in space, a standard imaging setup incorporating an objective lens and a CCD camera can be built, with the insertion of a polarizing beamsplitter in between. The CCD camera records two images with orthogonal polarizations, after subtraction of which an electric field image can be obtained with an individual temporal waveform in each pixel. Such a simple imaging configuration is capable of enabling applications that take advantage of spatio-temporal reconstruction of ultrashort pulses. The EOI field characterization of few- and sub-cycle pulses in the near-infrared and visible regimes is presented in Chapter 3.

More importantly, near-field detection can be directly transferred to the new spectral regions, with accompanying advantages of the high-frequency EOI. Many challenges common in the THz range, including weak laser sources and the influence of harmful strain-induced birefringence in the EOS crystal, are overcome by the shift to shorter wavelengths, where relatively strong irradiation is widely available. For near-field detection of a nano object (the star in Fig. 1.10), the sample must be deposited on a sufficiently thin EOS crystal [114] and illuminated by a broadband NIR radiation. High spatial-frequency components produced by the object may still interact in the crystal with a probe pulse right after the excitation. In this case, the near-field information is recorded through SFG with the broadband white-light probe pulse and extracted as a function of the time delay between the two pulses. As a result, the probe pulse propagates to the far-field and produces a near-field image using the imaging system. The spatial resolution is independent of the illuminated test wavelength and determined by the diffraction limit of the LO frequencies.

The ability to resolve sub-wavelength nanostructures in real-time over a wide area from the mid-infrared to visible spectral regions can potentially find a variety of applications in the field of photonics, micro-optics, and biology. A proof of principle of the EOI near-field detection, working in the near-infrared, is demonstrated in Chapter 5.

Nowadays, diverse experiments either in the temporal dimension (time-domain spectroscopy) or spatial dimension (microscopy) are regularly performed in labs throughout the world. However, the integration of temporal measurements into the spatial domain is generally a challenging task. High temporal resolution provided by extremely short pulses implies the occurrence of chromatic aberrations in conventional light microscopy due to the large bandwidth. On the other hand, many state-of-the-art super-resolution imaging systems cannot be adapted to ultrafast measurements in the time domain.

The imaging apparatus based on the EOS technique in the high-frequency regime contains fascinating features compared to the conventional imaging systems including direct integration of time-space experiments with simultaneously sub-wavelength spatial and sub-cycle temporal resolution. It originates because the frequency upconversion relying on the nonlinear interaction leads to the compression of information about the entire bandwidth of the incident test field. In the case of the broadband NIR field, all frequency components are encoded into a relatively narrowband SFG pulse and retrieved by changing time delay. As a result, due to the nonlinear interaction in the crystal, only this narrowband light is exploited after spectral filtering, which carries complete information about the broadband NIR field (see inset of Fig. 1.9). This is especially profitable in the EOS imaging configuration: optical adverse effects like chromatic aberrations are strongly eliminated. Thus, a platform for measurements with high temporal resolution can be established with the use of incredibly short few femtosecond pulses containing octave spanning bandwidth. The EOI technique provides a great opportunity to conduct pump-probe experiments with incredibly high temporal and spatial precision at once (Chapter 5).

The second important advantage of EOI compared to other traditional imaging systems is expressed in momentum conservation during SFG. As depicted in the inset of Fig. 1.10, the diffraction angle of the NIR waves after the interaction with a sample can be extremely large. In the EOI apparatus, the numerical aperture is determined not by the scattered NIR wave vectors but the emerged SFG wave vectors, which have a significantly smaller angle due to the momentum conservation. Under proper phase-matching conditions in the EOS crystal with large acceptance angle and broadband properties, the reduction of the required numerical aperture can be achieved compared to the classical case when the object is imaged directly by the NIR waves.

More details and experimental tricks of the imaging system for a specific application can be found in the next chapters of the thesis.

1.4   Introduction to Metasurface Optics

The purpose of the current section is to present a brief introduction of light propagation through a material interface consisting of subwavelength-spaced nanoantennas and the resultant behavior of pulses transmitting through them. In the experimental part of the thesis, a couple of metasurface samples are utilized to shape an incident light pulse and generate complicated electric fields (Chapter 4). In this matter, basic operational principles of metasurface optical devices are good to be familiar with. A great theoretical and
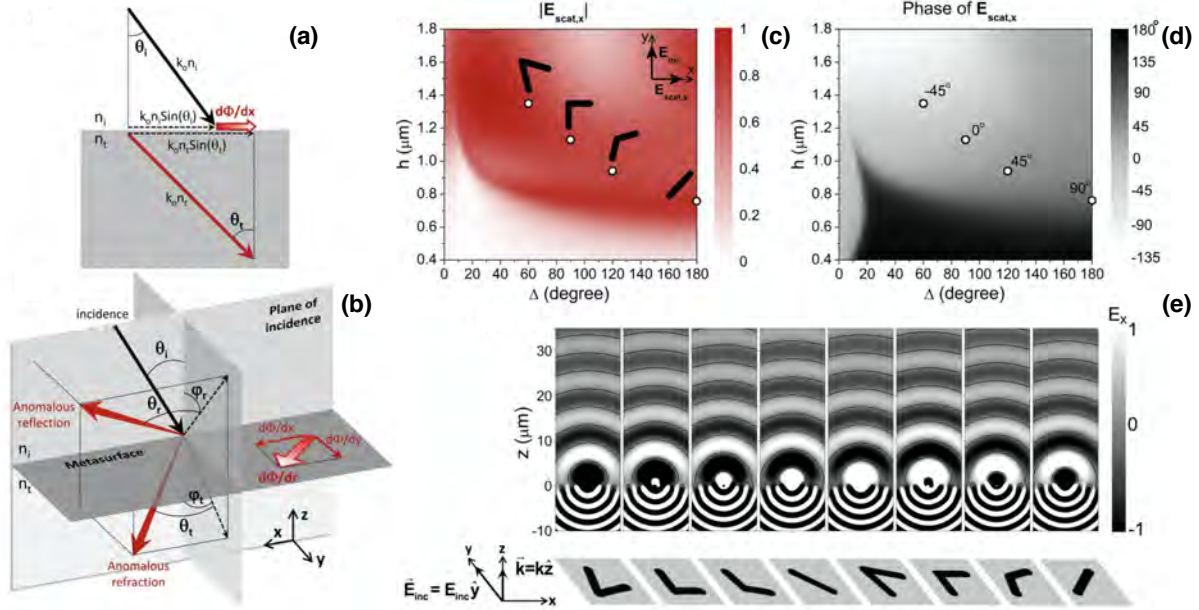
Figure 1.11: Basics of the metasurface lens theory. The interface between two media obeys the generalized Snell's law, where a constant phase gradient **(a)** $d\Phi/dx$ in the 2D case and **(b)** $d\Phi/dr$ in the 3D case represent an effective wavevector. Each gold antenna provides **(c)** nearly identical amplitude of the scattered electric field and **(d)** incremental phases of $\pi/4$. **(e)** Simulation of the wavefront propagation for each unit. Figure adapted from [116].

practical overview of light propagating with phase discontinuities can be found in [115, 116], which will be the basis for the present thesis for the description of metasurface optics and their ability to control light properties in the far-field.

Unlike traditional optical elements that rely on gradual phase changes along the optical axis, abrupt phase shifts yield an extra degree of control over the characteristics of light. In fact, the light propagation with phase discontinuities obeys Fermat's principle, with an abrupt phase shift $\Phi(\mathbf{r})$ that depends on the radial position of the interface. Then, assuming a plane wave incident with an angle θ_i on an artificially structured interface and refracting with the angle θ_t (see Fig. 1.11a), the 2D generalized Snell's law of refraction can be derived in the form [115]

$$n_t\sin(\theta_t) - n_i\sin(\theta_i) = \frac{1}{k_0}\frac{d\Phi}{dx}, \tag{1.50}$$

where $d\Phi/dx$ is the interfacial phase gradient, which lies in the metasurface plane, n_i and n_t are the refractive indices of the media, k_0 is the wave vector in vacuum. In the three-dimensional case (Fig. 1.11b), Eqn. 1.50 is complemented by [116]

$$\cos(\theta_t)\sin(\phi_t) = \frac{1}{n_t k_0}\frac{d\Phi}{dy}, \tag{1.51}$$

where ϕ_t is the refraction angle in the plane perpendicular to the incident. The same generalized Snell's law equations can be obtained for the case of anomalous reflection [117]:

$$\sin(\theta_r) - \sin(\theta_i) = \frac{1}{n_i k_0}\frac{d\Phi}{dx}, \qquad (1.52)$$

$$\cos(\theta_r)\sin(\phi_r) = \frac{1}{n_i k_0}\frac{d\Phi}{dy}, \qquad (1.53)$$

where ϕ_r is the reflection angle in the plane perpendicular to the incident. It can be seen from the equations that the phase gradient $d\Phi/dx$ or $d\Phi/d\mathbf{r}$ represents an effective wave vector that is imparted on the refracted or reflected light, leading to the wave vector conservation along the interface. The phase gradient can be obtained by placing an array of inhomogeneous resonators with sub-wavelength separation. However, a portion of the incident light does not experience such extraordinary propagation effects but follows the conventional Snell's law in areas between the resonators. The efficiency of metasurface optics can be controlled by changing the distance between the nano-scatters.

The interface can be made of different types of resonators such as plasmonic antennas [118], collection of nanoparticles [119] or electro-magnetic cavities [120]. The plasmonic antennas are the most common elements for manufacturing metasurface optics due to their versatile optical characteristics and ultrathin structure. Inside a meta-structure, the incident light excites plasmonic resonances on the surface of the antennas. The resulting amplitude and phase delay of the scattered light depend on the incident polarization and the parameters of the antenna. The amplitude of the transmitted light is typically tuned to be maximally similar for each antenna by accurately choosing their shapes.

In [115], the authors implemented an analytical calculation of the interaction of eight different V-shape nano-antennas with the incident light linearly-polarized along the y-axis, which can excite symmetric and antisymmetric modes. The nano-structured antennas comprise two arms of equal length h forming a V-shape with an angle Δ (see Fig. 1.11e). The propagation of the E_x component of the scattered field is simulated along the z-axis. It can be seen from the numerical simulation that parameters of eight various types of V-antenna are chosen in such a way that the phase shift between two adjacent antennas is $\pi/4$, which corresponds to a distance of 1 µm in that case. This provides the entire phase manipulation of the light from 0 to 2π with such eight nano-structures. In Fig. 1.11c, it is demonstrated that an accurate selection of different values of h and Δ may lead to a nearly identical amplitude of the scattered field E_x, providing a phase shift of 45° (Fig. 1.11d). With this incredible control, it is possible to shape any wavefront of interest.

One of the intriguing prospects of modern metasurface optic design is a production of ultrathin flat samples that can perform similarly to standard refractive optical elements but without the disadvantages inherent to them. Primarily, it relates to spherical aberration, which significantly deteriorates imaging measurements unless complex optical systems are applied to mitigate aberrations. Although many exciting meta-optical elements have been recently demonstrated with innovative features [121–125], in the present thesis, the emphasis is put on two principal ultrathin samples: a flat lens and a flat axicon [126].
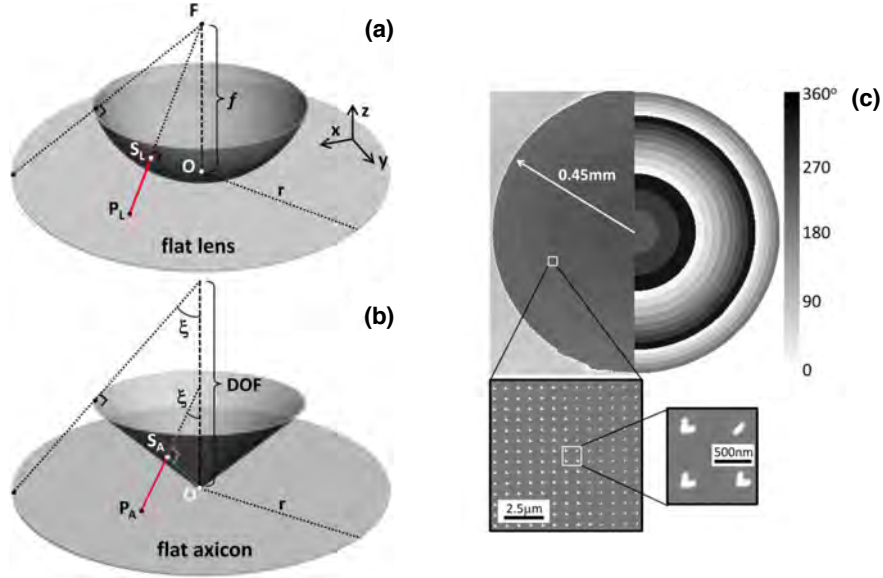
Figure 1.12: Design concept of flat lenses and axicons. **(a)** Hyperboloidal phase profile created by a meta-lens. **(b)** Conical phase profile created by a meta-axicon. **(c)** Typical structure of a meta-lens with discretized phase profile by eight antennas across the surface. Figure adapted from [116].

A conventional glass lens imparts a hyperboloidal phase profile on an incident light field. In analogy, to design a flat focusing lens, abrupt phase shifts produced by nano-antennas must follow the same profile, constructively interfering in the focal plane. Therefore, a flat lens with a given focal length f introduces a phase shift $\phi_L(x,y)$ on the incident light of wavelength λ on every point of the lens surface $P_L(x,y)$ (Fig. 1.12a) according to the following condition [116, 126]:

$$\phi_L(x,y) = \frac{2\pi}{\lambda}\overline{P_L S_L} = \frac{2\pi}{\lambda}\left(\sqrt{x^2 + y^2 + f^2} - f\right), \qquad (1.54)$$

where S_L is a projection of P_L onto the spherical surface with a radius of f. For a flat conical lens, often referred to as an axicon, the imparted phase profile $\phi_A(x,y)$ must be conical, in order to convert an incident Gaussian beam into a non-diffracting Bessel beam (Fig. 1.12b):

$$\phi_A(x,y) = \frac{2\pi}{\lambda}\overline{P_A S_A} = \frac{2\pi}{\lambda}\sqrt{x^2 + y^2}\,\sin(\xi), \qquad (1.55)$$

where S_A is a projection of P_L onto the conical surface, ξ is the angle of the axicon, $\xi = r/\text{DOF}$, r is the radius of the metasurface axicon and DOF is the depth of focus. In Fig. 1.12c, a typical flat lens design is depicted. An array of meta-structures are placed on a surface of a dielectric in a way that the phase shifts across the interface cover full range from 0 to 2π radians using eight types of V-nanoscatters.

The local phase shifts designed with a subwavelength spatial precision have already strongly redirected the future of optical components, offering an unprecedented level of light manipulation. However, to measure the electric field in both space and time and test the performance of such metasurface device, a spatio-temporal metrology technique capable of resolving contemporary few-cycle laser pulses is required. This also applies to more complex-structured flat samples with a complicated electric field at the output, including multi-bound fields. This is one of the interesting applications of the electro-optic imaging system, which can help facilitate the design of metasurface optical elements with novel light control characteristics. The spatio-temporal characterization of electric fields, shaped using a flat lens and a flat axicon, is shown in Chapter 4.

Chapter 2

Experimental System

The present chapter partially describes the laser sources and experimental tools of the work done in this thesis. The setup is located in the Laboratory of Attosecond Physics at the Max Planck Insitute of Quantum Optics in Germany. The complex OPCPA laser system based on three amplification stages [127] has been utilized in different experiments such as high harmonic generation [128] or light-wave synthesis [94]. These experiments are extremely sensitive to any types of fluctuations and laser drifts and, as a result, they were suffering from frequent instabilities of the light source. The system has been recently rebuilt with only two amplification stages, introducing some major improvements that mostly affect the stability and reliability of the output beams [129].

An imaging system, based on the EOS method, is developed in ambient conditions, with a possibility to be easily moved and integrated with other experiments, showing the flexibility and compactness of the setup. As EOI traditionally suffers from poor sensitivity, which has been the biggest disadvantage of the technique, two completely new approaches to solve the issue are implemented in the work, making EOI applicable even under extremely noisy conditions. The entire procedure for the retrieval of a final electric field image is discussed in this chapter along with the limits of the temporal and spatial resolution.

2.1   Phase-Stable 1.9 µm Laser Source

The laser system is a passively phase-stable OPCPA [43, 44], which produces 1 mJ, 14 fs near-infrared pulses centered at 1.9 µm through intra-pulse DFG in BBO. The use of such relatively long wavelengths in high harmonic generation has enabled the emitted spectrum to achieve cut-off energies that were difficult to reach before [128]. With this laser source, access to incredibly short 4.5 fs pulses has been accomplished through the dramatic broadening of the NIR light in a hollow-core fiber (HCF) followed by light synthesis [94]. Here, these sub-two-cycle waveforms are utilized to study the spatio-temporal structure of pulses as well as microscopic effects of nanoscale samples that are resonant at this wavelength. In theory, a lithium thiogallate (LGS) crystal can be adapted to shift the research field to the molecular fingerprint region, in the the mid-infrared [130].

Seed and Pump Generation
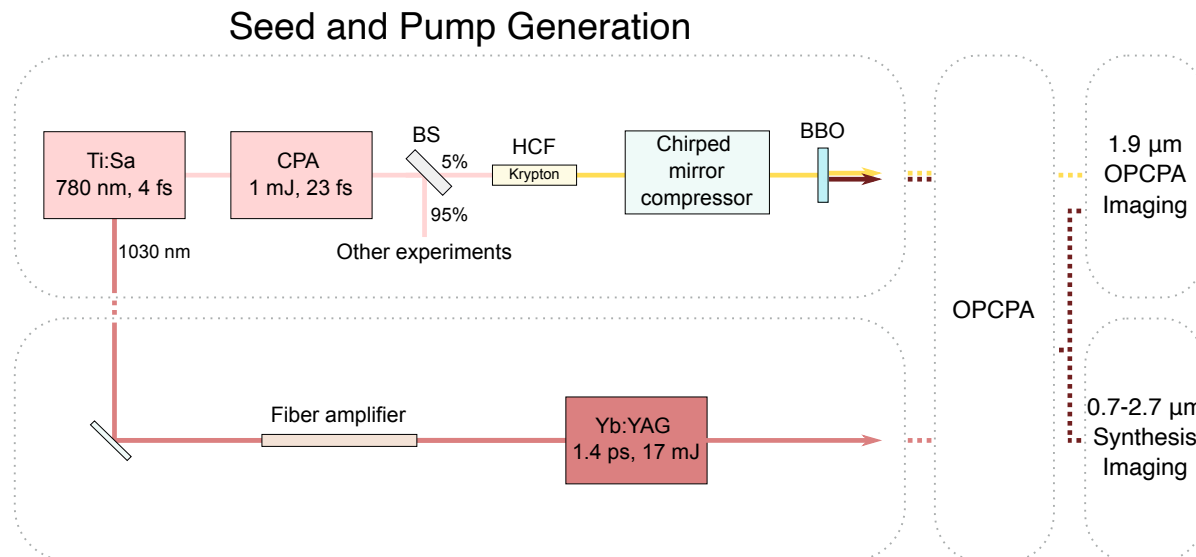
Figure 2.1: Seed and pump generation. Both the seed for CPA and the seed for Yb:YAG thin disk amplifier are generated in the same Ti:Sa laser source, providing intrinsic temporal synchronization between DFG and the pump for the OPCPA.

2.1.1   Seed and Pump Generation

A commercial Ti:Sapphire oscillator (Femtolasers, Rainbow II) generates 4 fs pulses with 3.5 nJ pulse energy at 78 MHz repetition rate. The output spectrum centered at 780 nm was additionally modified to include a narrowband output at 1030 nm wavelength for the pump laser (Figure 2.1).

The oscillator provides the seed for a multi-pass Ti:Sapphire CPA (Femtopower Pro), which produces 1 mJ pulses with 23 fs pulse duration at 3 kHz repetition rate. 5% of the output (60 µJ) is focused into a krypton-filled HCF with the length of 280 mm and an inner-core diameter of 140 µm. Broadened with the efficiency of 60% via self-phase modulation, the pulses cover the 500-1000 nm spectral range, allowing for pulse compression with a chirped mirror compressor down to 4 fs duration. Such short white-light pulses provide optimal conditions for intra-pulse DFG using a 500 µm thick BBO crystal with type II phase matching [131]. The generated NIR continuum has orthogonal polarization to the visible pulses and relatively weak nJ energy. The DFG spectrum spans nearly one octave, from 1.4 to 2.6 µm region, and it is subsequently used as a seed in the OPCPA. A significant advantage of the DFG process for seed generation is the intrinsic CEP stability, granting a necessary condition for CEP sensitive experiments such as HHG or EOS [132]. The standard deviation was calculated based on measurements of the CEP using an f-2f interferometer taken over a 1 hour time period, with the resulting value of 64.7 mrad [129].

A special dichroic beam splitter separates the spectral region around 1030 nm of the oscillator output which is then preamplified in a fiber amplifier (Tünnermann group, FSU Jena). The amplified pulses with 0.4 nJ energy seed a Ytterbium-doped Yttrium Alu-
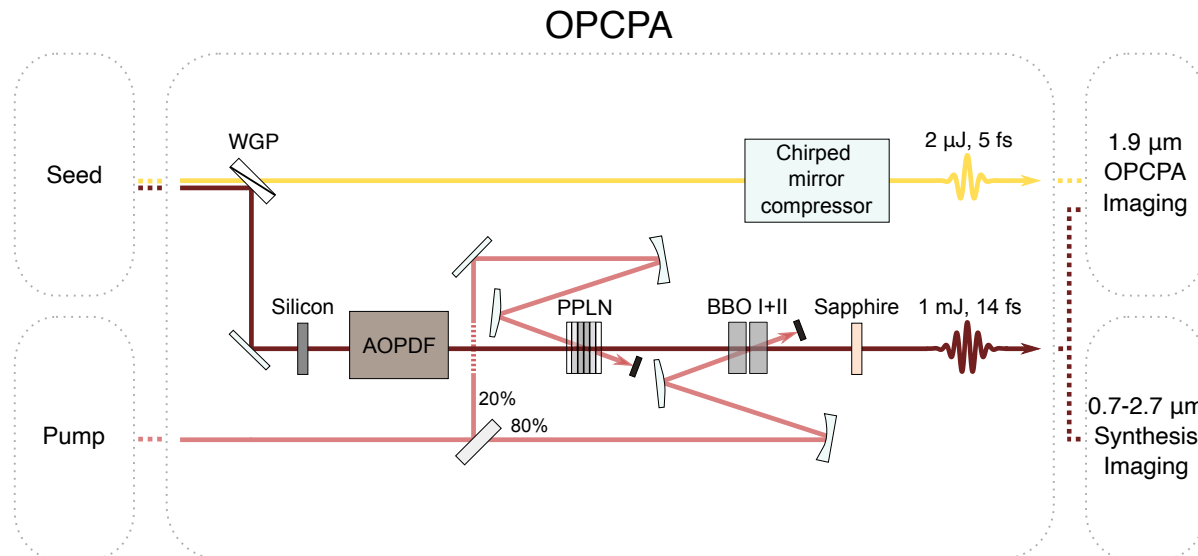
Figure 2.2: New hybrid OPCPA configuration delivers phase-stable 1 mJ pulses centered at 1.9 µm with 14 fs time duration. Residual white light is recompressed to 5 fs and used as a probe in EOS imaging experiments.

minium Garnet (Yb:YAG) thin-disk regenerative amplifier [133]. The thin-disk amplifier emits a train of 17 mJ pulses at 3 kHz repetition rate. A reflective grating compressor is used to compress the output pulse to 1.4 ps for utilization as a pump in the OPCPA stages [134]. A great benefit is provided by the fact that both seed pulses for the CPA and the thin-disk amplifier are generated by the same Ti:Sa oscillator, yielding intrinsic temporal synchronization between DFG seed and the pump of the OPCPA. To compensate for slow temporal drifts and fast jitter, an active temporal stabilization is realized along with a pointing stabilization system (TEM Messtechnik, Aligna) [135].

2.1.2 OPCPA Setup

The generated DFG seed pulses centered at 1.9 µm wavelength are separated from the residual white light pulses using a broadband wire-grid polarizer (WGP) (Figure 2.2). A 5 mm silicon window is placed in the seed path to introduce a positive chirp to the pulse and increase the efficiency of the OPCPA process. One of the most important components of the optical layout for all the work presented in the thesis is an acousto-optic programmable dispersive filter (AOPDF) (Dazzler, Fastlite) that provides full control of the spectral phase of the amplified pulses, including adjustment of higher-order dispersion. The AOPDF also benefits from the stretched input pulse by reaching the maximum efficiency of 10 %.

The new OPCPA configuration consists of only two stages that are pumped by the thin disk amplifier. The unamplified DFG spectrum is depicted in Fig. 2.3a. The first stage is based on a 5% Mg-O doped periodically poled lithium niobate (PPLN) crystal pumped with 3 mJ pulse energy (20 %). The PPLN crystal is 1 mm thick and enables the pulse
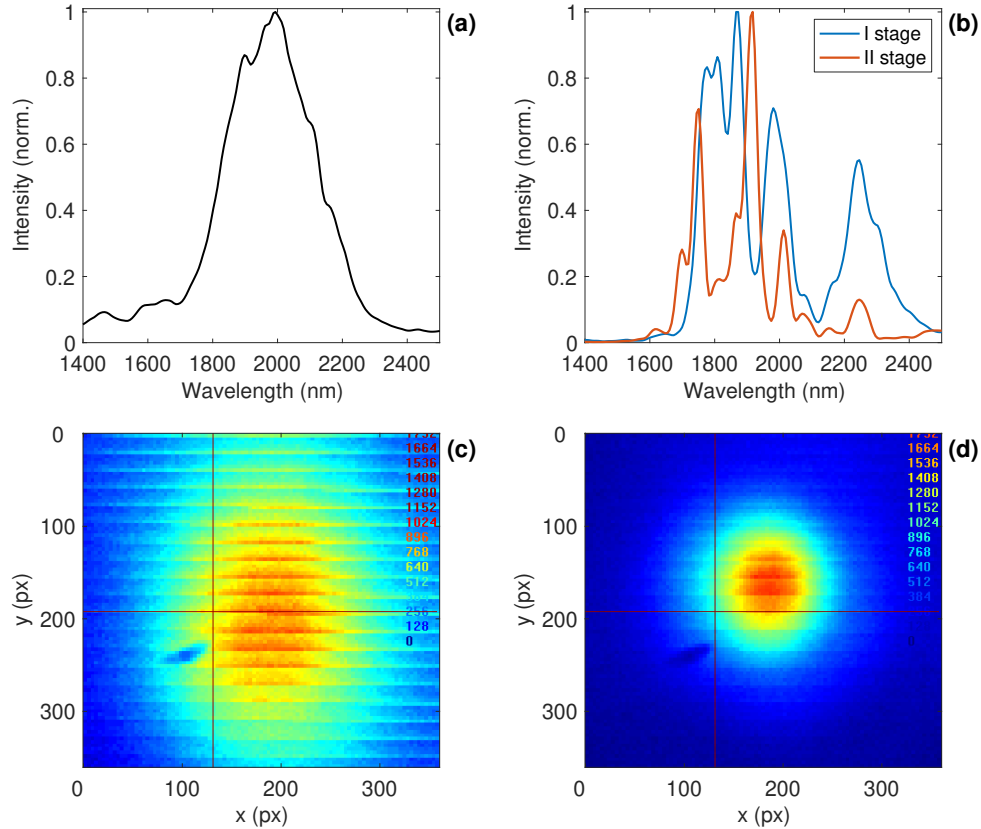
Figure 2.3: Output parameters of the OPCPA stages. **(a)** DFG spectrum before amplification in the OPCPA. **(b)** Amplified spectra and **(c)**, **(d)** mode of the beam after the first (PPLN crystal) and second (stacked type-I and -II BBOs) stages, respectively.

energy of the 1.9 µm seed to be increased to 40 µJ. The output continuum covers the range from 1.5 µm to 2.6 µm, which is shown with the beam profile in Fig. 2.3b and Fig. 2.3c.

The achievable power of the pulse in the second stage can lead to damage to the crystals utilized for the amplification. Although PPLN crystals support exceptional amplification bandwidth, they are delicate and can be easily damaged under relatively low intensities, without a possibility of being manufactured in larger apertures, to allow spatial expansion of the beam. A bulk lithium niobate ($LiNbO_3$) crystal is one of the alternatives and, in the original version of the setup, it was used to amplify the final stage of the OPCPA [127, 136]. Recently, the second stage has been completely redesigned based on two stacked BBO crystals with type-I and type-II phase-matching angles, which together provide a similar bandwidth as the $LiNbO_3$, reducing photorefraction and shifting the amplified spectrum to the blue side [129]. The BBO-I and BBO-II crystals with 4 mm and 5 mm thickness, respectively, are pumped with 14 mJ (80 %) of the thin disk laser, increasing the seed pulse energy to 1 mJ. The output spectrum covers the range from 1.5 µm to 2.6 µm (Fourier transform limit ∼12 fs), which is shown with the beam profile in Fig. 2.3b and Fig. 2.3d. The compression of the OPCPA pulses is achieved with a 10 mm thick sapphire window,

which has negative GDD in the required spectral range. To attain nearly Fourier-limited two-cycle pulses of 14 fs, the AOPDF is adjusted to finely tune the compression.

The white light pulses, after passing through the DFG BBO, WGP, and propagating in air, are recompressed again using a chirped mirror compressor and a pair of fused silica wedges to 5 fs. The pulses in this state are short and broadband enough to serve as a probe for EOS of the NIR OPCPA electric field in both time [17] and space domains.

2.2 Electro-Optic Imaging

All further description of the optical layout refers primarily to the full electric field reconstruction with electro-optic imaging in the near-infrared, with the extension to the visible spectral region using an already existing light-wave synthesizer [94].

In the present work, standard time-domain EOS is applied first to characterize and compress the broadband NIR pulses under investigation. The time-domain EOS setup consists of a Wollaston prism tilted at 45 degrees to the input probe polarization and a pair of home-built balanced photodiodes. CEP modulation from 0 to π with the AOPDF introduces a frequency comb shift of the 1.9 µm pulse, which enables heterodyne detection of the given signal at 1.5 kHz reference frequency using a lock-in amplifier (SR830, Standford Research Systems). The switching from the conventional EOS to the imaging apparatus can be implemented by flipping a mirror after the EOS crystal.

2.2.1 Near-Infrared OPCPA Pulses

Here, imaging system is described in the application to the detection of the OPCPA output pulses (Fig. 2.4). The NIR beam is focused using a lens, which is either a BaF_2 lens with FL=100 mm (Chapter 3) or metasurface lenses (Chapter 4). In conventional EOS, both probe and test arms are usually focused with similar focal spots. In contrast, EOI requires a larger cross-section of the probe compared to the test field to fully resolve the spatial distribution of the electric field. For this purpose, a telescope for the white-light beam was built, producing a focus of ~ 300 µm $(1/e^2)$. The data demonstrating the usefulness of the telescope will be shown in Chapter 3. The time delay between the two pulses is regulated by a linear piezo stage (SLC, SmarAct) in the probe arm. A 100 µm thick type-II BBO crystal (EKSMA Optics) is placed in the focus of both beams, after their collinear combination in a broadband WGP (LOT-QuantumDesign). Phase-matched SFG is imaged using a 4x infinity-corrected microscope objective with NA=0.1 (RMS4X, Olympus, Plan Achromat). The infinite conjugate objective produces an image at infinity, allowing for the introduction flat optical components in the beam path between the objective and a tube lens, that is used to produce the final image on a camera. A band-pass filter is placed to isolate spectral region of 500-550 nm, where SFG overlaps with the probe light (LO). As previously described, this enables the additional improvement of the signal-to-noise ratio (SNR) of the EOS system. Similarly to the Wollaston prism, a second WGP at a 45° angle is utilized to split the beam into two arms with mutually orthogonal polarization
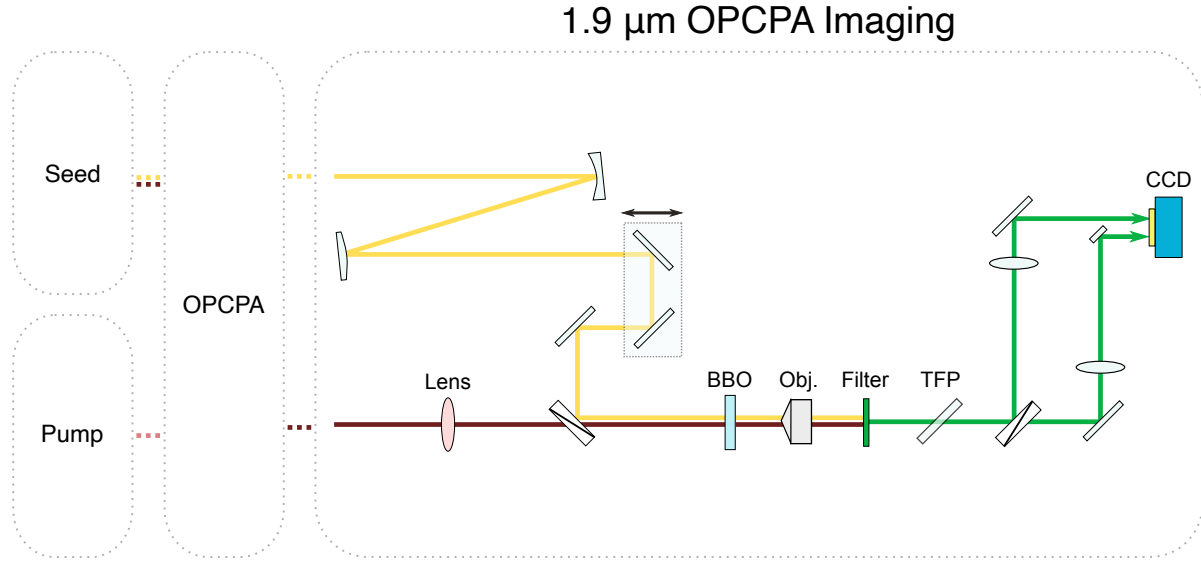
Figure 2.4: Optical layout of electro-optic imaging with the 1.9 µm OPCPA pulse. The interaction of the test NIR and probe fields in the BBO is imaged on the CCD camera by a microscope objective and a tube lens for each polarization arm.

(henceforth: a and b images). The WGP is a great instrument for this work, as it has a wide acceptance angle and excellent polarization performance. The resulting polarization images are focused on a CCD camera (Cinogy CinCam CCD-2302-UV) using a pair of tube lenses with FL=175 mm. The magnification M of the designed imaging system is $M = 4 \times 175/180 \approx 3.9$.

Due to a relatively low nonlinear coefficient of BBO, the imaging system is expected to suffer from poor sensitivity. Moreover, the cross-section of the probe in BBO is made to be larger than one of the NIR test beam to fully resolve. As a result, the probe pulse experiences spatially varying nonlinear upconversion. Boundary regions of the NIR cross-section generate significantly weaker SFG than the central peak. This leads to a spatial variation of the SNR, which increases the noise level of the entire image (see Subsection 3.1.2). Unlike standard EOS, a lock-in apparatus cannot be integrated with the imaging system to improve SNR of electric field images.

Two novel methods to enhance image contrast are implemented in the present work. The first approach incorporates a thin-film polarizer (TFP, 532 nm) [137]. The TFP enables an accurate manipulation of the amplitude of LO (s-polarization in the lab frame), while transmission of the SFG amplitude (p-polarization) is marginally affected. By tuning the rotation angle of the TFP, it is possible to achieve maximum interference of the leaking portion of LO with SFG. A similar technique was realized in EOS [138]. The effect produced by the TFP is equivalent to the use of the EOS crystal with a larger nonlinear coefficient. It results in better contrast and cleaner images on the CCD. As a TFP primarily operates in a narrowband spectral range, a tandem with the band-pass filter makes it perfectly suitable for EOS. Measurements confirming the benefit of the TFP will be shown in Chapter 3.

The second approach involves the AOPDF and its ability to control and assign a required CEP of the NIR pulse. After the subtraction of a and b images with crossed polarization (by analogy with balanced photodiodes), the noise coming from drifts and instabilities of the laser source is eliminated, as both images are captured simultaneously. However, spatial misalignment and small geometrical mismatch of the a and b images due to the different propagation paths can also induce noise of the system (see Fig. 2.6 in the next section). The AOPDF allows the removal of this mechanical noise, additionally increasing the resultant contrast. To fulfil this goal, the a and b images should be captured for both CEP $= 0$ and CEP $= \pi$ of the NIR waveform, recording in total four images for each time delay step. In principle, the information of the image a with CEP $= 0$ contains the same information as the image b with CEP $= \pi$, as well as the image b with CEP $= 0$ and the image a with CEP $= \pi$. In theory, it is possible to perform imaging with a single polarization arm, utilizing the AOPDF and assuming ideal stability of the laser system. Both approaches to improve the contrast of images in the EOI measurements are planned to be published in the near future.

2.2.2 Lightwave Synthesis

In addition to the amplified NIR pulses, the EOI technique is applied to spatially resolve the ultra-broadband synthesized fields, extending the bandwidth of this technique to wavelengths as short as 670 nm (450 THz). The synthesizer imaging is based on the already existing EOS setup, capable of detecting synthesized pulses in the temporal domain [94].

The 14 fs NIR laser pulse with the full power after the OPCPA is focused into a HCF with 240 µm inner diameter filled with ambient air (Figure 2.5). Active pointing stabilization of the NIR beam is realized to maximize the stability and reproducibility of the output light. Broadened supercontinuum after the fiber spans more than three optical octaves, from 300 nm to 2.7 µm, which is subsequently split into three spectral channels - zeroth channel (CH0, central wavelength of $\sim$ 450 nm), first channel (CH1, $\sim$ 1.2 µm) and second channel (CH2, $\sim$ 2.1 µm) - for the compression through different materials and chirped multilayer mirrors, designed individually for each channel.

The higher frequencies (CH0) are separated first by a dichroic beam splitter and compressed with a chirped mirror compressor to 2 fs to function as a sampling pulse for EOS. IR synthesis is performed using the two remaining channels (CH1+CH2) with a delay stage for each channel and produces sub-cycle transients at $\sim$ 1.8 µm with the shortest achieved pulse duration of 4.5 fs (Fourier transform limit is $\sim$ 3 fs). After compression, the channels have 53 nJ (CH0), 0.37 µJ (CH1) and 1.27 µJ (CH2) pulse energies, respectively. A telescope is placed in the CH0 path to create a larger focus spot compared to the IR synthesis arm, which is focused by an off-axis aluminum parabolic mirror with FL=100 mm. The dichroic beam splitter combines the two arms for electro-optic detection with a 100 µm thick type-I BBO crystal. The emitted SFG signal is imaged using a 4f imaging system, consisting of a UV lens with FL=200 mm and a pair of UV tube lenses with FL=175 mm (unfortunately, no UV microscope objective was at hand at that moment). The light is band-pass filtered (290-350 nm) and divided into two arms with crossed polarization by a

0.7-2.7 µm Synthesis Imaging
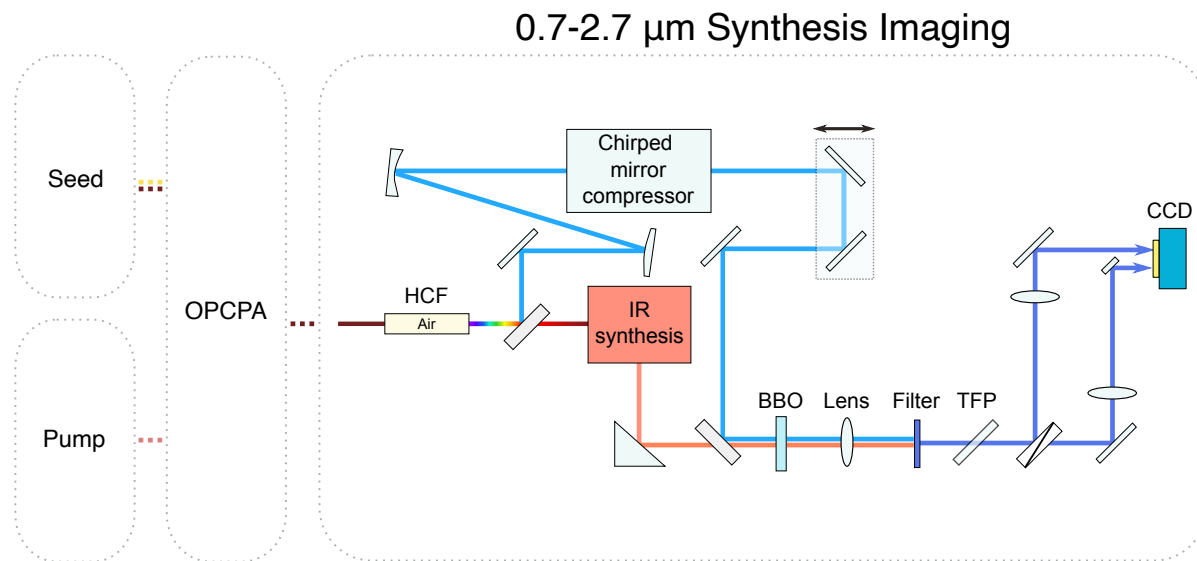
Figure 2.5: Optical layout of electro-optic imaging with the pulse synthesis. After pulse broadening in an air-filled HGF, higher frequencies (CH0) are separated and compressed to 2 fs to be utilized as a probe pulse for EOS imaging. IR synthesis (CH1+CH2) produces pulses as short as 4.5 fs centered at 1.8 µm.

broadband WGP rotated by 45 degrees. A TFP plate (343 nm) is additionally set to improve SNR of extracted images. The CCD camera records resulting cross-polarized images in the focal plane of the tube lenses.

2.3   Image Acquisition and Resolution

In this section, all the steps to obtain a final image of the electric field are discussed. The scanning process consists of the following actions: 1) a CCD frame with a and b images is recorded while the CEP of the NIR pulse is set to zero. 2) A voltage is applied to a CEP module of the AOPDF to flip the CEP to π, and 3) another CCD frame is recorded. After capturing four images for one point of time delay, 4) the piezo stage is moved to the next delay point and the CEP is flipped back to 0. The entire procedure is repeated for all steps within the time delay window. The step sizes used for the OPCPA imaging and synthesis imaging are 0.5 µm (1.67 fs) and 0.24 µm (0.8 fs), respectively. During a scan, all data from the CCD are stored in the RAM of a PC to minimize acquisition time and then saved to the hard drive. A typical acquisition takes about 10 minutes with 30 averaged laser shots per data point, with the main limiting factor being the transfer speed of the CCD. For the measurements presented in the current work, only one CCD is utilized, providing enough pixels (5 MP with a 3.45 µm pixel size) to capture both cross-polarized images. For imaging systems with 20x and higher magnification, the use of two CCDs is necessary, assuming perfect temporal synchronization between them.
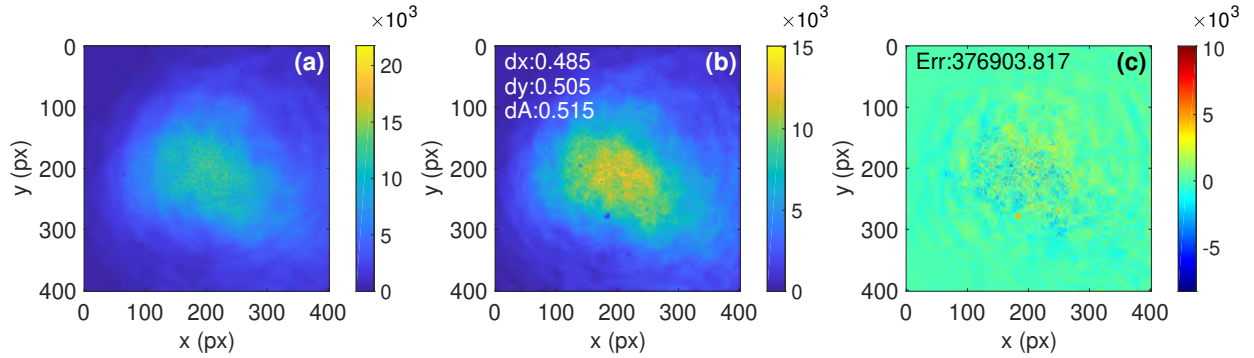
Figure 2.6: Alignment procedure of probe images with the test beam being blocked. **(a)** The first image on the CCD. **(b)** Numerical position shift and intensity correction of the second image. **(c)** Resulting difference image obtained by subtracting (b) from (a).

Two typical images of the probe light on the CCD with the test field being blocked are shown in Fig. 2.6. The second image (b) is numerically aligned to the first image (a) to produce a difference image (c), representing a frame of the electric field under study. Fine adjustment of the position shift (dx and dy) of the second image is realized in a sub-pixel level through the least-squares fitting procedure. Besides, an intensity multiplier (dA) is applied to reach the minimum error in (c). The error value is defined as

$$\text{Err} = \sqrt{\sum (a - b)^2}, \tag{2.1}$$

where a and b are the images (a) and (b) in Fig. 2.6. To prevent subtraction errors, a gate intensity level is used for the pixels of (a) and (b) images, below which values are set to zero. Furthermore, binning 2x2 is implemented in all measurements, expanding the sensitivity of the camera through a combination of four adjacent pixels into a single pixel. In addition, a spectral band-pass filter is numerically applied to obtain cleaner waveforms.

It is also highly important to analyze the spatio-temporal resolution limits of the built imaging system. Since EOI is based on the EOS technique, time resolution of the imaging apparatus is coupled to the duration and bandwidth of the sampling pulse, as well, reaching $\sim$2.2 fs after spectral filtering in the measurements with the NIR OPCPA electric field [17]. Currently, the best possible temporal resolution of EOS is measured to be $\sim$1 fs in the light-wave synthesis experiments [18]. In the space domain, as discussed earlier, the theoretical resolution is determined by the diffraction limit of high frequencies within the probe light. In practice, the resolution can deteriorate for many reasons, e.g. optical elements of the system or signal averaging in the EOS crystal. Therefore, a resolution analysis has to be accomplished, involving both the probe and test fields.

In the far-field imaging, we characterize the optical system with a standard resolution target, 1951 USAF, using only the band-pass filtered white-light beam. The resolution target, shown in Fig. 2.7a, is placed in the focus of the probe pulse and imaged by the 4x microscope objective (Fig. 2.7b). From the imaged pattern, the resolution of the imaging system is evaluated by extracting the corresponding spatial profile of a cross-section of the
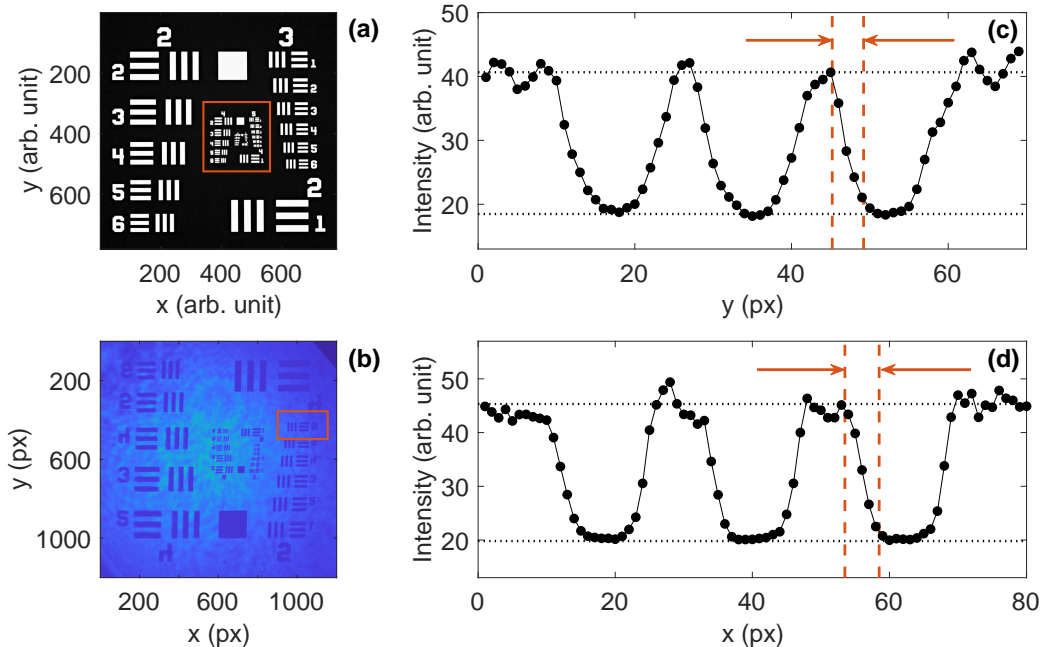
Figure 2.7: Evaluation of spatial resolution with a test target. **(a)** Resolution target sample, 1951 USAF. **(b)** Red square of (a) is imaged by the 4x objective. **(c)** Slice of red region of (b) with a resolution of ~ 3.5 µm, defined by varying intensity from 10% to 90%. **(d)** The same approach is applied to the target imaged with the 20x objective, resulting in a spatial resolution of ~ 0.9 µm.

red area with the intensity varying from 90% to 10%. The intensity values are averaged for all pixels along the pattern. For the OPCPA imaging setup with the LO spectrum of 500-550 nm range, these measurements are done for both 4x and 20x microscope objectives, with the resulting spatial resolution of ~ 3.5 µm (Fig. 2.7c) and ~ 0.9 µm (Fig. 2.7d), respectively. Synthesis imaging, utilizing the LO of 290-350 nm and the 4f imaging system, provides a spatial resolution of ~ 4 µm, due to the poor NA of the system. It has to be noted that the applied binning can make the actual resolution worse by a factor of 2.

In the measurements involving near-field detection, a test target should be characterized by an electron microscope. An important property of EOI is that the near-field effects can be resolved in a wide-field geometry with a resolution, independent of the exciting field wavelength. In this thesis, the approximate resolution with both the test and probe fields is evaluated through the deposition of sub-wavelength silver-coated microparticles on the EOS crystal and corresponding local field enhancement of the test light. The results will be discussed in Chapter 5.

Chapter 3

Spatiotemporal Metrology

New prospects to study the fundamental physics of light-matter interaction have been discovered with an ability to detect the measurable change that material encodes onto the amplitude and phase of the exciting pulse [6, 139, 140]. Direct access to the electric field has always been a challenge in the near-infrared or visible regimes, where pulse durations as short as a few femtoseconds can be reached. With the advent of novel metrology methods such as attosecond streaking [55], NPS [13], and time-domain EOS [17, 94], temporal field reconstruction with incredibly high attosecond temporal resolution became feasible. However, these techniques essentially neglect the dependence of the electric field on spatial coordinates, and each point of the measured discrete field in time represents an averaged intensity in the cross-section of the pulse. Therefore, possible spatio-temporal distortions, which can significantly increase the pulse duration and decrease the peak amplitude, are veiled from an observer [141, 142]. The presence of such distortions is especially crucial in measurements related to ultrafast and attosecond physics.

In this matter, EOI gives absolute spatio-temporal information about the electric field and is easy to implement in free space without a vacuum environment. All spatio-temporal couplings can be revealed without the need for complex data processing and algorithms. A comparison with theory becomes more reliable, reducing the number of assumptions and parameters about the spatial effects. With a simple Fourier transform, a time-dependent waveform at each pixel can be converted to amplitude and phase of each frequency of the broadband light, making EOI suitable for hyperspectral imaging.

In addition, light pulses with a complex spatial structure are of great interest and have many applications in modern science. Waveforms with the non-diffracting Bessel spatial distribution exhibit several intriguing features, like self-reconstruction [143] or formation of optical pulling forces [144]. Another interesting example is optical vortices, which carry orbital angular momentum and have been applied in many research fields, such as optical information transmission [145] or optical micro-manipulation [146]. Reliable retrieval of electric fields with complex spatial shape is incredibly difficult and cannot be realized with basic characterization techniques. EOI can pave a straightforward way for the complete spatio-temporal characterization of these beams, providing a time-dependent wave for each pixel in the plane of the EOS crystal.

In this chapter, for the first time, the EOI technique is applied in the near-infrared range to fully resolve the electric field of the 14 fs NIR pulse (120-200 THz) both in time and space. The completion of a three-dimensional pulse reconstruction is shown to be straightforward, revealing spatio-temporal distortions as well as the wavefront properties. In addition to the near-infrared spectral region, all benefits of the EOI are transferred further to the visible optical range (up to 450 THz). Synthesized NIR-visible waveforms are fully characterized, exposing coherent spatio-temporal composition of the involved channels and other intriguing optical effects.

3.1 Broadband Near-Infrared Waveforms

First, the laser pulses after the OPCPA are reconstructed using the well-established EOS method. The analysis of the retrieved waveform enables the pulse compression using an AOPDF feedback loop. Once a nearly transform-limited duration is reached, the imaging technique is employed for absolute space-time field characterization.

3.1.1 Temporal Field Reconstruction

The time-domain pulse retrieval in the present thesis is partially reproduced from the EOS experiments that have recently been done with the previous three-stage OPCPA configuration [17]. After the OPCPA modernization during this work, the question about the output pulse shape and its compression has arisen again.

An important requirement for high-frequency EOS is a large bandwidth of the probe pulse in order to successfully resolve frequencies up to 200 THz. The spectral bandwidth of light after the process of broadening in the HCF is more than enough for the goals that we pursue. However, the bandwidth of the probe is not the only condition for performing EOS measurements: a poorly compressed probe leads to covering more than a half cycle of the test field, which can result in wrong polarization rotation of adjacent spectral components and negligibly small EOS signal. Therefore, a nearly transform-limited probe pulse ($\sim$ 5 fs) is achieved by fine tuning a pair of glass wedges and generating second harmonic in a type-I BBO crystal. FROG reconstruction of the probe pulse can be found in [17].

The second stage of the OPCPA delivers about 1 mJ pulse energy. To avoid potential damage and saturation of the EOS crystal, we utilize only the first stage of the OPCPA with 40 µJ pulse energy, attenuated using a reflective neutral density filter with 4.0 optical density ($\sim$ 0.1 % of transmission at 2 µm). The light attenuation allows us to work on the edge of BBO saturation, providing maximum SFG for better SNR of the EOS system. The octave-spanning NIR field enters the type-II BBO crystal on the extraordinary axis collinearly with the visible probe, which passes through the crystal on the ordinary axis. Their nonlinear interaction generates photons of SFG radiation $\omega_{SFG} = \omega_t + \omega_p$ on the extraordinary axis. Bandpass-filtered light (500-550 nm), which contains the local oscillator and SFG components, experiences polarization rotation depending on the strength and direction of the NIR electric field. A Wollaston prism projects this light onto crossed
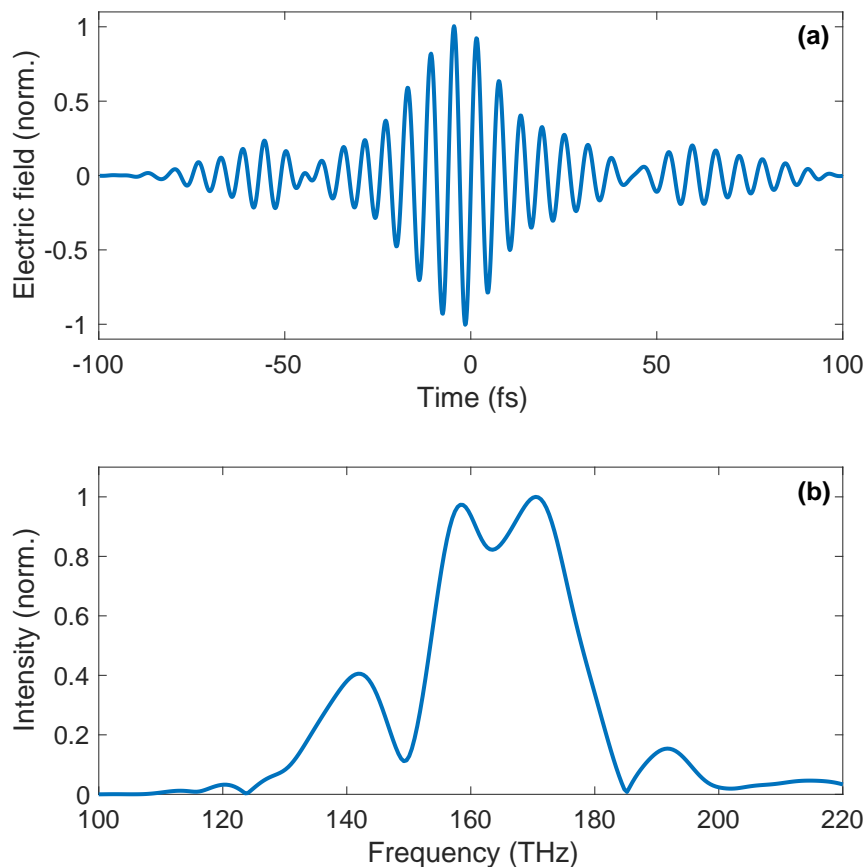
Figure 3.1: Time-domain electro-optic sampling of the 1.9 µm OPCPA pulse: **(a)** Temporal evolution of the NIR electric field with 18 fs time duration. **(b)** Corresponding spectrum obtained by the Fourier transform of (a).

axes at the 45° angle and splits the wave packet into two orthogonally-polarized arms for detection with balanced photodiodes. In the standard EOS configuration, a quarter-wave plate can be placed before the Wollaston prism at the 0° angle to modify the beam ellipticity, which leads to the transformation of the LO and SFG to the right- and left-circular polarizations or vice versa. As a consequence, a $\phi_{\mathrm{CEP}} = \pi/2$ phase shift with respect to the actual electric field is imparted. With the direct projection by a rotated Wollaston, the CEP shift is not introduced.

The retrieved information about the 1.9 µm test field is sent to the AOPDF to correct for the dispersion (in addition to the Sapphire window) that the pulse gains along the path through the OPCPA crystals and other necessary optics. It is especially important to precisely compensate higher orders of dispersion and acquire a flat phase. After a few iterations with the AOPDF feedback loop, a nearly Fourier-transform-limited pulse of 14 fs can be obtained [17]. A typical EOS measurement and the Fourier-transform counterpart of the NIR field, focused by a biconvex BaF_2 lens (GVD ≈ 0.82 fs^2/mm at 1.9 µm) with

FL=100 mm, are depicted in Fig. 3.1. The extracted electric field is averaged over 450 laser shots per data point. Calculation of the full width at half maximum (FWHM) of the intensity profile, derived from Fig. 3.1a, yields about 18 fs pulse duration. In theory, the chirp can be present due to several reasons including higher-order dispersion, chromatic aberration of the broadband incident beam, etc. The pulse spreading and inability to compress the pulses to the Fourier limit (12 fs) can also take place due to various spatio-temporal couplings, which can be observed with the EOI technique as well as the actual field dependence on the spatial coordinates.

3.1.2 Spatiotemporal Field Reconstruction

To perform electro-optic imaging and spatially characterize the pulses under investigation, a mirror can be simply flipped after the EOS crystal to redirect the band-pass filtered light to the imaging system. It has to be noted that no additional beam path manipulation is required before the EOS crystal, allowing for the direct comparison between EOS and EOI. In standard EOS, the spatial information about the interaction is already captured by the band-pass filtered light, but it is spatially integrated by the photodiodes. Therefore, a standard imaging unit, utilizing a microscope objective and a camera, can straightforwardly visualize this valuable information. In theory, it is possible to realize both techniques, EOS and EOI, working simultaneously by placing a beam splitter right after the EOS crystal. In the current section, a 4x objective lens with NA=0.1 is employed along with a pair of tube lenses and a CCD camera for imaging measurements. A full description of the experimental setup can be found in Section 2.2.

The operational principle of EOI is adapted from EOS — a time delay between the white-light probe $E_p(\omega_p)$ and the test $E_t(\omega_t)$ pulses is varied to measure changing SFG, generated in the EOS crystal, and extract the electric field of the test pulse. SFG components, $E_{SFG} \propto C_{NL} E_p(\omega_p) E_t(\omega_t)$, and the local oscillator $E_p(\omega_p)$, which is the part of the probe spectrum, interfere on the CCD after their projection by a WGP, creating two images with perpendicular electric field orientations, where C_{NL} is a constant factor determined by the nonlinear crystal. The two a and b images appearing in the CCD are

$$a \propto |E_p + E_{SFG}|^2 \propto E_p^2 + 2C_{NL}E_p^2 E_t + C_{NL}^2 E_p^2 E_t^2, \tag{3.1}$$

$$b \propto |E_p - E_{SFG}|^2 \propto E_p^2 - 2C_{NL}E_p^2 E_t + C_{NL}^2 E_p^2 E_t^2, \tag{3.2}$$

where E_p, E_t and E_{SFG} represent complex spectral amplitudes. The a and b images in the current state are only the intensity distributions. The electric field image of the test waveform E_t can be obtained through subtraction of the amplitudes of the recorded images, with the removal of the spatial effects of the probe beam through normalization

$$E_t \propto \frac{\sqrt{a} - \sqrt{b}}{\sqrt{a} + \sqrt{b}}. \tag{3.3}$$

In this case, the signal on the detector scales linearly with the intensity of the probe light, but the retrieved field is independent of that intensity. However, spatial variation of the probe and test intensities across the detection plane is expected to affect the SNR, which will also vary spatially. As was described in Section 2.3, two additional approaches are realized to significantly improve the SNR of the imaging system: 1) placing the TFP after the band-pass filter and 2) capturing cross-polarized images for both $\phi_{\mathrm{CEP}} = 0$ and $\phi_{\mathrm{CEP}} = \pi$. The resulting difference image of the test electric field E_t is calculated as

$$E_t \propto \frac{\sqrt{a_0} - \sqrt{b_0}}{\sqrt{a_0} + \sqrt{b_0}} - \frac{\sqrt{a_\pi} - \sqrt{b_\pi}}{\sqrt{a_\pi} + \sqrt{b_\pi}}, \tag{3.4}$$

where a_0 and b_0 are images with $\phi_{\mathrm{CEP}} = 0$; a_π and b_π with $\phi_{\mathrm{CEP}} = \pi$.

In Figure 3.2, an EOI measurement of the NIR field is demonstrated, with an aperture of 4 mm diameter placed in the beam path ~ 1 m before the focusing element. In the first row of the figure, three spatially resolved two-dimensional snapshots of the electric field in the BBO plane are depicted, at a time delay of -3.34 fs with the positive extremum of the field amplitude (Fig. 3.2a), -1.67 fs, when the electric field crosses zero value (Fig. 3.2b) and 0 fs with the negative extremum (Fig. 3.2c). It is particularly clear that the field has a complex structure with out-of-phase rings around the central maximum indicating the presence of some types of aberration. Fig. 3.2d visualizes the spatiotemporal dynamics of the NIR optical pulse over the time delay window along y axis, while the x value is fixed to zero. This perspective especially underlines spatio-temporal properties of the wavefront. The aperture placed in the NIR path to control the incident power, as further discussed, directly affects wavefront curvature and other related distortions caused by spherical aberration. Fig. 3.2d explicitly demonstrates that the wavefront is slightly curved, signifying that the detection crystal is not placed exactly at the focal plane. In Fig. 3.2e, the three-dimensional (3D) electric field is shown, providing an opportunity to follow the spatio-temporal evolution of the 1.9 µm field in all coordinates. As 3D structures are difficult to visualize in a 2D medium, surface representation is implemented in the current work: semitransparent contour denotes 12 % of the maximum value of the amplitude and opaque contour is 60 %. The strongest part of the pulse, nearly two cycles, can be clearly seen in the picture. The direct comparison with the time-domain EOS (Fig. 3.1) can be done to reveal how different spatial sections contribute to the effective pulse duration.

The cube of the waveforms at each pixel can be exploited to create a hyperspectral image of the test field. For this purpose, time-domain waveforms are transformed into the frequency domain, obtaining the amplitude and phase of each spectral component. A false-color image of the NIR beam focused by the BaF_2 lens is depicted in Fig. 3.3a. Red, green and blue colors correspond to the narrowband regions around 145 THz, 168 THz and 189 THz, respectively, with a channel bandwidth of 8 THz (see also Fig. 3.3e-g). Note that the intensities of the channels are numerically adjusted in the image for better visualization. The colors can be easily remapped to highlight any spectral range. From the image, the color spreading across the beam can be seen, with the green tones on the left-hand side and the red tone on the right-hand side. However, the central part of the
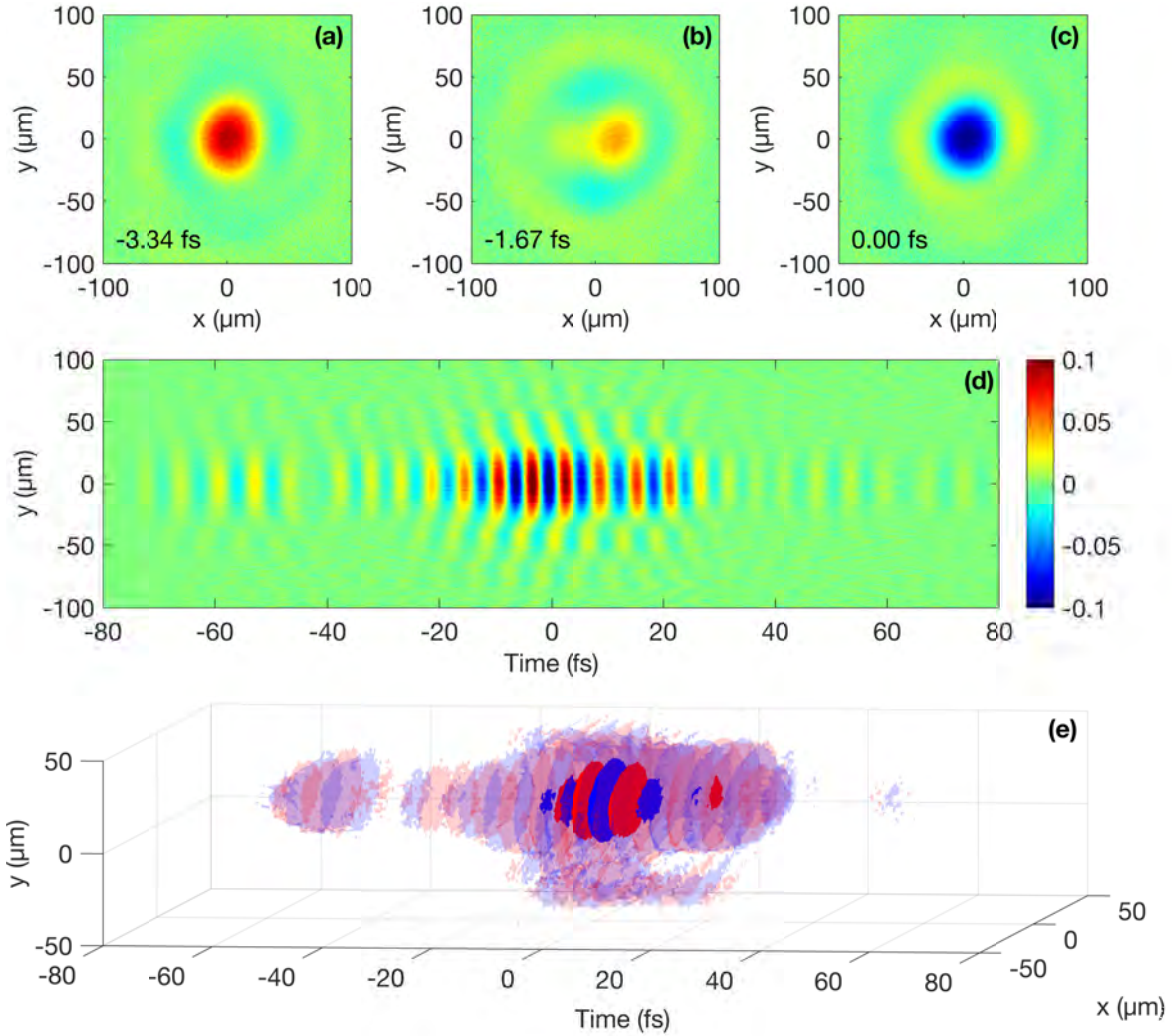
Figure 3.2: Absolute spatio-temporal characterization of the 1.9 µm OPCPA pulse with electro-optic imaging. Electric field at the time of **(a)** highest field strength, **(b)** zero crossing and **(c)** negative maximum. **(d)** Spatio-temporal electric field distribution in the plane $E(x = 0, y, t)$. **(e)** 3D image of the electric field, where semitransparent and opaque contours represent 12% and 60% of the maximum, respectively.

image seems to be whitish, implying that all the incident colors are present in the area. The spatio-temporal distortion that assumes a spatial separation of different frequency components within the beam cross-section is usually referred to as spatial chirp. Studies of spatio-temporal distortions acquired by the amplified pulse in noncollinear OPCPA due to pulse front mismatch have demonstrated the possibility of the spatial chirp formation in the amplification process [147–149]. The hyperspectral image clearly illustrates the presence of a similar effect in the imaged focus.

The temporal and spectral properties of the beam are explored in more detail by analyzing three individual pixels. The time-domain waveforms at the left edge ($x = -20$ µm, $y = 0$), center ($x = 0, y = 0$), right edge ($x = 20$ µm, $y = 0$) of the beam are demonstrated in Fig. 3.3b-d, along with the Fourier-transform of these waves (Fig. 3.3e-g). The shaded areas (red, green and blue) in Fig. 3.3e-g are drawn to show the color designation in Fig. 3.3a. The brightest central pixel ($x = 0, y = 0$) contains the information about the major part of the incident frequencies, with an approximate pulse duration of 15.8 fs. The analysis of the pixel on the left-hand side ($x = -20$ µm, $y = 0$) indicates that the spectrum is flatter in the green zone and mainly the same in the other ones. This leads to a slightly shorter time duration of 15.2 fs in this area. The pixel on the right-hand side ($x = 20$ µm, $y = 0$) tends to contain more low-frequency components rather than high-frequency ones. Thus, the local bandwidth is relatively decreased, and the spectrum is red-shifted with significant intensity reduction in the green zone, resulting in a relatively long time duration of 28.7 fs. Such inconsistency in the frequency distribution in the cross-section of the beam can be a reason why Fourier-transform-limited pulses are difficult to achieve in the standard OPCPA schemes in general.

As discussed earlier, EOI provides full information about the wavefront of a test beam in the plane, where the EOS crystal is placed, making the technique an alternative to a wavefront sensor. In the measurement mentioned above, a biconvex lens was utilized to focus the collimated 1.9 µm beam, expecting the introduction of spherical aberrations in the imaged focus. For this reason, a couple of additional experiments are done to track the changes of the wavefront of the NIR beam after passing through different diameters of the lens clear aperture.

The electric field image, captured with the aperture size of 2 mm, is depicted in Fig. 3.4 along with the case of free beam propagation. The detection crystal was fixed during all three measurements (including the original) and slighly saturated in the additional measurements. A crystal saturation is one of the adverse effects that should be carefully inspected and avoided. Due to spherical aberration, the beam with a low NA is focused further from the lens. In this case, the NIR beam at the detection plane converges and the wavefront curvature is convex (Fig. 3.4a). In the original measurement with the aperture size of 4 mm (Fig. 3.2d), the wavefront is relatively flat. When the beam freely propagates and has a high NA, the beam focuses closer to the lens. Therefore, the wavefront in the crystal plane becomes strongly concave, making the recorded field to be deeply diverging (Fig. 3.4b). The wavefront sensing feature of EOI provides complete information about the wavefront structure of a beam under study, which can be applied to study innovative optical elements for correcting spherical aberrations.
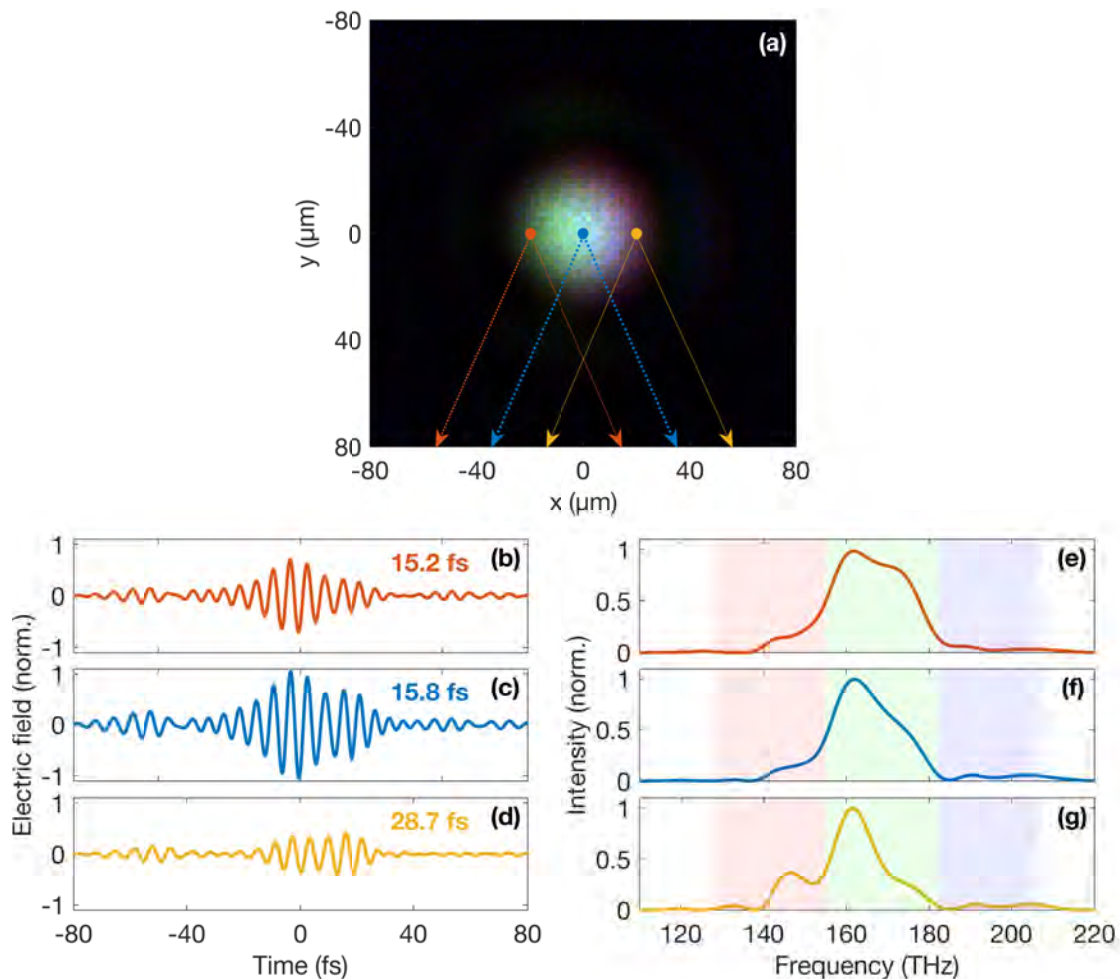
Figure 3.3: Fourier analysis of the NIR OPCPA field. **(a)** False-color image of the beam, where red, green, and blue intensities are mapped to 145 THz, 168 THz, and 189 THz. **(b)-(d)** Temporal waveforms at the left edge ($x = -20$ µm, $y = 0$), center ($x = 0, y = 0$) and right edge ($x = 20$ µm, $y = 0$) of the beam, normalized to the peak amplitude of (c). **(e)-(g)** Corresponding normalized spectra obtained by the Fourier transform of (b)-(d).

Interestingly, a single EOI measurement allows us to calculate, how far the focus is from the imaged plane, and fully determine the field form in any other plane along the propagation direction. At the moment, this is outside of our interest. This procedure will be discussed in detail in Chapter 4, where interesting spatio-temporal dynamics behind strong chromatic aberration of a focused pulse is studied.

In conclusion of the current section, it is worth emphasizing the practical purpose of the TFP and telescope in the imaging system. The very first attempt to perform EOI was under the simplified EOS conditions when the test and probe beams are focused by a single off-axis parabolic mirror into the EOS crystal. This optical arrangement leads to beam spots with similar spatial dimensions in the focal plane, even if an aperture placed in the
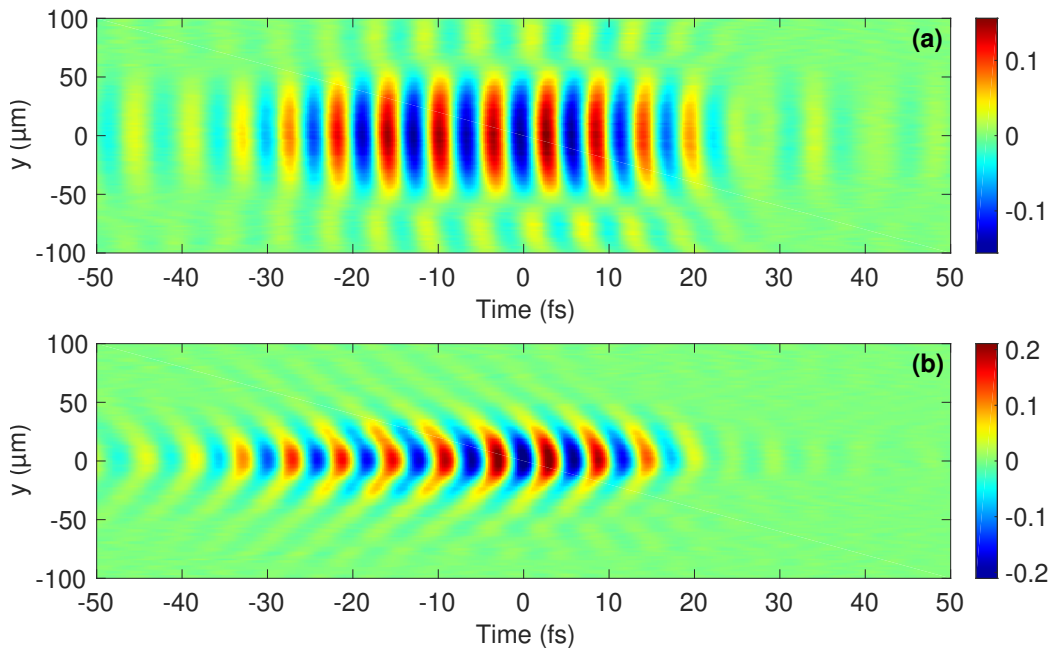
Figure 3.4: Comparison of wavefront patterns imaged in a single detection plane with and without an aperture. Electric field of the 1.9 µm beam in the case of **(a)** passing through 2 mm aperture and **(b)** free propagation.

probe path is maximally closed. At the same time, the aperture must be placed relatively far from the detection crystal to provide a flat wavefront of the probe pulse in the imaging plane. An example of such measurement is depicted in Fig. 3.5a-c. It can be easily noticed that the NIR field is substantially truncated because the sampling beam does not still have sufficiently large cross-section to interact with the NIR electric field (see also [100]). Such images give only an idea about the internal spatial structure of the NIR pulse but not the complete field information. In this matter, boundary spatial regions of the electric field often provide valuable knowledge about different types of aberrations. In addition, spatial overlap between the NIR and sampling beams can be misaligned, which might lead to misinterpretation of the obtained results. The main advantage of this geometry is a decent SNR without implementing additional tricks, as each pixel generates strong enough SFG signal in the EOS crystal.

One of the approaches to avoid the truncation might be an aperture placed in the unfocused probe beam close to the WGP. In this case, the probe pulse after passing through the hole generates less SFG. In addition, the aperture creates a diffraction pattern, leading to an inhomogeneous probe intensity distribution and distorting the probe wavefront. In our opinion, the best solution is to produce a larger probe focal spot using a telescope. Nevertheless, the low nonlinear coefficient of BBO along with the spatial variation of the probe and NIR beams leads to poor SNR in the marginal zones of the field cross-section. The noise level is greatly enhanced in these regions due to weak NIR intensities and, as a
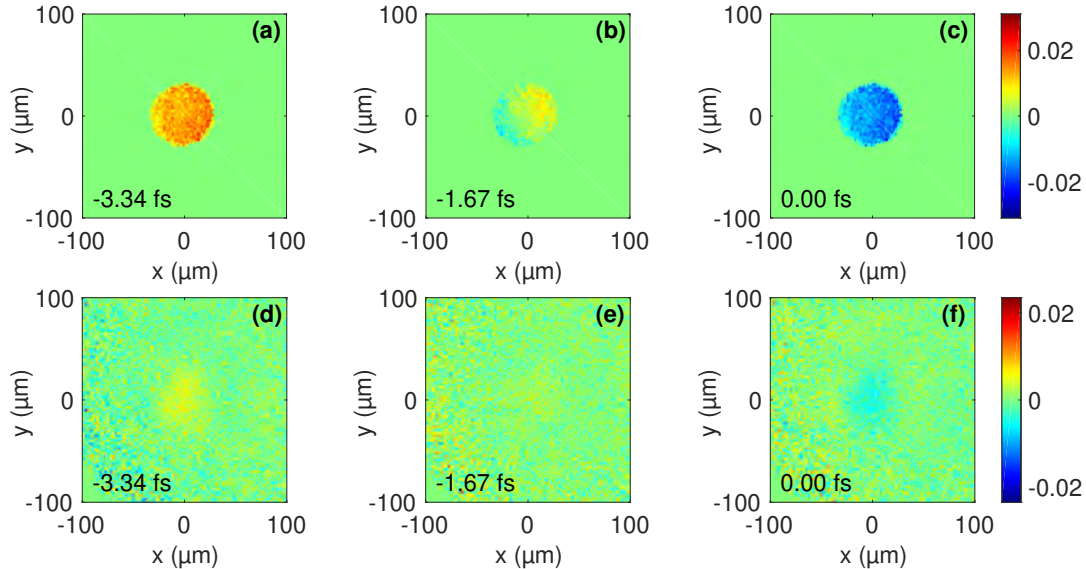
Figure 3.5: Influence of the telescope and TFP on extracted electric field images. **(a)**-**(c)** The NIR pulse retrieved without the TFP and telescope at the time of highest field strength, zero crossing and negative maximum. **(d)**-**(f)** The NIR pulse extracted without the TFP at the time of positive extremum, zero crossing and negative extremum.

result, low upconversion there, affecting the NIR field signal across the image (Fig. 3.5d-f). In principle, proper data processing can lead to acceptable field images by sacrificing spatial resolution. However, as described in Subsection 2.2.1, the problem can be solved by a new technique, combining the TFP and the band-pass filter. This approach enables careful tuning of the LO amplitude, significantly increasing the contrast of the extracted images (see original Fig. 3.2). The comparison of all three measurements was made under similar experimental conditions and numerical parameters.

3.2 Ultra-Broadband Synthesized Waveforms

A particular important property of the OPCPA pulses is that they can be spectrally broadened to an extreme degree in an ambient-air-filled HCF, with the output spectral range from UV to NIR. Implementing this, we subsequently divide the emerged continuum into three channels - 1) 300-600 nm (CH0), 2) 700-1400 nm (CH1) and 3) 1400-2700 nm (CH2) [94]. An individual compression of each channel and their coherent recombination can lead to a sub-cycle transient with ~ 1.5 fs pulse duration, beating the fundamental limit of a single-cycle electric field. However, in the EOS work [94] and current thesis, the higher-frequency UV-VIS channel is used as a sampling pulse to characterize sub-cycle synthesized transients, comprising VIS-NIR and deep NIR channels, with tunable carrier-envelope phase and pulse duration. EOI likewise advances the spectral limits, providing absolute space-time field characterization of ultra-broadband synthesized waves.

The actual setup slightly differs from the work done in [94]. The optical scheme has been partially rebuilt (see Enrico Ridente's Ph.D. thesis in future), introducing great stability, reliability and reproducibility of the output beams. Under such conditions, the EOS methodology opens a door towards attosecond science with incredible temporal precision in a free-space environment, without implementing a huge and expensive vacuum apparatus. In this section, the resolving power of ultra-broadband EOS is brought to the space domain, where spatial resolution is determined by the UV spectral components.

3.2.1 Characterization of Individual Channels

The light synthesis procedure requires maximally short pulses in the individual channels. The AOPDF is unable to correct the higher-order spectral phase of the light after HCF, because the settings of the device are configured to maximize the efficiency of the broadening process. Nevertheless, CEP control of the broadened light is still available using the AOPDF, which is extremely useful in both EOS and EOI experiments.

The compression of the channels is reached by manufacturing special multilayer mirrors, separately for each arm [150]. As the UV light suffers from extreme dispersion in any transparent material, no transmissive optics are used in the CH0 path, except for a pair of MgF_2 wedges. Carefully tuning the wedges and maximizing the generation of second harmonic in a type-I BBO crystal, a nearly transform-limited pulse can be attained. After compression, the pulse of the probe UV-VIS arm is retrieved using XFROG and measured to be 2 fs, enabling the detection of half-cycles durations of ~ 1 fs in EOS experiments [18, 94].

Time-domain EOS field retrieval with CH0 as a sampling pulse is applied first to confirm that the maximum compression of CH1 and CH2 is achieved. As all the arms have the same polarization and enter the BBO on the ordinary axis, SFG is generated on the extraordinary axis due to the type-I phase matching. More details about the materials and methods used in the measurements can be found in [18].

A typical time evolution of the channels is depicted in Fig. 3.6a, normalized to the peak value of CH1. The retrieved waveforms have ~ 6.8 fs and ~ 12.5 fs pulse duration at FWHM for CH1 and CH2, respectively. Adjusting the delay stages, it is possible to combine the electric fields at any relative time and synthesize pulses with completely different shapes. The shortest synthesized transients can be obtained when the peak amplitude of CH1 is coherently overlapped with the peak amplitude of CH2, as demonstrated in Fig. 3.6a. The resulting pulse will be shown and discussed in the next subsection. Corresponding spectra obtained by the Fourier transform of the fields are illustrated in Fig. 3.6b, normalized to the peak amplitude of CH1. The new resolving capabilities of the EOS technique can be clearly noticed, with spectral limits reaching optical frequencies up to 450 THz (670 nm). Once the time-domain EOS has paved the way to the new spectral region, a transfer of the imaging apparatus to the same frequency range should not face difficulties.

The experimental setup is built in such a way that EOI can be performed after EOS with a short time interval to minimize the influence of temporal drifts and directly compare two approaches. The guiding of the band-pass filtered UV beam to the imaging unit is done by flipping a mirror after the EOS crystal.
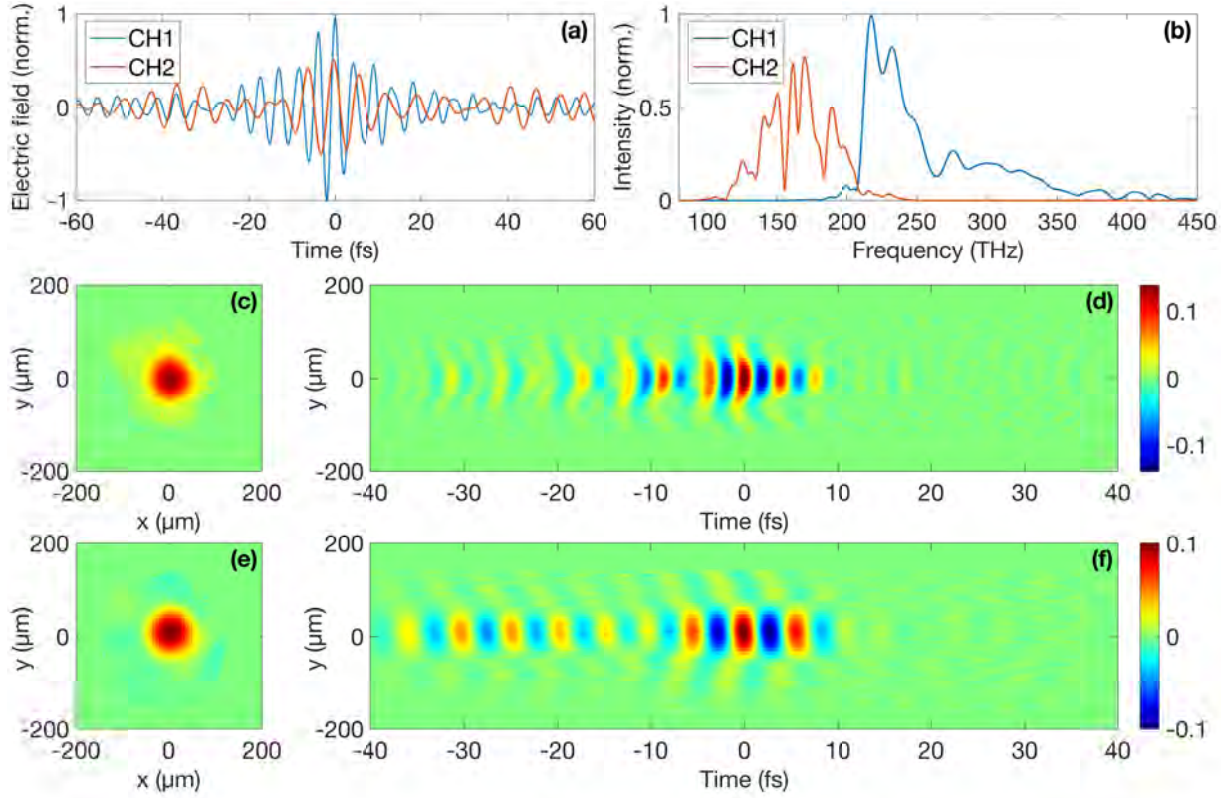
Figure 3.6: Complete spatio-temporal reconstruction of CH1 and CH2 of the synthesizer. **(a)** Waveforms obtained via standard EOS. **(b)** Corresponding spectra derived by the Fourier transform of (a). Electric field of CH1 **(c)** at the positive extremum and **(d)** along the y-axis. Electric field of CH2 **(e)** at the positive extremum and **(f)** along the y-axis.

As described in Section 2.2, the synthesis imaging system consists of a UV lens with FL=200 mm and a pair of UV tube lenses with FL=175 mm. The resulting magnification of the system is ~ 0.9, which is sufficient to resolve the inner spatial structure of pulses with a relatively large beam waist. Besides, an aperture is embedded within each arm to control the beam size in the focus as well as the transmitted power.

The physics behind the experiment mainly replicates EOI with the OPCPA field. The spatial distribution of CH1's electric field at the positive extremum is shown in Fig. 3.6c. The spatio-temporal dynamics of the pulse along the y-axis is depicted in Fig. 3.6d, exposing the positive wavefront curvature at the BBO position. The electric field of CH2 in the $x-y$ cross-section and $y-t$ plane is shown in Fig. 3.6e and Fig. 3.6f, respectively. Interestingly, the spatio-temporal dynamics of CH2 exhibits a flatter wavefront and the signs of pulse-front tilt in the detection plane. The pulse-front tilt is potentially expressed in the image as a small rotation of the wavefront around the x-axis. The hyperspectral analysis of both channels has not shown any noticeable spectral deviations in the cross-section, like the spatial chirp, which was present in the original driving beam before the HCF. We believe that the spatial chirp is eliminated by the fiber acting as a spatial filter.
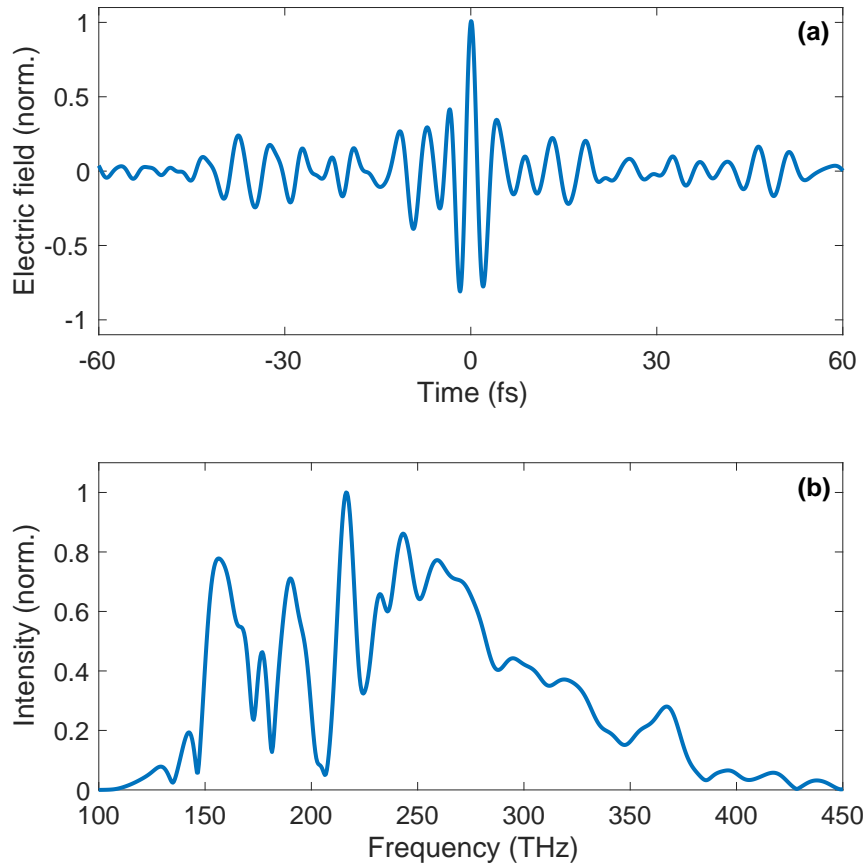
Figure 3.7: Time-domain electro-optic sampling of a synthesized pulse. **(a)** Temporal evolution of the transient with 4.5 fs time duration; **(b)** Corresponding spectrum obtained by Fourier transform of (a).

3.2.2 Synthesized Transient

In the current subsection, an example of the synthesized transients will be demonstrated. Undoubtedly, the main interest is concentrated on the shortest synthesized pulses, which will be analyzed and spatiotemporally visualized. As described earlier, such short oscillating electric fields can be generated by a proper coherent combination of the individual components, which have been presented in the previous subsection. This is feasible with sufficient interferometric stability and precise control over the delay between the two arms.

The electric field evolution of one of the shortest sub-cycle synthesized pulses, achieved in the experiment, is shown in Fig. 3.7a. The field is retrieved using the time-domain EOS, with a measured pulse duration of 4.5 fs. The interference between the two channels leads to single-peak light confinement, which is in great demand in ultrafast science [151]. The spectral intensity in Fig. 3.7b, obtained by the Fourier transform of the electric field, illustrates the multi-octave bandwidth of the synthesized waveform, which consists of two independent spectral regions with frequencies of 120-200 THz and 210-450 THz.

Experiments with a waveform synthesizer are not new in the community as many scientific groups have developed similar laser sources, sometimes with even shorter pulse durations [151–154]. However, the characterization of synthesized transients using the EOS metrology is indeed an exciting achievement, especially taking into account a potential extension of the time-domain field reconstruction to an imaging geometry and thereby the spatial domain. Thus, the EOI modality has the capacity to make synthesized pulses the most characterized ever, providing absolute spatio-temporal field information in a compact, simple setup in ambient conditions.

The band-pass filtered light with the 290-350 nm spectral region, which contains LO components of the UV-VIS channel and SFG components, generated by the same channel and the synthesized field in the BBO, is redirected to the 4f UV imaging system for EOI measurements. The interference on the CCD camera and subtraction of the crossed-polarized images yield the electric field images as a function of the time delay. It is worth noting that the BBO is placed in the relative focus of both CH1 and CH2.

Three individual field frames for 0 fs, 0.8 fs, and 1.6 fs are depicted in Fig. 3.8a-c, respectively. The electric field image at 0 fs shows the spatial distribution at the dominant field strength and appears to be relatively round, without any obvious distortions. The field images with zero crossing and negative extremum complement the previous image and provide an opportunity to look inside the pulse's structure.

The image of the field dynamics in the plane $E(x = 0, y, t)$, shown in Fig. 3.8d, reveals interesting properties of the wavefront at the imaged position. Since the BBO is placed in the mean focal plane of both channels, which have a small difference in the focus position, the image discloses a different spatio-temporal behavior of the two components. According to the investigation of the individual arms in the previous subsection, the NIR channel (CH2) has the focal plane slightly further from the focusing element than the VIS-NIR channel (CH1). Thus, the physical shift of the EOS crystal towards the focusing element makes the detected CH2's wavefront negative, i.e. the beam is converging. It is clearly seen in the image that the right-hand side oscillations with respect to the major peak represent the negatively curved lower frequencies. At the same time, the CH1's wavefront is still positive and the beam is diverging (positively curved higher frequencies on the left-hand side). However, at the peak position of the electric field, the individual channels start to compensate each other, allowing the shaped wavefront to be relatively flat. In this particular context, EOI provides new, deeper insight into the process of the formation of synthesized fields. The 3D electric field visualization in Fig. 3.8e emphasizes the spatiotemporal sub-cycle structure of the synthesized pulse.

Interesting spatio-spectral effects can be also extracted by performing the Fourier transform of every single waveform of each pixel. This operation yields a hyperspectral image of the pulse, which provides the position of each frequency component in the cross-section. The false-color image is presented in Fig. 3.9a, where red, green and blue colors correspond to the spectral regions around 190 THz, 285 THz and 380 THz, respectively, with the channel bandwidth of 30 THz (see also Fig. 3.9e-g). The image reveals the spatial misalignment of the CH1 and CH2: the right-hand side of the synthesized beam tends to contain more low-frequency components rather than the high-frequency ones. This effect
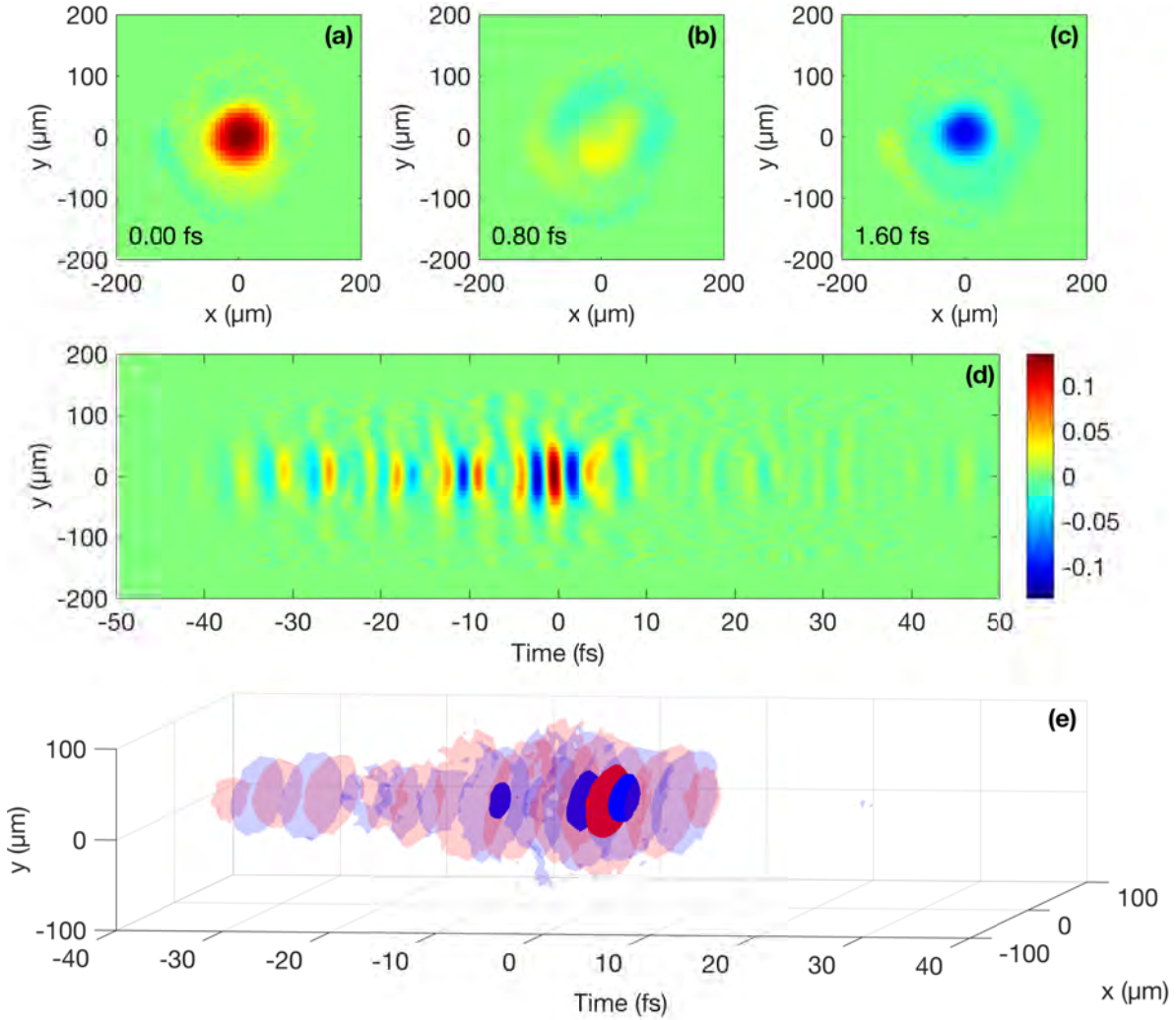
Figure 3.8: Absolute spatio-temporal characterization of a synthesized pulse with visible-near-infrared spectrum. Electric field at the time of **(a)** highest field strength, **(b)** zero crossing and **(c)** negative maximum. **(d)** Spatio-temporal electric field distribution in the plane $E(x = 0, y, t)$. **(e)** 3D image of the electric field, where semitransparent and opaque contours represent 12% and 60% of the maximum, respectively.
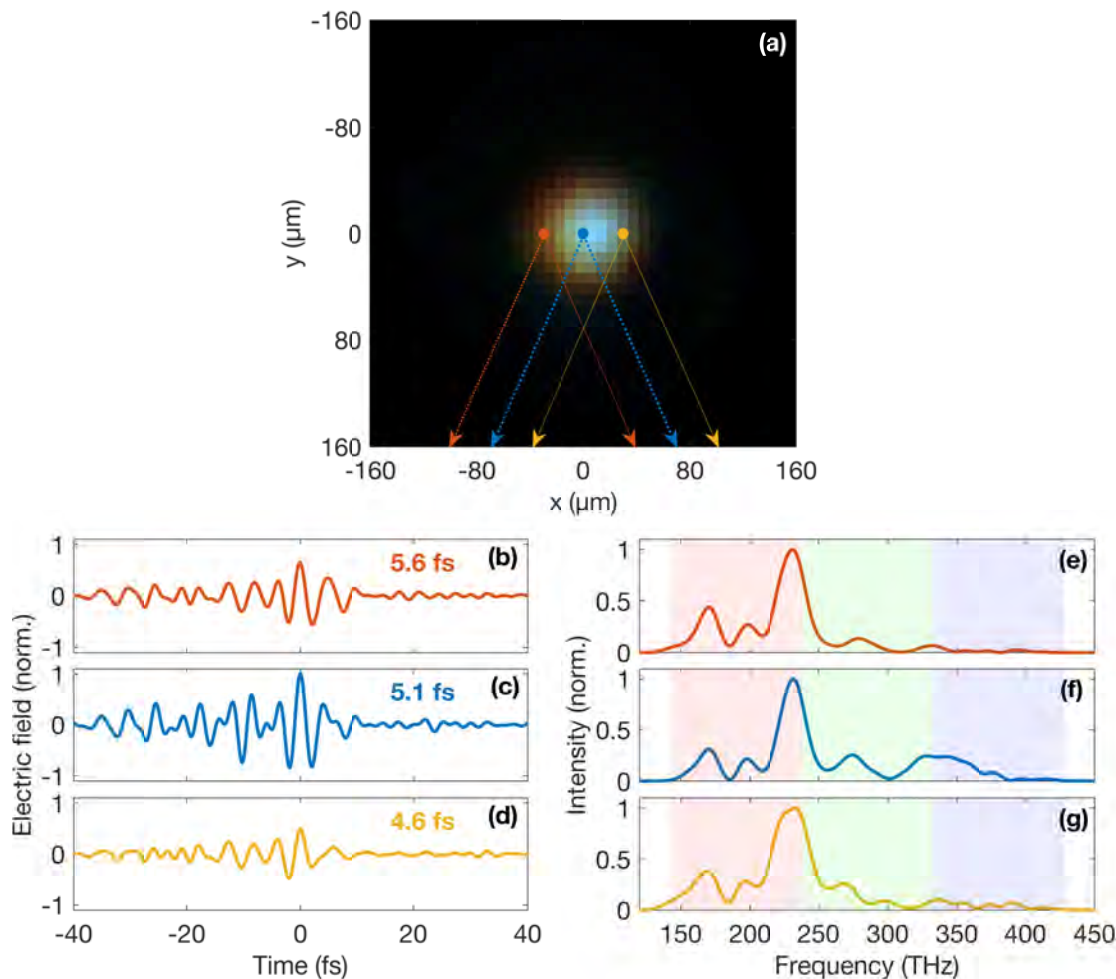
Figure 3.9: Fourier analysis of the synthesized pulse. **(a)** False-color image of the beam, where red, green, and blue are mapped to 190 THz, 285 THz, and 380 THz. **(b)-(d)** Time-domain waveforms at the left edge ($x = -30$ µm, $y = 0$), center ($x = 0, y = 0$) and right edge ($x = 30$ µm, $y = 0$) of the beam. **(e)-(g)** Corresponding spectra obtained by Fourier transform of the temporal waves.

may be an indication of unequal beam waists or different focus positions on the propagation axis. In any case, this leads to the reduction of local bandwidth and, consequently, longer pulse durations in such areas.

In addition, three waveforms from the false-color image are analyzed in more detail — at a pixel at the left edge ($x = -30$ µm, $y = 0$), center ($x = 0, y = 0$), and right edge ($x = 30$ µm, $y = 0$) of the beam. Corresponding time-varying oscillations and their Fourier transform are presented in Fig. 3.9b-d and Fig. 3.9e-g, respectively. The pulse duration of the central pixel at the peak intensity is measured to be 5.1 fs, while the calculated spectrum spans almost the entire incident bandwidth. The pixel on the left side of the beam ($x = -30$ µm, $y = 0$) contains significantly reduced local bandwidth, missing the

high-frequency part. This leads to a pulse duration of the waveform at this pixel to be 5.6 fs. The right part of the beam ($x = 30$ µm, $y = 0$), which includes most of the incident optical components, has a pulse duration of 4.6 fs. The detailed analysis showed the existence of a few pixels that experience pulse durations of $\sim 4 - 4.5$ fs.

3.3   Outlook

This chapter has shown the field-resolved imaging capabilities in the high-frequency regime. Absolute spatio-temporal characterization of the NIR light fields including CEP is available through a compact and simple imaging setup built in ambient conditions. In the present work, the technique has also been extended to cover visible frequencies in the light synthesis experiment, opening the door to new studies in the NIR-VIS frequency range.

The experimental concept of EOI has been directly transferred from EOS, which allows the interaction of two light waves to be used to record the information of one of the fields into the polarization state of another. In the imaging concept, each point of the cross-section of a test field leads to an individual polarization rotation, appearing as a pixel in a CCD image. The inner spatial structure of the NIR-VIS waveforms in the far-field can be retrieved with pretty high spatial resolution, provided by the diffraction limit of the LO. In many spatio-temporal imaging approaches, high temporal resolution makes achieving high spatial resolution difficult — large bandwidth of an ultrashort pulse results in the occurrence of chromatic aberration of the imaging system. The method presented here lacks this disadvantage because a test broadband field is compressed to a very narrowband light through the conversion process in a $\chi^{(2)}$ crystal. Sub-cycle temporal (~ 1 fs) and high spatial resolution (~ 3.5 µm) are provided simultaneously in a free-space optical scheme. Deeper insight into the subwavelength spatial resolution will be presented in Chapter 5.

EOI provides complete three-dimensional information about a light field without any assumptions on the dependence on spatial dimensions. The metrology level of the technique makes sub- or few-cycle fields to be the most characterized pulses ever. This implies that everything, including CEP distortions and other spatio-temporal couplings, can be extracted, analyzed and visualized.

In this matter, spherical aberrations produced by the focusing lens and the pulse-front tilt of CH2 have been successfully demonstrated. The Fourier transform of the cube of acquired waveforms can be utilized to produce a hyperspectral image to monitor how different spectral components are relatively positioned in the cross-section of the beam. In particular, the spatial chirp of the 1.9 µm OPCPA laser source has been revealed, where the low frequencies are spatially separated from the high frequencies. With an EOI measurement, it is possible to observe how a pulse duration, obtained with various time-resolved techniques, in reality, can be spatially separated and formed as an effective duration by the superposition of different waves in each spot of the cross-section. Thus, this imaging method can be used for spatio-temporal correction of the amplified pulses, especially when high-precision measurements are involved. The study of dynamical processes in each OPCPA crystal would facilitate better conversion efficiencies and higher peak intensities.

Completely new knowledge about the process of light synthesis has been presented, exhibiting interesting features of the spatio-temporal interaction of the individual components (CH1 and CH2), which form the synthesized pulse. This insight would enable a pulse synthesis of maximally short Fourier-transform-limited waveforms with precise information about the contribution of each channel.

In addition, two novel techniques to significantly improve the contrast of the imaging system has been presented. The first approach relies on the direct control of the LO amplitude using a TFP. It has been clearly shown that a combination of the TFP with the band-pass filter makes field images surprisingly clean, with a high dynamic range. This can be also advantageous in traditional EOS, both in the high-frequency regime and the THz spectral region, where intense irradiation is hardly achievable. The second approach is based on measuring a waveform with opposite CEP. By recording two images with both CEP=0 and CEP=π, higher SNR of the system has been attained.

The detection frequency limit of the synthesis imaging setup can be extended to about 500 THz under the present experimental conditions. The imaging methodology is expected to be directly applied to the commonly used light sources as the Ti:Sapphire-based and erbium-doped fiber laser systems.

Chapter 4

Field Shaping by Metasurface Optics

The study of nanoscale structures and their interaction with incident light has established a new exciting research area called nanophotonics, which recently emerged in the scientific world. A flat material interface, consisting of subwavelength-spaced nano-scatters, provides incredible far-field control over the properties of light, enabling innovative optical phenomena, such as subwavelength focusing, negative refraction, or optical cloaking [155–157]. Metasurfaces yield a miniaturization of standard refractive optics into an extremely thin single-optic design, which permits shaping of arbitrary wavefronts. In order to focus the light into a nearly diffraction-limited spot, a standard glass lens requires complex optical techniques such as aspheric profile or multi-lens system. A meta-lens inherently circumvents refraction-induced spherical aberration and reduces other monochromatic aberrations such as astigmatism or coma [126].

However, the question about the temporal control over the electric fields using such meta-optics is still open. This task is directly connected to the ability to suppress chromatic aberration of a broadband incident pulse and maximize its peak intensity. Direct detection within this domain, even for complex-structured waveforms, can be readily reached by EOI, providing new knowledge about the focus capability of metasurface lenses in both time and space. This information would be very helpful to simplify and develop the next generation of flat optics and other nano-devices with absolute spatio-temporal control over the light properties in the far-field.

In this chapter, the EOI technique is applied to resolve and observe spatio-temporal evolution of the NIR electric fields generated by metasurface optics. The work is based on a collaboration with the Harvard John A. Paulson School of Engineering and Applied Sciences and particularly Prof. Capasso's scientific group, which has pioneered ultrathin metasurface optics, and provided samples to our lab. The first meta-structure is a lens with strong chromatic aberration, designed for single wavelength operation. It is perfectly suitable for the study of the spatio-temporal process of the chromatic focusing and corresponding pulse broadening. It is shown that a single measurement in one detection plane can fully characterize the electric field in all planes along the propagation axis. Furthermore, spatio-temporal properties of a truncated Bessel beam produced by an achromatic meta-axicon are explored. A comparison with a standard glass axicon that has similar

optical characteristics is demonstrated, accompanied by the hyperspectral analysis of the produced focal spots. This chapter closely follows Mamaikin et al. [158].

4.1   Metasurface Samples

In the following section, a brief description of metasurface samples used in the experiment is provided. A more thorough explanation can be found in [159–161]. SEM images of the samples are presented in [158].

The first sample we investigate in the current work is a monochromatic meta-lens designed for a single visible wavelength of 632 nm. The lens consists of silicon dioxide (SiO$_2$) nano-pillars of different diameters with the same height of 2 µm manufactured on a fused silica substrate. The numerical aperture of the meta-lens is measured to be 0.13 at $\lambda = 800$ nm. The focusing principle is shown in Fig. 4.1a in the case, when the incident beam contains a narrowband light at 632 nm wavelength. The distance where all the rays cross the optical axis, i.e. focal length, is engineered to be 1 cm. The pillar distribution on the surface features some lines of discontinuities reminiscent of a Fresnel lens design. When the incident light has a large bandwidth (Fig. 4.1b), this leads to a wavelength-dependent focal length similar to the diffractive optics. The optical image of the manufactured flat lenses on a fused silica substrate is shown in Fig. 4.1c.
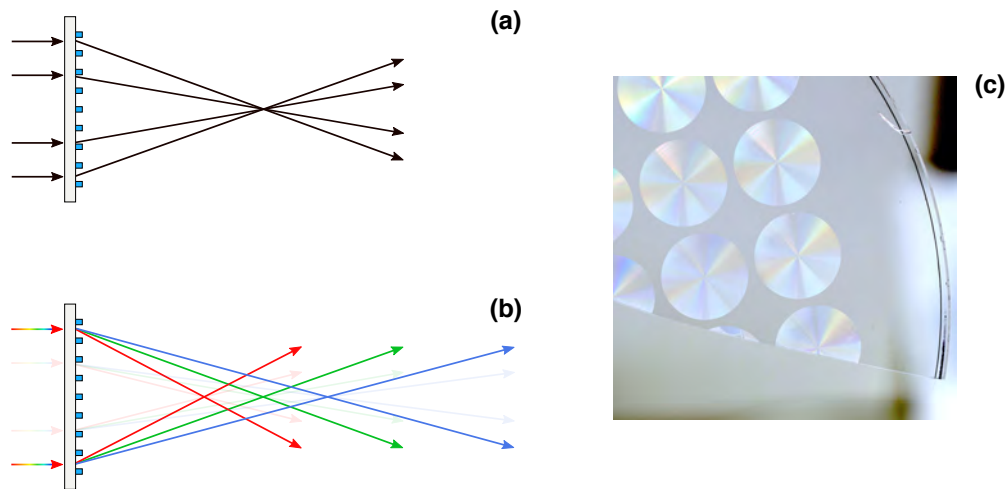
Figure 4.1: Monochromatic visible meta-lens sample. **(a)** Principle of the meta-lens designed for a specific input wavelength, 632 nm. **(b)** Chromatic aberrations produced by the flat lens when the input beam has broadband spectrum. **(c)** Optical image of the meta-lenses manufactured on a fused silica substrate.

In general, the metasurface-based devices are affected by chromatic aberration because they are inherently dispersive. However, recent research has demonstrated that relatively broadband metasurfaces can be realized [162–165].
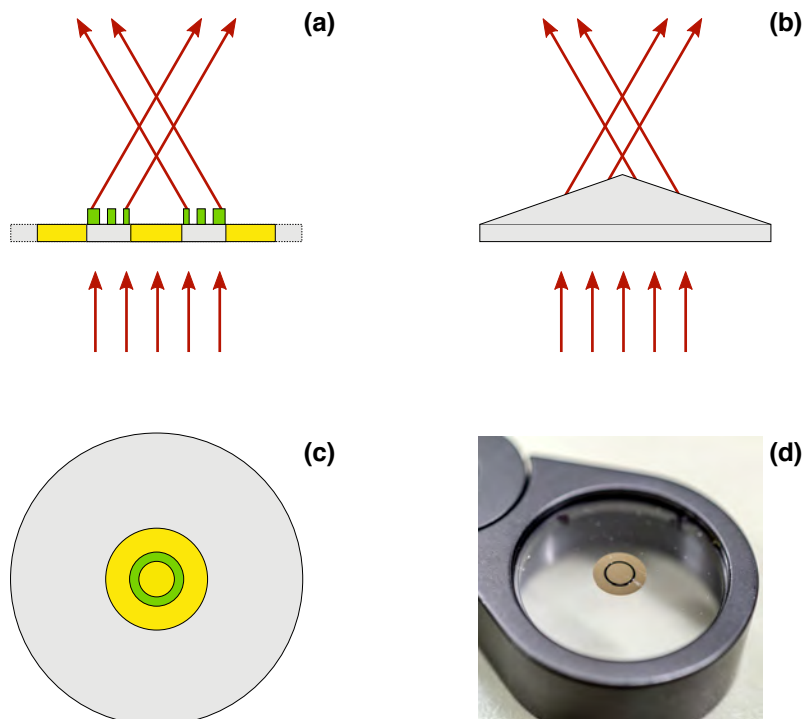
Figure 4.2: Achromatic meta-axicon sample. **(a)** Concept of a meta-axicon generating the Bessel beam. **(b)** A glass axicon producing the Bessel beam. **(c)** Schematic of the meta-axicon on a fused silica substrate. **(d)** Optical image of the manufactured meta-axicon.

The second flat sample that we study in the present work is an achromatic meta-axicon, which is specifically designed and fabricated for broadband wavelength operation [161]. This metasurface focusing element is composed of α-silicon nanofins with the same height, length, and width but different rotation angle $\theta(r)$, fabricated onto a fused silica substrate. In that way, a spatially varying phase delay $\phi(r)$ is introduced to the circularly-polarized incident light based on the Pancharatnam-Berry phase, which enables the realization of wavelength-independent focusing [166, 167]. A schematic of the meta-axicon, converting an incident beam to a Bessel beam, is illustrated in Fig. 4.2a, with a comparison to a standard refractive axicon (Fig. 4.2b). The ring of nanofins with the annulus size of 250 µm, surrounded by the gold aperture (Fig. 4.2c), deflects the light at an angle of 3.1 degrees, which corresponds to NA=0.055. The resulting focal length at $\lambda = 1.5$ µm is 3 cm. The optical image of the manufactured meta-axicon is depicted in Fig. 4.2d.

In general, nanostructures with azimuthal asymmetry exhibits birefringence. It can be understood from the fact that due to the rotation of each nanofin the effective refractive indices are different for orthogonal polarization states [168]. To maximize the performance of the meta-axicon, the geometric parameters of each nanofin are determined such that the nanofin acts as a miniature half-waveplate at an incident wavelength of 1.5 µm [168, 169]. If the incident beam is left-handed circularly polarized, then $\phi(r) = 2\theta(r)$, and the

emerging field is converted to a right-handed circularly polarized field. In our case, when the incident NIR light is not left-handed circularly polarized but has linear polarization, the entire nanofin arrangement is expected to introduce a decomposition into two beams with opposite helicity [165, 170]. A beam with the "correct" polarization to the designed sample converges, while the second beam gets the conjugate phase and diverges.

The EOS detection is primarily sensitive to one linear polarization state at a time. Here, the detection of the circularly polarized field produced by the meta-axicon is implemented for one linearly polarized component that lies on the extraordinary axis of the BBO. Thus, only a quarter of the power transmitted through the gold aperture of the meta-axicon contributes to the signal, requiring a decent amount of the incident intensity. Luckily, the OPCPA is powerful enough to provide pulses with high intensities for the measurement.

For the direct comparison of the focusing capabilities of the described meta-axicon with a refractive axicon, we chose an axicon made of fused silica with the edge thickness of 3.5 mm and the center thickness of 5.2 mm. The glass axicon approximates the optical properties of the meta-axicon: the deflection angle is ~ 3.5 degrees.

4.2 Extremely Chromatic Meta-lens

In this section, the focusing characteristics of the monochromatic meta-lens will be studied through its interaction with a broadband beam in the NIR region. The light source that is used for this purpose is the 14 fs OPCPA pulses, in the frequency range from 130 THz to 200 THz. To conduct the experiment, the meta-lens must be placed in the NIR beam path before the beam combining optic. The generated electric field is retrieved in the detection plane by the varying time delay between the NIR OPCPA laser source and the white-light sampling pulse.

The EOI measurement, demonstrating the electric field pattern in the detection plane, is illustrated in Fig. 4.3. The first row of images represents single field frames at time delays of 0 fs, -1.67 fs and -3.34 fs, which correspond to the maximum positive amplitude, zero crossing and a negative extremum of the electric field. The presence of the multi-ring, out-of-phase pattern around the central spot indicates the generation of some kind of aberration by the metasurface. This manifestation is to be expected, given that the meta-sample is designed for single-wavelength operation. The produced electric field structure becomes even more interesting, exposing its spatio-temporal distribution by fixing one spatial coordinate to zero, $E(x = 0, y, t)$ (Fig. 4.3d). The incident spectral components are distributed throughout the detection plane, forming a complex electric field pattern in time and space, due to the multiple focal planes that correspond to different spectral components. As a result, only a few optical components are focused into the EOS crystal, which leads to a significant bandwidth reduction in the imaged plane. Indeed, analyzing the brightest pixel from Fig. 4.3d and revealing its temporal waveform, it is clear that the pulse duration is dramatically increased (Fig. 4.3e). The spectral intensity derived from this waveform is presented in Fig. 4.3f. The spectrum clearly demonstrates that only the frequencies from 160 THz to 180 THz are focused. This relatively narrow bandwidth
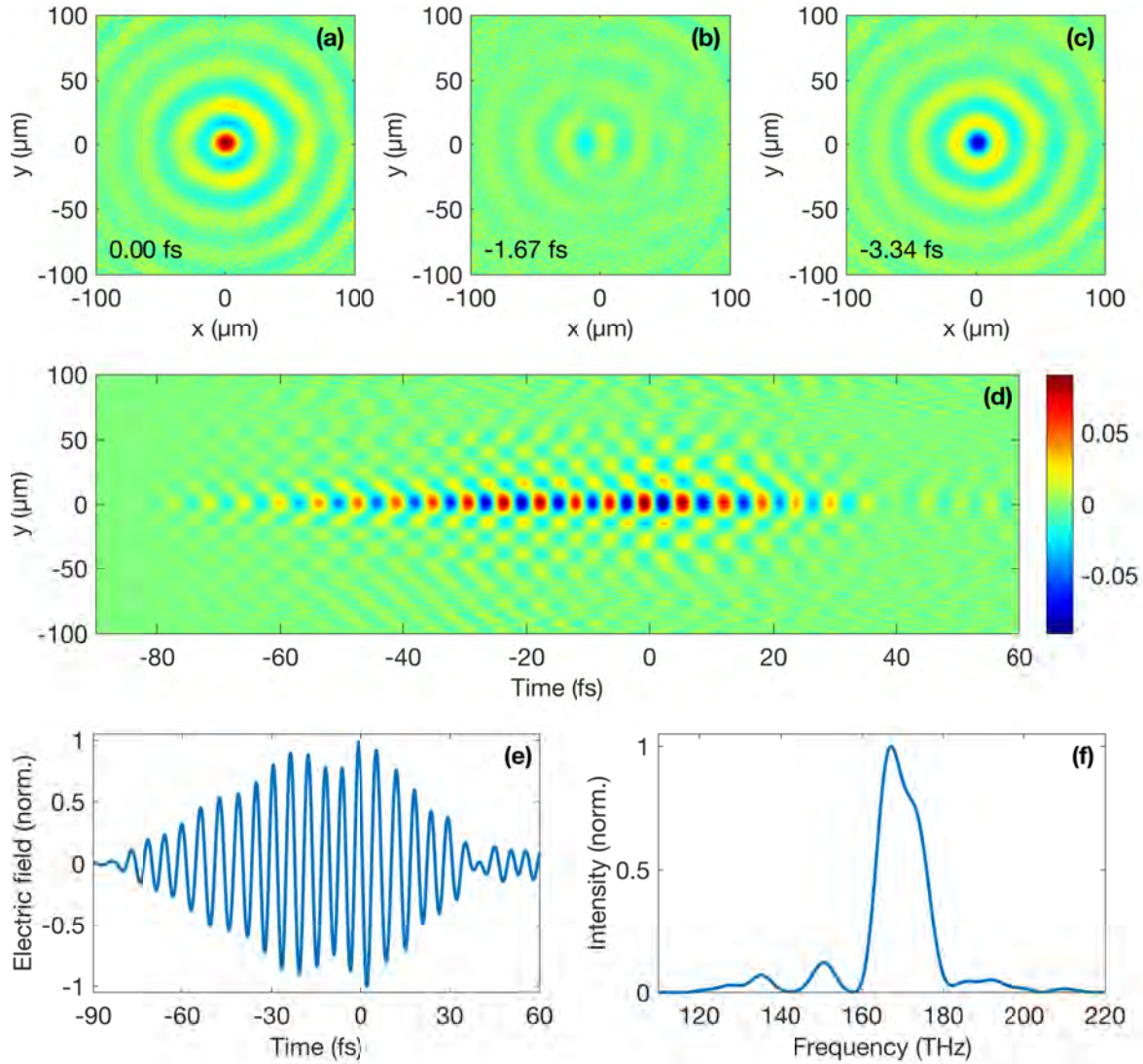
Figure 4.3: Characterization of the NIR field focused by the meta-lens with strong chromatic aberration. Electric field at the time of **(a)** highest field strength, **(b)** zero crossing and **(c)** negative maximum. **(d)** Spatio-temporal electric field distribution in the plane $E(x = 0, y, t)$. **(e)** Time-domain waveform at the point of the highest field strength $E(x = 0, y = 0, t)$. **(f)** Corresponding spectrum obtained by the Fourier transform of (e).

implies that the process of chromatic focusing leads to the stretching of the incident 14 fs pulse to about 48 fs, calculated as the FWHM from the corresponding temporal waveform.

As discussed earlier, EOI gives full spatio-temporal information about the electric field in the detection plane, which contains the entire bandwidth of the incident beam. In our case, only a narrowband spectral region is focused, appearing in the image as the most intense part at the center. However, the other spectral components, although out of focus in the detection plane are also present in the image, and this information is available. Consequently, the amplitude and phase of each spectral component within the incident bandwidth can be extracted to implement numerical simulation of their linear propagation.

Taking the Fourier transform of the obtained temporal waveforms in each pixel yields the complex spectrum in the frequency domain. The frequencies with known amplitude and phase are associated with the corresponding wave vectors $k = n\omega/c$. The 2D Fourier transform in space provides a decomposition of the light field into plane waves, and gives the transverse spatial frequencies and corresponding x and y components of each wave vector, i.e. k_x and k_y. As a result, each plane wave of the light field in the 3D Fourier-transformed matrix has a frequency, phase, and orientation. Thus, to calculate the form of the light field in any other plane along z axis for the distance Δz, a wave-vector-dependent phase shift $\Delta\phi$ should be added

$$\Delta\phi(k, k_x, k_y) = kd = \frac{k\Delta z}{\sqrt{1 - \frac{k_x^2 + k_y^2}{k^2}}}, \tag{4.1}$$

followed by the inverse Fourier transform, where $d = \Delta z/cos(\theta)$ is the effective propagation distance of the individual plane wave and θ is the angle between k_z and k. With this simple Fourier-optic procedure, it is possible to find an exact focal plane for each spectral component within the incident bandwidth through numerical shift of the crystal.

Such calculation is presented in Fig. 4.4, where red, green, and blue are mapped to 145 THz, 168 THz, and 189 THz. The first false-color image (Fig. 4.4a) clearly demonstrates the chromatic aberration produced by the meta-lens along the z axis, while the x coordinate is fixed to zero. The numerical calculation is done for the range of $-4000 < z < 4000$ µm from the original measurement ($z = 0$). The focal position for each color can be observed and even precisely determined. Accordingly, the $x - y$ false-color images in the second row represent the beam foci for the mapped narrowband frequency ranges around 145 THz (Fig. 4.4b), 168 THz (Fig. 4.4c), 189 THz (Fig. 4.4d), with the exact distance from the original plane. As a result, the flat lens leads to the spatial separation of the incident low- and high-frequency components along the optical axis on the order of ~ 2.4 mm.

To verify the feasibility of the Fourier-optic numerical displacement of the EOS crystal, one more measurement is carried out, when a physical shift of the crystal is done by ~ 1.5 mm towards the metasurface lens. The experimental results are presented in Fig. 4.5. A single frame of the generated field pattern is depicted in the $x - y$ image (Fig. 4.5a). The dynamical spatio-temporal image in Fig. 4.5b shows the modifying wavefront curvature, indicating that some spectral components are about to focus, others are strongly defocused.
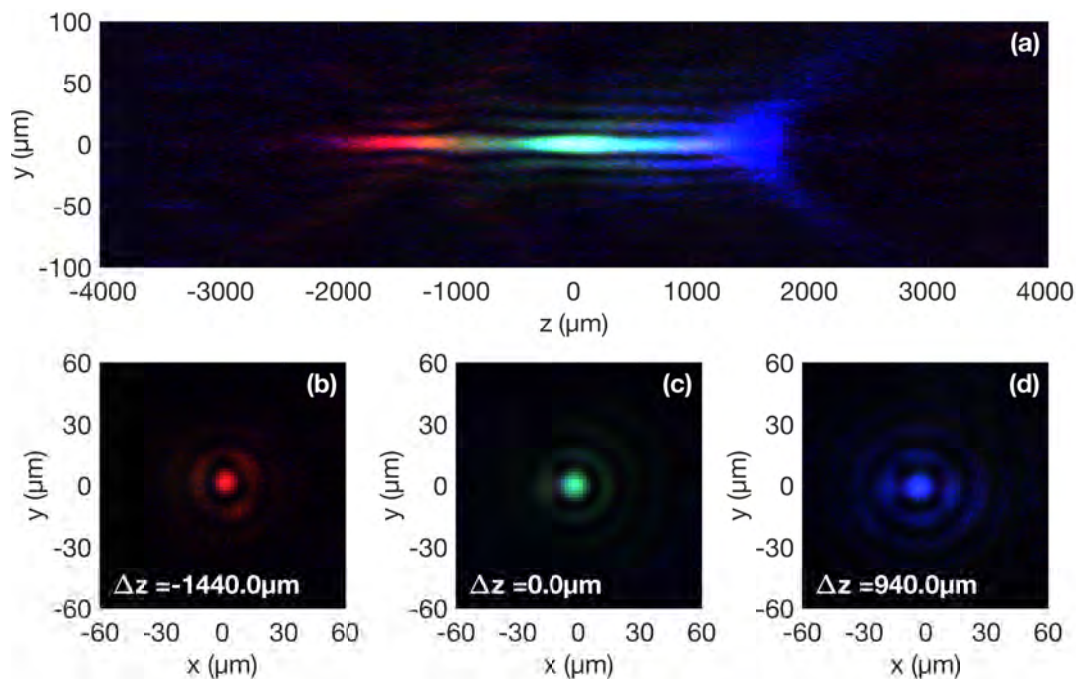
Figure 4.4: Visualisation of the chromatic aberration created by the meta-lens. **(a)** False-color $y - z$ image of different focus planes shifted numerically, where red, green, and blue are mapped to 145 THz, 168 THz, and 189 THz. **(b)-(d)** Cross-section images of the focus position for each mapped frequency.

The temporal evolution of the brightest pixel in Fig. 4.5c illustrates the broadening of the generated field in the new detection plane, with a pulse duration of 49 fs. In principle, shifting the detection crystal closer to the lens should make the low-frequency components dominate. The spectrum obtained by the Fourier transform of (c) naturally confirms it. Applying the numerical phase shift through the 3D Fourier transform and moving the detection plane along the z axis, false-color images can be obtained for the same frequency ranges: red, green, and blue represent 145 THz, 168 THz, and 189 THz (Fig. 4.5e-g). The physical crystal position is at $z = 0$. The focal plane of the red components is determined to be 100 µm away from the real crystal plane. The green components are about 1550 µm, which is in good agreement with the previous results. It has to be noted that the focal plane of the blue components cannot be reliably measured because this information is barely captured by the crystal. However, assuming agreement between this measurement and the one before (Fig. 4.3), an approximate focal plane can be numerically calculated.

It has been demonstrated that a single EOI measurement yields a cube of waveforms that can be exploited to calculate the light field form in any other plane along the propagation axis. The spatio-temporal distortions in the case where an incident beam contains a large bandwidth can be easily detected and potentially corrected to design a metasurface lens that maximally confines the light in both time and space.
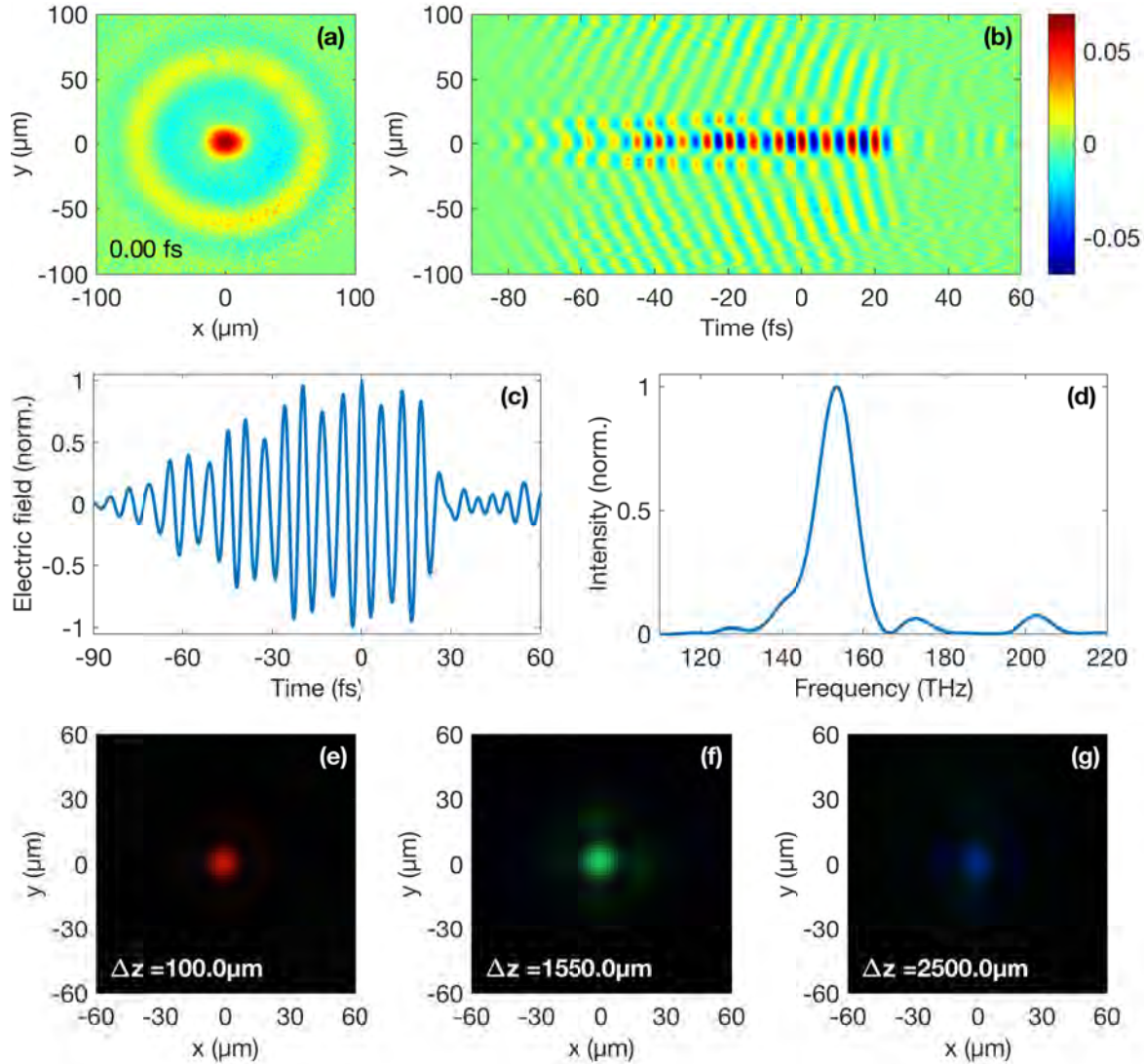
Figure 4.5: Characterization of the NIR field focused by the meta-lens after moving the detection plane by ~ 1.5 mm. Measured electric field **(a)** at the time of positive extremum and **(b)** along the y axis in dynamics. **(c)** The temporal evolution of the brightest pixel and **(d)** its corresponding spectrum. **(e)**-**(g)** Foci for each mapped frequency range (red, green, and blue represent 145 THz, 168 THz, and 189 THz), calculated numerically.

4.3 Light Focusing by Conical Lenses

Cone-shaped lenses or axicons are utilized to transform an incident Gaussian beam into a non-diffracting zeroth-order Bessel beam. The phase imparted to the light in transmission has a conical profile, i.e. the phase delay increases linearly with the distance from the center. The generated Bessel beam is only approximated within a finite area, as a true Bessel beam is spatially unbounded and carries an infinite amount of energy. As mentioned earlier, the electric field retrieval of spatially modulated beams is extremely difficult, especially on a few-cycle time scale. Basic field-resolved techniques such as standard EOS or FROG do not provide a reliable characterization of such complex-structured pulses because EOS averages the spatial field distribution and FROG prefers non-collinear geometry between the beam under study and its time-delayed replica to spatially separate the nonlinear signal. The EOI modality, in contrast, provides an individual waveform for each pixel in the cross-section, making the spatio-temporal detection of any beam with complex spatial structure readily accessible and reliable.

To investigate spatio-temporal properties of the few-cycle NIR pulses with a Bessel-like spatial structure, the axicon must be placed in the OPCPA arm before the beam-combining polarizer. In the present work, we study two completely different types of axicons - an achromatic metasurface axicon and a conventional refractive glass axicon. The comparison of these two samples is made on one day, under nearly identical experimental conditions using the same parameters in the processing.

4.3.1 Achromatic Meta-Axicon

Let us start with the spatiotemporal characteristics of the Bessel beam created by the achromatic meta-axicon. As the axicon focuses only one circularly polarized component of the incident linearly polarized light, the WGP projects the focused field $E(x, y, t)$ on two orthogonal axes and splits it into two constituents E_x and E_y, reflecting the former to the e-axis of the BBO crystal. Thus, the retrieved Bessel beam is expected to possess only one converging field component E_x due to the WGP and BBO with type-II phase-matching.

A typical EOI measurement, when the NIR light is focused by the metasurface axicon, is presented in Fig. 4.6. Three individual frames in Fig. 4.6a-c represent the electric field of the truncated Bessel beam at the highest positive strength, around zero crossing and a negative maximum, respectively. An ordinary spatial pattern described by a zeroth-order Bessel function of the first kind can be observed. In the process of scanning, a small reflection was noticed, which is for unknown reasons created by the meta-axicon. It can be also seen in the images as an intense spot with the coordinates about ($x = -20$ µm, $y = -10$ µm), which is in-phase with the first ring. This ellipse is a central core of the accompanying reflection. Luckily, the reflection is temporally delayed, marginally affecting the retrieved electric field. The spatio-temporal dynamics of the Bessel beam's electric field $E(x = 0, y, t)$ is depicted in Fig. 4.6d. The image clearly illustrates strong light confinement in both time and space, validating the achromatic characteristics of the flat axicon over the broadband incident light. In addition, three pixels are analyzed from the
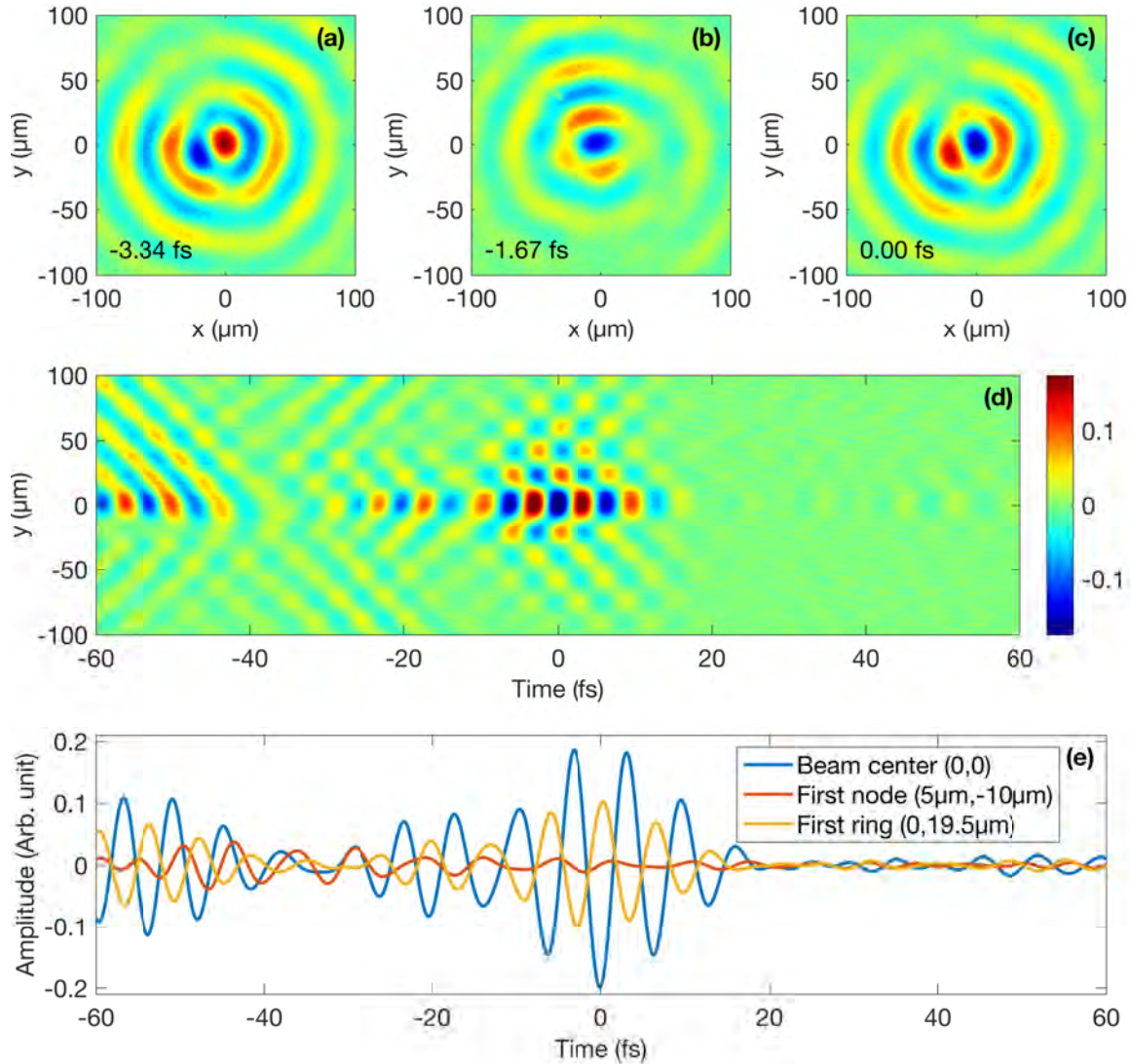
Figure 4.6: Electric field pattern produced by the meta-axicon at the time of **(a)** highest field strength, **(b)** close to zero crossing and **(c)** negative maximum. **(d)** Spatio-temporal electric field distribution in the plane $E(x = 0, y, t)$. **(e)** Time-domain waveforms at the center, first node and first ring of the truncated Bessel beam.

image, at the beam center, the first node and the first ring (Fig. 4.6e). The waveforms at the beam center ($x = 0, y = 0$) and the first ring ($x = 0, y = 19.5$ µm) exhibit out-of-phase behaviour, while the wave at the node ($x = 5$ µm, $y = -10$ µm) stays mostly unperturbed. The pulse durations given by the FWHM reach the nominal value of ~ 13.5 fs. The hyperspectral analysis of the truncated Bessel beam produced by the metasurface axicon will be presented in comparison with a glass axicon in the next subsection.

4.3.2 Conventional Glass Axicon

Glass refractive axicons have found many valuable applications in various research fields such as telescopes, atomic traps [171], corneal surgery [172], optical coherence tomography [173], optical trapping [174], etc., since their first invention in 1954 [175]. Particularly, an intriguing property of Bessel beams focused by an axicon have been recently found: the radiation at the focus might travel with subluminal speed due to the interference effects of two intersecting wavefronts. This exciting effect was observed through a time-resolved measurement in the center of the Bessel electric field in the THz range [176]. Nevertheless, spatio-temporal characteristics of the produced Bessel beams are still barely known, especially in few-cycle and sub-cycle temporal regimes.

Although a reflective design of the axicon has been introduced to remove chromatic aberration and group velocity dispersion [177], a conventional transmissive axicon is studied in the current thesis as the most available and usable optical element for creating truncated Bessel beams.

The EOI experiment with the glass axicon is performed with a minimal time interval after the measurement with the meta-axicon to maximally preserve the properties of the NIR pulse. In contrast to the meta-surface axicon, the incident linear polarization of the laser pulse focused via the glass axicon is maintained.

The measured electric field of the Bessel beam is pictured in Fig. 4.7. Corresponding $x - y$ slices of its spatial structure at time delays of a positive maximum, zero crossing and negative maximum are shown in Fig. 4.7a-c, respectively. The generated Bessel field pattern is relatively round and symmetric. The spatio-temporal evolution of the electric field $E(x = 0, y, t)$ in Fig. 4.7d illustrates interesting features in time and space: the temporal profile is not consistent over the profile of the focus. This is expressed in the distributed incident bandwidth over wide spatial and temporal regions. Temporal waves at the brightest pixel of the beam center ($x = 0, y = 0$), first node ($x = 5$ µm, $y = -10$ µm) and first ring ($x = 0, y = 19.5$ µm) are separately analysed (Fig. 4.7e). Although the waveforms are slightly stretched, the FWHM pulse duration at the beam center is measured to be 14 fs, similar to the incident pulse. It is noticeable that the longer wavelengths are retarded with respect to the shorter ones due to the glass dispersion of the axicon. The trailing frequencies do not contribute to the final pulse duration but have the relatively high amplitude. The temporal waveform of the first ring is calculated to be about 27 fs. However, not only temporal chirp leads to longer pulse durations. The complete picture of the spatio-temporal couplings is better to represent in the frequency domain as many interesting optical phenomena can be unveiled with a single hyperspectral image.
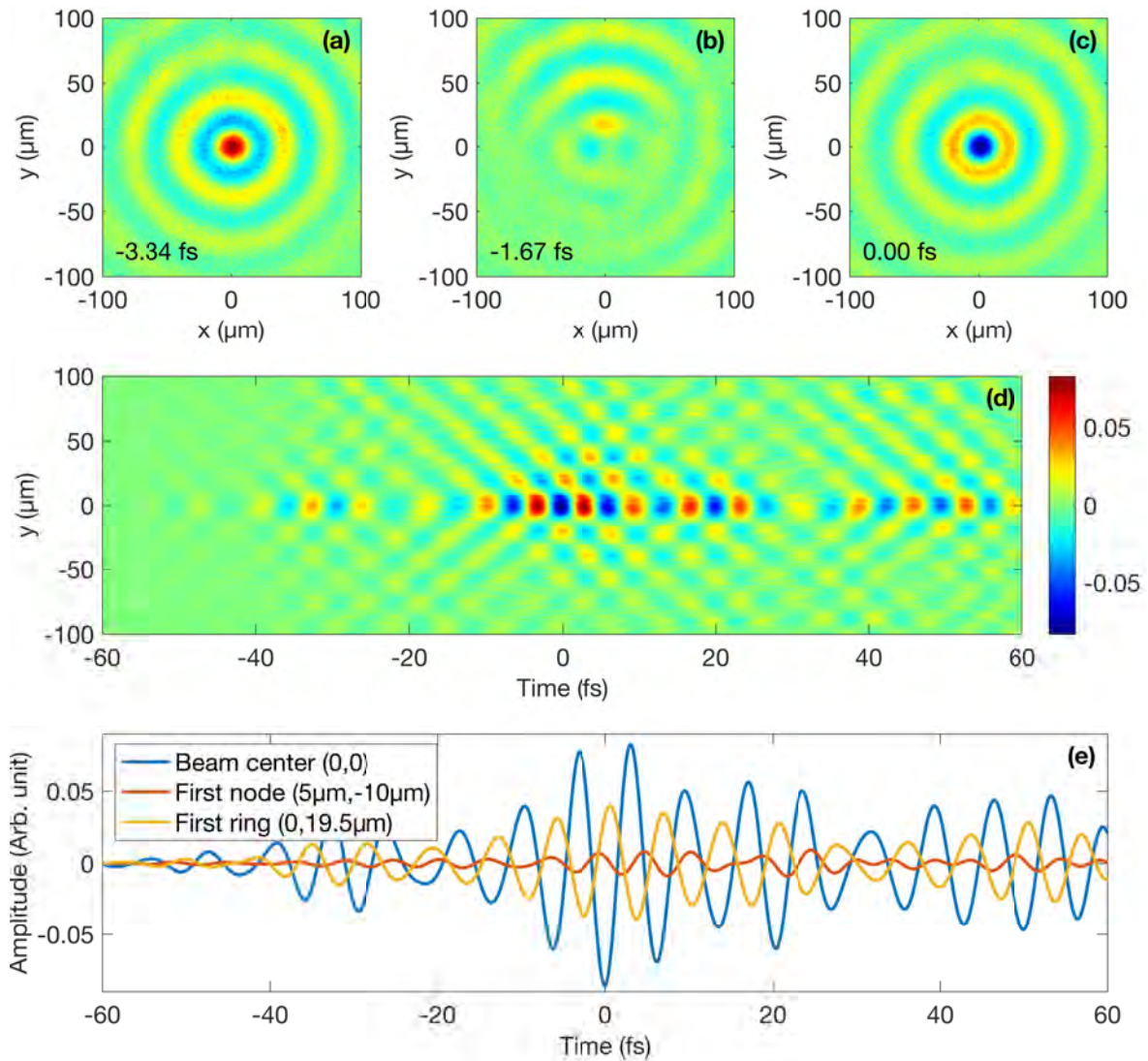
Figure 4.7: Electric field pattern produced by a glass axicon at the time of **(a)** positive field strength, **(b)** zero crossing and **(c)** negative field maximum. **(d)** Spatio-temporal electric field distribution in the plane $E(x = 0, y, t)$. **(e)** Time-domain waveforms at the center, first node and first ring of the truncated Bessel beam.
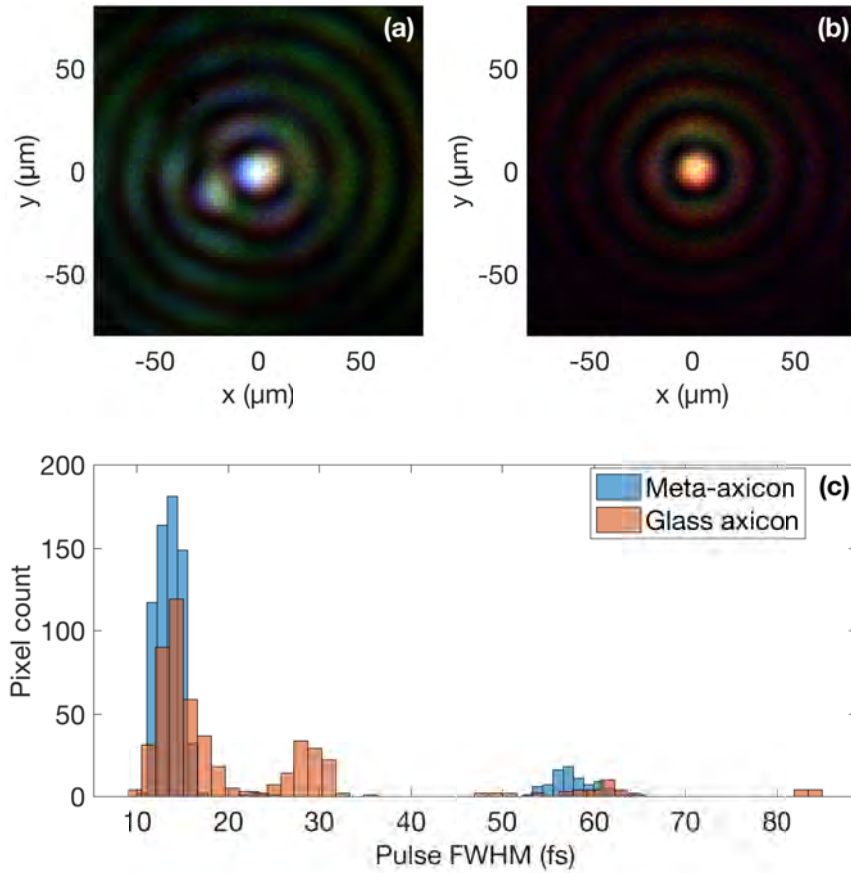
Figure 4.8: Focusing capabilities of the meta-axicon and similar glass axicon. False color images of the beam (red, green, and blue are mapped to 135 THz, 164 THz and 192 THz) focused by **(a)** the meta-axicon and **(b)** the glass axicon. **(c)** Histogram of pulse durations after focusing with the axicons counted in number of pixels.

The spatio-spectral analysis of the Bessel beams focused by the meta-axicon and the glass-axicon is done through the Fourier transform of all corresponding temporal waveforms at each pixel of the cross-section. The incident bandwidth is divided into three narrowband colors: 135 THz, 164 THz and 192 THz represent red, green and blue shades. The spectral intensity factors, which are applied to identify spatial color spreading, are identical for both false-color images. The hyperspectral comparison of the focusing capabilities of the investigated axicons is presented in Fig. 4.8. The Bessel profile created by the metasurface axicon (Fig. 4.8a) has consistent color distribution, with a whitish central core. The spatial separation of the input wavelengths in the core is partially distinguishable, which is probably carried over from the incident OPCPA laser pulse (see Chapter 3). The nodes and antinodes of the Bessel structure show uniform radial distribution for all frequencies, yielding a significant amount of pixels with the original ~ 14 fs pulse duration in the histogram (see Fig. 4.8c).

An interesting peculiarity can be discovered in the Bessel hyperspectral pattern produced by the glass axicon (Fig. 4.8b): the core mostly contains longer wavelengths rather than shorter ones. This induces the reduction of local bandwidth in this region and longer pulse durations. The second important spatio-spectral effect can be noticed in the rings of the Bessel beam: higher frequencies (green colors) are localized in the inner zones of the rings and lower frequencies (red colors) are arranged in the outer zones. This phenomenon is directly connected to the chromatic aberration induced by the refraction of the pulse. Altogether, these two spatio-spectral phenomena increase the number of pixels with longer pulse durations in the histogram for the glass axicon (Fig. 4.8c). As a result, the meta-axicon consisting of subwavelength-space phase shifters demonstrates an incredible quality of focusing in comparison with the standard glass optics, achieving shorter pulse durations and higher peak intensities simultaneously in space and time.

4.4   Outlook

In this chapter, we have demonstrated imaging of the far-field electric fields, output wavefront of which has been locally shaped using an array of silicon-based nanostructures. The metasurface optical devices have a huge potential to fully replace the traditional refractive and diffractive optical elements, offering full control over the light properties in an ultrathin and compact planar design.

The imaging apparatus has opened a door towards the spatio-temporal characterization of few-cycle pulses with complicated spatial structures generated by metasurface optics. The chromatic aberrations, which are usually present in any transmissive optical components unless a special complex arrangement is implemented, can be well detected and extracted to provide a full picture of light focusing. The imaging modality simultaneously captures a complete array of individual waveforms in one detection plane that can be utilized to establish the form of the light in any other plane along the propagation axis. This can be done by performing temporal and spatial Fourier transformations and applying a wave-vector-dependent phase shift independently to each plane-wave component, followed by inverse Fourier transform. Therefore, compensating spatio-spectral distortions of a constructed meta-device is feasible through the numerical backpropagation of the focused light to the metasurface plane and recalculating the phase profile in order to design and produce a flat optic with a required electric field at the focus.

To realize the wavelength-independent focusing, a metasurface axicon has been designed and manufactured with a spatially varying phase shift relying on the Pancharatnam-Berry geometrical phase. The achromatic capabilities of the meta-axicon are experimentally confirmed, with the extracted pulse durations similar to the incident field. The glass refractive axicon with close optical characteristics have been studied, as well, to compare spatio-temporal properties of the produced Bessel beams. The interesting fact has been found via hyperspectral analysis: the rings of the truncated Bessel beam focused by the glass axicon tend to contain spatially separated wavelengths. The lower frequencies are concentrated in the outer regions of the rings, while the higher frequencies stick to the inner

regions. This behavior can be easily understood from the physics of refraction: shorter wavelengths are deflected closer to the optical axis than the longer-wavelength components. In the end, the local bandwidth is partially reduced, resulting in longer pulse durations in such regions. The metasurface axicon has demonstrated a superior quality of focusing over a similar glass-made axicon.

The optical characteristics of metasurface structures in the interaction with few-cycle pulses have been just started to be explored. EOI is capable of facilitating the construction of the new generation of flat lenses and other metasurface optical components, providing a complete picture of light behavior after the interaction with the nanostructure-filled interface. Metasurface devices such as metasurface vortex phase plates or meta-holograms can be also investigated with the imaging apparatus. Although only the formation of electric fields in the far-field has been shown yet, the near-field information is also accessible with EOI. This exciting research area will be addressed in Chapter 5.

Chapter 5

Near-field Microscopy

Electromagnetic radiation emitted by a dipole has one particular phenomenon that attracts the attention of a huge number of scientists - some portion of the radiation with wave vectors $k^2 < k_x^2 + k_y^2$ does not propagate to the "far-field" of the dipole and decays exponentially. The region where it occurs is often referred to as "near-field", with the typical distances less than the exciting wavelength. For visible light imaging, sub-wavelength structures, such as biological cells or nano-antennas require a spatial resolution on the nanometer scale, which is not easily achievable due to the presence of the fundamental light confinement limit in the far-field. Therefore, access to the near field is in great demand in associated research areas. Modern techniques such as near-field scanning optical microscopy [178–181] and other scanning probe methods [182, 183] can perform imaging with spatial resolution below 50 nm. However, a two-dimensional raster scan of the excitation laser light leads to long acquisition times, which in the case of dynamic samples cannot provide a real-time picture of rapid changes. In contrast, a wide-field geometry based on EOS has been developed in the THz range, where a sample and a detection crystal are very close to each other to capture near-field information in real time before diffraction has occurred and form a far-field image across the wide area [102, 109].

With the time-resolved access to the near-field region, direct observation of the electric field dynamics within different plasmonic devices (including metasurface optics described in Chapter 4) and the formation of local fields is feasible [109, 184] . The time-domain picture of energy exchange with the surrounding materials can be straightforwardly retrieved, revealing the fundamental light-matter energy transfer dynamics behind the plasmonic resonances. In addition, label-free imaging of chemical components or biological samples placed on a thin crystal can be achieved with sub-wavelength resolution in real-time through the measurements of resonant absorption for each temporally resolved pixel [19, 110, 185].

In this chapter, the basic principles of THz real-time near-field imaging are transferred to the near-infrared regime. A couple of basic near-field EOI geometries is discussed, with the pros and cons of each approach. The detection of field enhancement generated by a collection of silver-coated microparticles is shown with subwavelength spatial resolution. Both uniaxial and isotropic EOS crystals are tested for this purpose. This chapter partially follows Mamaikin et al. [158].

5.1 Near-Field Geometry

Near-field techniques are based on the interaction of probe radiation with a sample under investigation within a very short distance from the sample. Unlike traditional near-field schemes, where the probe light is localized to a sub-wavelength scale, THz wide-field EOI relies on the immediate upconversion of the scattered THz light to SFG in a dedicated crystal. At the moment, two principal designs successfully operate in the THz near-field imaging, providing near-field images in a wide-field geometry: transmitted- and reflected-probe configurations (Fig. 5.1). Both optical schemes can be transferred to the NIR and visible spectral ranges, with the accompanying benefits of high-frequency EOI.
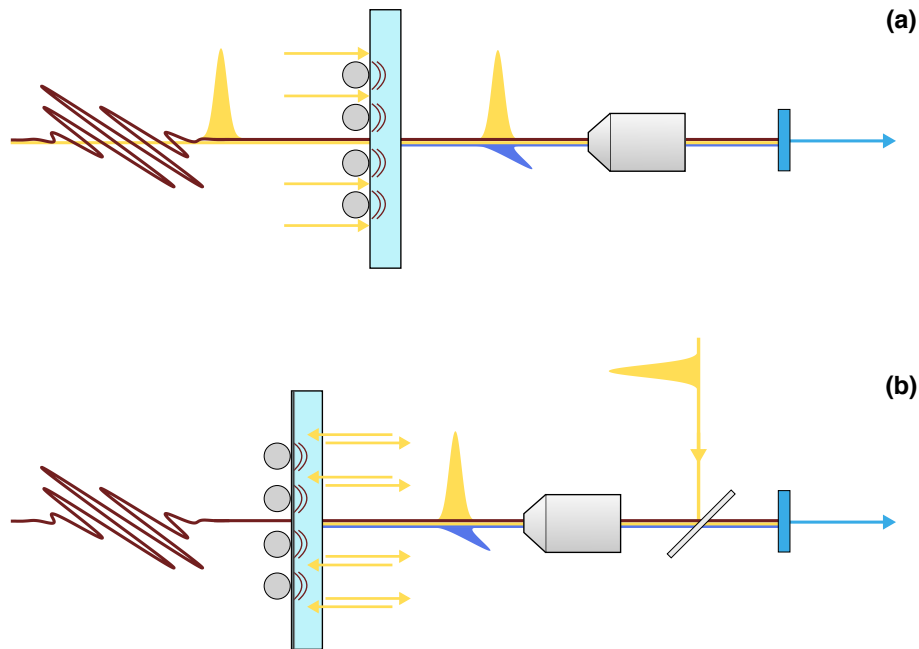
Figure 5.1: Typical near-field imaging geometries. **(a)** Transmitted-probe geometry, when the test and probe pulses collinearly enter the crystal, on which a sample is deposited. **(b)** Reflected-probe geometry, when the probe pulse enters the crystal from the back side and is reflected back by a high-reflection coating on the front surface.

In the transmitted-probe geometry, the optical layout is similar to the standard EOS and EOI schemes, described in the previous chapters: the white-light probe and NIR beams pass collinearly through the EOS crystal (Fig. 5.1a). The investigated nano-structures must be deposited on a sufficiently thin crystal to capture near-field radiation. In this case, the sample can be resolved with sub-wavelength resolution through the nonlinear interaction of the scattered light with the probe pulse. If the scattered NIR wave vectors are directly collected by a microscope objective, the resulting numerical aperture will be substantially larger compared to the case of EOI. The imaging modality allows for a signif-

icant reduction of the required numerical aperture, which is determined by the SFG wave vectors, through momentum conservation in the nonlinear upconversion (see Fig. 1.10).

The advantage of the transmitted-probe configuration is the simplicity of the setup, without implementing additional path manipulation or using customized optical components. However, the drawback of the scheme appears with the direct deposition of the resonant target on surface of the crystal — the sample simply blocks a substantial amount of the probe beam, which is supposed to generate SFG with the enhanced NIR field and then produce an image of this field on the CCD. Therefore, the detection of the enhanced field is considerably degraded, and the images contain the NIR field information only at the edges of the target. In addition, in the transmitted-probe geometry, it is extremely important to avoid resonant effects of the sample with the probe, otherwise, modifications of the probe light properties can be introduced.

In the reflected-probe geometry, the optical layout has to undergo a few optical path modifications: the probe light and the NIR beam enter the EOS crystal from different directions (Fig. 5.1b). The path trajectory of the excitation NIR field is not changed, and it still interacts with the resonant target, which is deposited on the front surface of the crystal (left-hand side in the presented figure). However, to avoid the interaction of the probe with the sample and corresponding light-blocking, the white light enters the crystal from the back side (right-hand side in the presented figure). In this configuration, the front surface of the crystal must have a high-reflection coating to send the probe light back to the imaging system. As an option, to prevent additional reflections from the back surface, an anti-reflection coating can be implemented on the back side, as well.

The reflected-probe scheme leads to better and cleaner images with complete near-field information, emerged from the sample. Since the probe pulse is minimally affected by the sample, there are no great concerns about possible resonant phenomena between the structure and the probe. However, the probe should pass through a microscope objective twice, back and forth. The typical working distance of a 20x objective is about 2 mm, and less for objectives with higher magnification. The main difficulty is the compression of the probe light - a large amount of dispersion accumulated in the lens system of the objective should be carefully compensated to attain strong SFG and preserve high contrast of the extracted images. A feasible option in this case is the use of a reflective objective, which naturally introduces spatial filtering by blocking a central region of images. A microscope objective with long working distance (usually about 15 mm) can be also tested. Finally, the main drawbacks of the reflected-probe geometry are the fabrication of high-reflection coating directly on the crystal surface, specifically for a broad bandwidth of the probe beam, and a great deal of dispersion introduced by typical transmissive microscope objectives.

In the THz near-field imaging, the reflected-probe geometry is more common, as the physics behind the EOS detection with THz frequencies slightly differs from that of high-frequency EOS [17]. In the current thesis, we stick to the first, transmitted-probe scheme, as a primary goal of the work is to demonstrate a proof of principle of high-frequency near-field EOI. The optical setup does not require special optical materials or dedicated target design, allowing for the realization of the experiment with the already built imaging system through a deposition of a resonant sample on a thin EOS crystal.

5.2   Field Enhancement with Microparticles

To induce field enhancement with a particular incident wavelength, a resonant sample must be carefully chosen. The most primitive sample for this mission is a collection of metallic spherical nano-scale particles, which are widely exploited in the visible spectral range [186–188]. However, in the NIR regime with 1.9 µm wavelength, preferable particle size is on the order of ~ 1 µm, while the enhancing properties of noble metals decrease with longer wavelengths. Due to the limited number of offers on the market with the precise diameter of microparticles, it has been decided to test resonant characteristics of silver-coated solid-soda-lime-glass microspheres with varying sizes from 1 µm to 7 µm.

By depositing the aggregation of microspheres on the surface of a thin EOS crystal, we expect to locally enhance the NIR electric field in the vicinity of protrusions and randomly-formed small cavities and detect the enhanced field using the EOI technique [189]. To resolve the sub-wavelength properties of the electric field around the spheres, the 4x microscope objective of the imaging system is replaced with a 20x objective (NA=0.4). In this way, spatial structures of about 0.9 µm can be resolved (see Section 2.3).

5.2.1   Detection using a BBO crystal

In the near-field EOI experiments, the detection crystal plays an important role in obtaining a strong, clean EOS signal and as high as possible spatial resolution. Usually, the crystal thickness is favored to be either comparable or less than an exciting wavelength. A 12 µm thick type-II BBO crystal is utilized for our EOI measurement as the thinnest available crystal at the moment. Besides, near-field effects additionally exploit surface nonlinearities at the surface of the BBO, increasing the contract of near-field images.

To cover a larger transverse area of the BBO's surface with the deposited microspheres and increase a probability of detection of sub-wavelength near-field radiation, the NIR beam is not focused. As a result, the collimated beam with ~ 0.12 mJ pulse energy at 1.9 µm wavelength illuminates more microparticles, providing extra pixels in the cross-section with temporal waveforms for individual analysis. The EOI measurement, obtained by varying the time delay between the white-light probe and NIR beam, is presented in Fig. 5.2. A wide-field image of the peak intensity distribution obtained simultaneously in each pixel can be observed in the center of the picture (Fig. 5.2a). The brightness of the pixels corresponds to the maximum local intensity, measured in the time delay window. The regions with nearly zero intensity are the areas, where the microspheres are located, blocking the probe light and carrying no intensity to the CCD. The regions with a relatively moderate intensity experience a regular EOS signal and follow the amplitude of the NIR field. These regions are considered as adverse because the near-field features are usually disguised there and not distinguishable from the background.

A few spots in Fig. 5.2a have distinctly stronger intensities with respect to the average value - they are emphasized with white squares. Two such regions in a zoomed-in view can be seen in Fig. 5.2b and Fig. 5.2c, with the enhanced field within a few pixels. As proof that the retrieved images do not correspond to noise or defective pixels but the
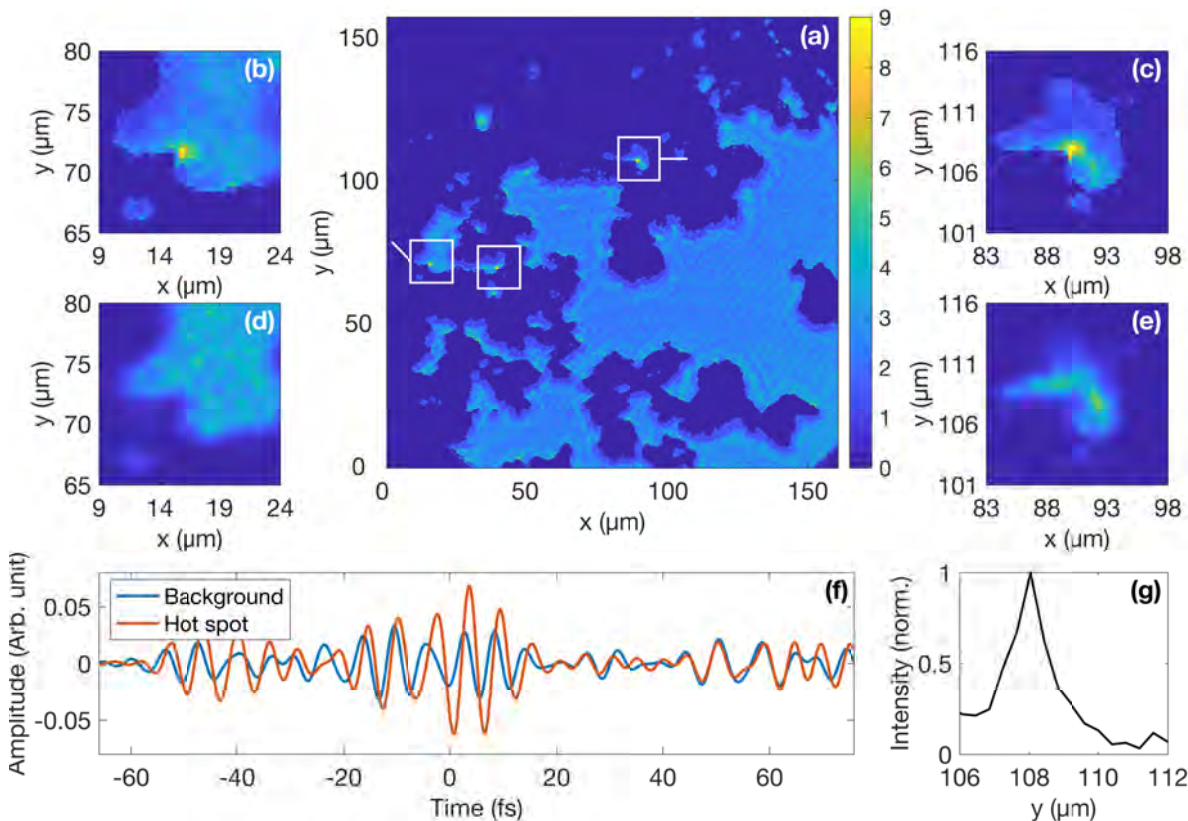
Figure 5.2: Time-resolved imaging of the electric field enhanced using silver-coated microparticles and detected with BBO crystal. **(a)** Peak intensity distribution of the BBO surface with deposited microspheres. **(b)** , **(c)** Enlarged images of the most intense regions of (a). **(d)** , **(e)** The same regions without 1.9 µm exciting beam. **(f)** Time-domain waveforms at the brightest pixel and unaffected pixel of (c). **(g)** Cross section of the hotspot in (c), indicating FWHM of 1.2 µm.

actual resonance, the same spatial areas are demonstrated in Fig. 5.2d and Fig. 5.2e, respectively, in the transmission of only white-light probe intensity, i.e. the exciting NIR beam is blocked. The sharp edges of the images in Fig. 5.2b and Fig. 5.2c with respect to their counterparts are due to the gating of pixels with insufficient probe power. For the direct observation of temporal properties of the enhanced pixel in Fig. 5.2c, its time-domain waveform and a wave averaged over a few neighboring pixels in relatively unperturbed free space is exposed in Fig. 5.2f. The enhanced field at the time delays around 0-10 fs has approximately twice the amplitude than the one of the background and closely follows its shape at relatively long positive delays.

The geometrical dimensions of the resonant effects are important to calculate for the estimation of spatial resolution of the imaging system. This evaluation yields only a rough resolution value, as the near-field phenomena presented in Fig. 5.2 are casually formed. The detailed analysis of spatial resolution needs to involve a specially prepared sample,
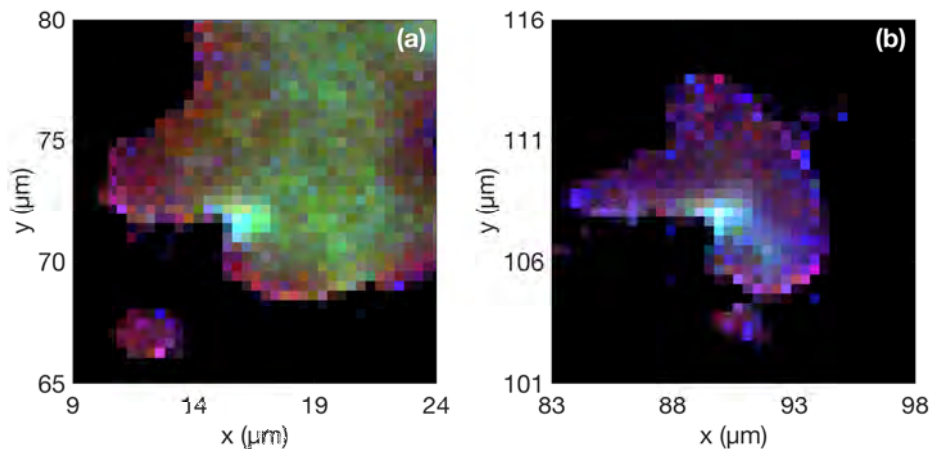
Figure 5.3: Hyperspectral view of the detected spots with the enhanced field. False-color images of **(a)** the first and **(b)** second regions with the detected near-field features, where red, green, and blue correspond to 145 THz, 165 THz, and 180 THz, respectively.

spatial characteristics of which are known or extracted using an electron microscope. The approximate transverse contour of the near-field hotspot of Fig. 5.2c along the y axis is depicted in Fig. 5.2g. The FWHM of the retrieved profile is calculated to be 1.2 µm, confirming a sub-wavelength scale of the resonant feature. More importantly, the imaging system is capable of resolving such micro-structures, opening a path towards the wide-field near-field imaging in the near-infrared spectral range with sub-wavelength spatial resolution.

In the field of plasmonics, an experimental knowledge behind the formation of plasmonic resonances is great of importance. In particular, precise information about the wavelength that leads to the formation of resonant phenomena is very crucial, especially if the incident laser source contains a broad bandwidth. This insight could facilitate the development of the next generation of plasmonic structures, carefully designed for a specific incident wavelength, and a better understanding of the interaction of light with plasmonic arrays. A distinctive feature of the EOI method is the ability to locate all incident frequencies in the wide-field geometry by converting the temporal waveforms at each pixel into the Fourier domain. With this simple procedure, the resonant wavelength can be isolated from other wavelengths that do not contribute to the excitation.

The hyperspectral analysis of the two regions, where the field enhancement has been found, can be seen in Fig. 5.3, where red, green, and blue correspond to 145 THz, 165 THz, and 180 THz, respectively. The color intensity factors for both images are applied equally. In the false-color images, one can clearly observe that the resulting hotspots in the lo-cations of resonant protrusions experience a broadband excitation. The regions at the edges of microspheres are prone to contain red/blue spectral components, while the free crystal space is mostly phase-matched to the green shades. The phase-matching of out-of-resonance frequency components leads to the obscure near-field signal in thin birefringent crystals, significantly reducing the detection efficiency of the EOI near-field apparatus.

5.2.2   Detection using a ZnS crystal

The EOI measurement, described below, is an attempt to improve the sensitivity and detection characteristics of resonant areas that are dim in comparison to the phase-matched background signal, like in the previous experiment. In general, the main goal of the near-field EOI is to achieve clear separation between the near-field effects and the background signal and maximally suppress the latter. Unluckily, the finite thickness of the BBO yields the accumulation of the background EOS signal along the propagation in the crystal, eventually beating the near-field signal. One advantage of the near-field radiation compared to the free-space EOS signal is the presence of surface nonlinearities, which can additionally facilitate the SFG process. We believe that the detected hotspots in the previous subsection also took advantage of the crystal surface, which allowed for better upconversion of the enhanced radiation, becoming detectable in the EOS image.

Stimulation of the surface nonlinearities seems like the right approach to improve the detection of near-field phenomena. It can be accomplished by using a crystal with a larger nonlinear coefficient compared to conventional EOS crystals. However, the bire-fringent nature of thin EOS crystals leads to strong phase-matching of the background signal. Therefore, an optimal crystal for the goals we pursue must have a larger nonlinear coefficient and be non-birefringent.

The nonlinear polarization in the case of sum-frequency generation in a $\chi^{(2)}$ medium under conditions of low-frequency excitation and the Kleiman symmetry can be expressed through d_{eff} for a fixed geometry [25]

$$P(\omega_3) = 4\epsilon_0 d_{eff} E(\omega_1) E(\omega_2), \tag{5.1}$$

where $\omega_3 = \omega_1 + \omega_2$. For the BBO crystal, which was utilized for the near-field detection, $d_{eff} \approx 1.76$ pm/V, assuming type-II phase matching with $\theta = 27°$. In our opinion, a good candidate for the near-field EOI measurement is a zinc sulfide (ZnS) crystal with $d_{eff} \approx 2.22$ pm/V, which is relatively cheap and widely available. This crystal does not display birefringence because of a cubic lattice but possesses a noncentrosymmetric struc-ture in the form of zincblende (β-ZnS). Moreover, ZnS material is highly dispersive for the probe frequencies (GVD ≈ 560 fs^2/mm at 0.8 µm), preserving the probe pulse to be short only for the first few microns of the crystal.

The EOI measurement fully replicates the one with the BBO crystal: microspheres are deposited on a 500 µm thick ZnS crystal (MTI Corporation) in the transmitted-probe geometry. The peak intensity distribution of the signal with two zoomed-in regions is depicted in Fig. 5.4. Unfortunately, the ZnS crystal does not provide sufficiently strong EOS signal and, as a result, the extracted images contain an extreme amount of noise. A detailed analysis of the pixels from the retrieved 3D matrix was additionally made. Some pixels exhibit the behavior similar to field enhancement, but the noise level does not allow us to confirm that this signal is actually related to the near-field effects. The situation is additionally deteriorated by the fact that the sample blocks the probe light. Nevertheless, a variety of work still needs to be done in the direction of improving near-field detection. The most obvious option is a realization of the reflected-probe geometry, where a resonant
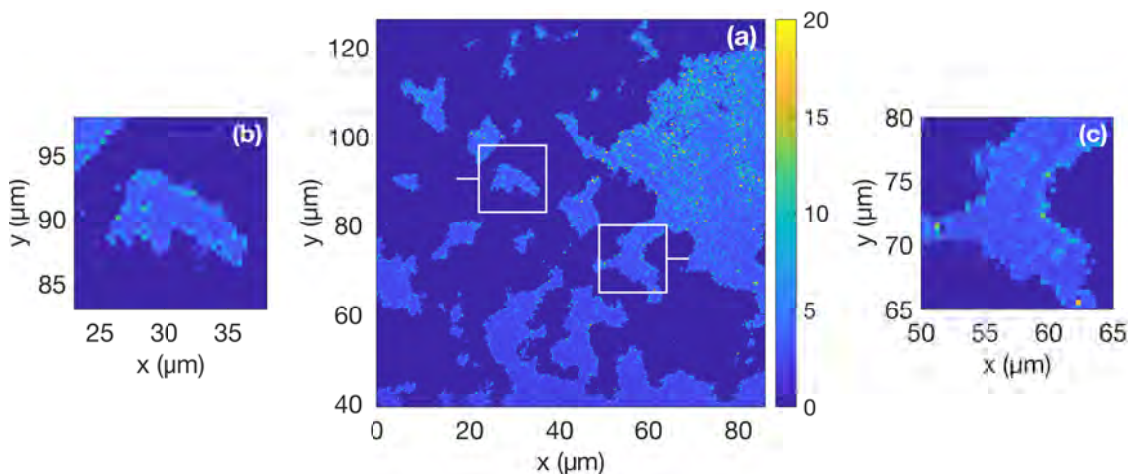
Figure 5.4: Imaging of the electric field detected with ZnS crystal. **(a)** Peak intensity distribution of the extremely noisy signal on ZnS surface with deposited microspheres. **(b)** and **(c)** are two zoom-in regions around the microparticles.

target does not interact with the probe light. A comprehensive search for better crystals that possess necessary optical properties for low-noise near-field EOI detection is valid, as well. In addition, the resonant sample can be directly embedded into a nonlinear medium, providing maximum interaction of the enhanced field with the detection crystal.

5.3   Outlook

In this chapter, we have demonstrated the near-field EOI detection in the near-infrared spectral range. It is important to note that the presented EOI measurement is only a proof of principle of the near-field detection when randomly oriented microspheres create a few spots with field enhancement characteristics. Nevertheless, it has been clearly shown that the introduced imaging technique is capable of providing sub-cycle temporal and sub-wavelength spatial resolution. In this matter, spatial field structures of about 1.2 µm are successfully resolved, beating the fundamental diffraction limit in a new way, without a raster probe scan. It is achieved using a nonlinear interaction of the near-field NIR radiation with a broadband probe pulse simultaneously at each pixel in a birefringent crystal, during which all properties of the near-field light are converted to a narrowband spectral region in the visible range, additionally reducing the effective numerical aperture. However, due to a large angle of near-field wave vectors, the difficulty of phase-matching arises. A viable solution lies in the use of extremely thin EOS crystals or even surface nonlinearities.

The wide-field EOI geometry enables the realization of real-time measurements of two-dimensional samples such as plasmonic devices or organic structures with the near-infrared light. This can provide new knowledge about the formation of local fields within the resonant targets as well as the light-matter interaction of the enhanced field with a surrounding

medium. Each pixel experiences the same incident electric field in the time domain and, thus, a reference signal is provided automatically in the transverse area beyond a sample. In this regard, the precise information about the exciting wavelength behind the resonant phenomena can be retrieved through the conversion of all temporal waveforms to the frequency domain and corresponding hyperspectral image. Moreover, the entire apparatus can be directly transferred to the visible optical region through the light synthesis experiments, where the research field is deeply coupled to plasmonic nanostructures.

More studies towards extracting cleaner near-field images have to be accomplished. A dedicated experiment requires a careful look at the resonant sample, which should excite near-field radiation and provide as high as possible contrast of the field images. This also involves suppression of the background free-space EOS signal and stimulation of the upconversion of near-field radiation. Huge potential in achieving these objectives has the reflective-probe EOI geometry, where a resonant sample does not influence the probe propagation, generating more SFG in the spatial regions where the sample is in direct contact with the detection crystal. This scheme chiefly demands a customized EOS crystal with a high-reflection coating on top as well as the dispersion compensation of the broadband probe light, which passes through the lens system of a microscope objective.

Chapter 6

Conclusion

Direct access to the time-dependent few-cycle electric fields has opened up new avenues into the study of modifications in the femtosecond scale that a sample experiences during a strong-field excitation. The measurements of the optical response of a system became possible by means of novel metrology schemes, without the need for complex retrieval algorithms. One of the most exciting investigations fulfilled in this direction is the time-dependent reconstruction of fundamental mechanisms of energy transfer between a solid and a few-cycle visible pulse [6]. However, in more complicated photonic systems, where a sub-cycle transfer dynamics are directly coupled to charge movements, spatiotemporal metrology schemes are required. Strict conditions involving both sub-cycle temporal and sub-wavelength spatial precision are necessary to resolve light-matter dynamics as a function of time and space. So far, complete spatiotemporal field characterization via electro-optic imaging has been limited to the terahertz frequencies. It has enabled many inspiring experiments including nonlinear dynamic response in a metamaterial structure [111] and formation of spoof localized plasmons from vortex beams [112].

This dissertation introduces a measurement scheme, which is capable of providing absolute space-time field characterization of near-infrared and visible waveforms in a simple and compact imaging setup. The laser source utilized to generate phase-stable few- and sub-cycle light pulses is based on a new hybrid BBO-based OPCPA configuration. The imaging apparatus incorporates basic principles of high-frequency time-domain electro-optic sampling and a simple imaging system to spatially resolve the interaction of two pulses in a nonlinear crystal with second-order nonlinear susceptibility. The upconversion of a broadband electric field under investigation into a narrowband frequency range is especially beneficial to the imaging system. First, chromatic aberrations become negligibly small, allowing for the implementation of experiments with simultaneously high temporal and spatial resolution. Second, momentum conservation during sum-frequency generation leads to a significant reduction of the required numerical aperture.

The spectral limits of the imaging method are analogous to conventional time-domain electro-optic sampling. The main drawback of the imaging technique is poor signal-to-noise ratio as the extracted signal is coupled to the contrast of images rather than balanced photocurrents, and cannot make use of a lock-in amplifier. New optical instruments to

increase signal-to-noise ratio of the system are presented in the thesis. A combination of a thin-film polarizer with a band-pass filter placed after the electro-optic crystal facilitates enhanced contrast of the images through the careful manipulation of the amplitude of the local oscillator. Furthermore, the ability to control the test waveform using the AOPDF allows for subtraction of images with the opposite carrier envelope phase, additionally eliminating mechanical noise of the system.

For the first time, spatially resolved few- and sub-cycle light fields are shown in the near-infrared and visible. Thorough characterization excludes implicit assumptions about the field dependence on the spatial coordinates, making theory a more reliable tool to describe the experimental outcome and explore new theoretical results. Spatio-temporal couplings, which prevent the decomposition of a laser field into spatial and temporal parts, can be detected using either direct spatio-temporal field or conversion to the spatio-spectral domain via Fourier transform. Since all such couplings eventually lead to the peak power reduction, they are highly undesirable in ultrafast and attosecond physics. The presented imaging system is able to become a simple method to reveal spatio-temporal distortions.

Standard amplification schemes often yield a formation of spatio-temporal distortions of the amplified beams: the presence of spatial chirp after the OPCPA can also be the case [148]. Deeper insight into the light synthesis process, including the spatio-temporal coherent recombination of individual channels, is expected to improve the procedure and attain transform-limited pulses.

The design and development of the new generation of optical elements based on sub-wave-length-spaced phase shifters may also take advantage of the imaging technique. Electric fields generated by metasurface devices in the far-field can be readily accessed, even if the spatio-temporal evolution is fairly complicated like Bessel beam or a combination of different fields. Moreover, the form of the light in any position of the propagation direction can be determined from a single measurement by means of simple Fourier optics. This is particularly profitable when a meta-lens induces chromatic aberration to the transmitted light: a focus location for each incident frequency component on the optical axis can be precisely identified. In this way, the plane of the metasurface interface itself is directly accessible, allowing for the recalculation of the output wavefront and peak performance.

Near-field microscopy is probably the most promising application of the imaging method. The near-field features can be detected in the wide-field geometry, providing a universal and reliable platform for real-time measurements of microscopic dynamic systems such as optically-active plasmonic and photonic devices or biological samples. Accordingly, field enhancement locally induced by an aggregation of spherical microparticles is captured with sub-wavelength spatial resolution. Spectral analysis of the resonant spots enables a determination of the exciting wavelength. The image contrast would be even more increased in case of a narrow plasmonic resonance.

Many more intriguing studies that take advantage of the complete spatio-temporal field characterization hold the potential to be implemented. In particular, it relates to the spatio-temporal reconstruction of the underlying dynamics of light-matter interaction with beams carrying spin or orbital angular momentum. Attosecond spectroscopic toolbox can be directly applied to probe spatially inhomogenoius samples and reveal energy transfer

dynamics. Furthermore, the near-field detection can be straitforwardly extended to the visible spectral region, where a variety of plasmonic targets can be studied. On the other hand, complex biological structures can be investigated in the molecular fingerprint region, where electro-optic sampling successfully operates [19]. The electro-optic imaging modality can be potentially adapted to single-shot measurements [190]. In most experimental cases, time-domain electro-optic sampling and its unique properties to access evolution of the time-varying field component can be easily transferred to the spatial dimensions, providing innovative and immense benefits to applications of the time-resolved microscopy [191,192].

Appendix A

List of Author's Publications

Publications related to this thesis:

- **M. Mamaikin**, Y.-L. Li, E. Ridente, W. T. Chen, J.-S. Park, A. Y. Zhu, F. Capasso, M. Weidman, M. Schultze, F. Krausz, and N. Karpowicz. "Electric-field-resolved near infrared microscopy", submitted.
  The author built the experimental setup, performed the measurements and analyzed the data together with N.K. and Y.-L. L., and prepared the manuscript together with N.K.

- **M. Mamaikin**, E. Ridente, Y.-L. Li, M. Weidman, F. Krausz, and N. Karpowicz. "Contrast enhancement in near-infrared electro-optic imaging", in preparation.
  The author built the experimental setup, performed the measurements, analyzed the data, and prepared the manuscript together with N.K.

- E. Ridente, M. Weidman, **M. Mamaikin**, C. Jakubeit, F. Krausz, and Nicholas Karpowicz. "Hybrid phase-matching for optical parametric amplification of few-cycle infrared pulses", Optica, accepted.
  The author assisted in building the laser system and analyzing the data, revised and discussed the manuscript.

Other publications:

- Sergey V. Sazonov, **Mikhail S. Mamaikin**, Maria V. Komissarova, and Irina G. Zakharova, "Planar light bullets under conditions of second-harmonic generation", Physical Review E **96**, 022208 (2017).

- S.V. Sazonov, **M.S. Mamaikin**, I.G. Zakharova, and M.V. Komissarova, "Planar spatiotemporal solitons in a quadratic nonlinear medium", Physics of Wave Phenomena **25**, 83–89 (2017).

- **Mikhail S. Mamaikin**, Maria V. Komissarova, and Irina G. Zakharova, "Propagation of light bullets in media with quadratic nonlinearity", Proceedings of the International Conference DAYS on DIFFRACTION, IEEE Conference Publications, 304–308 (2016).

Appendix B

Data Archiving

The experimental raw data, evaluation files, data processing scripts, and original figures can be found on the Data Archive Server of the Laboratory for Attosecond Physics at the Max Planck Institute of Quantum Optics: `//AFS/ipp-garching.mpg.de/mpq/lap/publication_archive`. All the figures in this thesis are organised in separate folders following the order of the chapters.

Each dedicated folder contains figures in .pdf format, raw data and Matlab scripts if needed. The auxiliary set of scripts required for data analysis is located in the individual folder. The table below gives an overview of the figures.

Figure 1.1	schematic plot (.pdf) and generating script (.m)
Figure 1.2	schematic plot (.pdf)
Figure 1.3	schematic plot (.pdf)
Figure 1.4	schematic plot (.pdf) and generating script (.m)
Figure 1.5	schematic plot (.pdf)
Figure 1.6	schematic plot (.pdf) and generating script (.m), [48]
Figure 1.7	schematic plot (.pdf)
Figure 1.8	schematic plot (.pdf)
Figure 1.9	schematic plot (.pdf)
Figure 1.10	schematic plot (.pdf)
Figure 1.11	schematic plot (.pdf), reprint from N. Yu, et al., [116]
Figure 1.12	schematic plot (.pdf), reprint from N. Yu, et al., [116]
Figure 2.1	schematic plot (.pdf)
Figure 2.2	schematic plot (.pdf)
Figure 2.3	schematic plot (.pdf), generating script (.m), and raw data.
Figure 2.4	schematic plot (.pdf)
Figure 2.5	schematic plot (.pdf)
Figure 2.6	schematic plot (.pdf), generating script (.m), and raw data.
Figure 2.7	schematic plot (.pdf), generating script (.m), and raw data.

Figure 3.1   schematic plot (.pdf), generating script (.m), and raw data.
Figure 3.2   schematic plot (.pdf), generating script (.m), and raw data.
Figure 3.3   schematic plot (.pdf), generating script (.m), and raw data.
Figure 3.4   schematic plot (.pdf), generating script (.m), and raw data.
Figure 3.5   schematic plot (.pdf), generating script (.m), and raw data.
Figure 3.6   schematic plot (.pdf), generating script (.m), and raw data.
Figure 3.7   schematic plot (.pdf), generating script (.m), and raw data.
Figure 3.8   schematic plot (.pdf), generating script (.m), and raw data.
Figure 3.9   schematic plot (.pdf), generating script (.m), and raw data.

Figure 4.1   schematic plot (.pdf)
Figure 4.2   schematic plot (.pdf)
Figure 4.3   schematic plot (.pdf), generating script (.m), and raw data.
Figure 4.4   schematic plot (.pdf), generating script (.m), and raw data.
Figure 4.5   schematic plot (.pdf), generating script (.m), and raw data.
Figure 4.6   schematic plot (.pdf), generating script (.m), and raw data.
Figure 4.7   schematic plot (.pdf), generating script (.m), and raw data.
Figure 4.8   schematic plot (.pdf), generating script (.m), and raw data.

Figure 5.1   schematic plot (.pdf)
Figure 5.2   schematic plot (.pdf), generating script (.m), and raw data.
Figure 5.3   schematic plot (.pdf), generating script (.m), and raw data.
Figure 5.4   schematic plot (.pdf), generating script (.m), and raw data.

Bibliography

[1] P. E. Batson, N. Dellby, and O. L. Krivanek. Sub-ångstrom resolution using aberration corrected electron optics. *Nature*, 418(6898):617–620, 2002.

[2] G. Binnig and H. Rohrer. Scanning tunneling microscopy. *IBM Journal of Research and Development*, 30(4):355–369, 1986.

[3] Stefan W. Hell and Jan Wichmann. Breaking the diffraction resolution limit by stimulated emission: stimulated-emission-depletion fluorescence microscopy. *Opt. Lett.*, 19(11):780–782, Jun 1994.

[4] Eric Betzig, George H. Patterson, Rachid Sougrat, O. Wolf Lindwasser, Scott Olenych, Juan S. Bonifacino, Michael W. Davidson, Jennifer Lippincott-Schwartz, and Harald F. Hess. Imaging intracellular fluorescent proteins at nanometer resolution. *Science*, 313(5793):1642–1645, 2006.

[5] John M. Guerra. Super-resolution through illumination by diffraction-born evanescent waves. *Applied Physics Letters*, 66(26):3555–3557, 1995.

[6] A. Sommer, E. M. Bothschafter, S. A. Sato, C. Jakubeit, T. Latka, O. Razskazovskaya, H. Fattahi, M. Jobst, W. Schweinberger, V. Shirvanyan, V. S. Yakovlev, R. Kienberger, K. Yabana, N. Karpowicz, M. Schultze, and F. Krausz. Attosecond nonlinear polarization and light–matter energy transfer in solids. *Nature*, 534(7605):86–90, 2016.

[7] Ronald Ulbricht, Euan Hendry, Jie Shan, Tony F. Heinz, and Mischa Bonn. Carrier dynamics in semiconductors studied with time-resolved terahertz spectroscopy. *Rev. Mod. Phys.*, 83:543–586, Jun 2011.

[8] A. L. Cavalieri, N. Müller, Th. Uphues, V. S. Yakovlev, A. Baltuška, B. Horvath, B. Schmidt, L. Blümel, R. Holzwarth, S. Hendel, M. Drescher, U. Kleineberg, P. M. Echenique, R. Kienberger, F. Krausz, and U. Heinzmann. Attosecond spectroscopy in condensed matter. *Nature*, 449(7165):1029–1032, 2007.

[9] R. Kienberger, E. Goulielmakis, M. Uiberacker, A. Baltuska, V. Yakovlev, F. Bammer, A. Scrinzi, Th. Westerwalbesloh, U. Kleineberg, U. Heinzmann, M. Drescher, and F. Krausz. Atomic transient recorder. *Nature*, 427(6977):817–821, 2004.

[10] Sebastian Thunich, Claudia Ruppert, Alexander W. Holleitner, and Markus Betz. Field-resolved characterization of femtosecond electromagnetic pulses with 400 THz bandwidth. *Opt. Lett.*, 36(10):1791–1793, May 2011.

[11] E. Goulielmakis, M. Uiberacker, R. Kienberger, A. Baltuska, V. Yakovlev, A. Scrinzi, Th. Westerwalbesloh, U. Kleineberg, U. Heinzmann, M. Drescher, and F. Krausz. Direct measurement of light waves. *Science*, 305(5688):1267–1269, 2004.

[12] Seung Beom Park, Kyungseung Kim, Wosik Cho, Sung In Hwang, Igor Ivanov, Chang Hee Nam, and Kyung Taec Kim. Direct sampling of a light wave in air. *Optica*, 5(4):402–408, Apr 2018.

[13] Shawn Sederberg, Dmitry Zimin, Sabine Keiber, Florian Siegrist, Michael S. Wismer, Vladislav S. Yakovlev, Isabella Floss, Christoph Lemell, Joachim Burgdörfer, Martin Schultze, Ferenc Krausz, and Nicholas Karpowicz. Attosecond optoelectronic field measurement in solids. *Nature Communications*, 11(1):430, 2020.

[14] Q. Wu and X.-C. Zhang. Free-space electro-optic sampling of terahertz beams. *Applied Physics Letters*, 67(24):3523–3525, 1995.

[15] J. A. Valdmanis, G. Mourou, and C. W. Gabel. Picosecond electro-optic sampling system. *Applied Physics Letters*, 41(3):211–212, 1982.

[16] Alexander Sell, Rüdiger Scheu, Alfred Leitenstorfer, and Rupert Huber. Field-resolved detection of phase-locked infrared transients from a compact Er:fiber system tunable between 55 and 107 THz. *Applied Physics Letters*, 93(25):251107, 2008.

[17] Sabine Keiber, Shawn Sederberg, Alexander Schwarz, Michael Trubetskov, Volodymyr Pervak, Ferenc Krausz, and Nicholas Karpowicz. Electro-optic sampling of near-infrared waveforms. *Nature Photonics*, 10(3):159–162, 2016.

[18] O. Razskazovskaya, E. Ridente, and et al. in preparation.

[19] Ioachim Pupeza, Marinus Huber, Michael Trubetskov, Wolfgang Schweinberger, Syed A. Hussain, Christina Hofer, Kilian Fritsch, Markus Poetzlberger, Lenard Vamos, Ernst Fill, Tatiana Amotchkina, Kosmas V. Kepesidis, Alexander Apolonski, Nicholas Karpowicz, Vladimir Pervak, Oleg Pronin, Frank Fleischmann, Abdallah Azzeer, Mihaela Žigman, and Ferenc Krausz. Field-resolved infrared spectroscopy of biological systems. *Nature*, 577(7788):52–59, 2020.

[20] M. Eisele, T. L. Cocker, M. A. Huber, M. Plankl, L. Viti, D. Ercolani, L. Sorba, M. S. Vitiello, and R. Huber. Ultrafast multi-terahertz nano-spectroscopy with sub-cycle temporal resolution. *Nature Photonics*, 8(11):841–845, 2014.

[21] Tyler L. Cocker, Dominik Peller, Ping Yu, Jascha Repp, and Rupert Huber. Tracking the ultrafast motion of a single molecule by femtosecond orbital imaging. *Nature*, 539(7628):263–267, 2016.

[22] Jean-Claude Diels and Wolfgang Rudolph. *Ultrashort Laser Pulse Phenomena (Second Edition)*. Academic Press, Burlington, 2006.

[23] Andrew M. Weiner. *Ultrafast Optics*. John Wiley & Sons, 2009.

[24] Claude Rulliere. *Femtosecond Laser Pulses*. Springer-Verlag New York, 2005.

[25] R. W. Boyd. *Nonlinear Optics*. Academic Press,, 2008.

[26] A.E. Siegman. *Lasers*. University Science Books, 1986.

[27] Rick Trebino and Erik Zeek. *Frequency-Resolved Optical Gating: The Measurement of Ultrashort Laser Pulses*. Springer US, Boston, MA, 2000.

[28] Bahaa E. A. Saleh and Malvin Carl Teich. *Fundamentals of Photonics*. John Wiley & Sons, 1991.

[29] David S Simon. *A Guided Tour of Light Beams*. Morgan & Claypool Publishers, 2016.

[30] D McGloin and K Dholakia. Bessel beams: Diffraction in a new light. *Contemporary Physics*, 46(1):15–28, 2005.

[31] K. H. Yang, P. L. Richards, and Y. R. Shen. Generation of far-infrared radiation by picosecond light pulses in LiNbO3. *Applied Physics Letters*, 19(9):320–323, 1971.

[32] J. A. Fülöp, L. Pálfalvi, G. Almási, and J. Hebling. Design of high-energy terahertz sources based on optical rectification. *Opt. Express*, 18(12):12311–12327, Jun 2010.

[33] J. A. Armstrong, N. Bloembergen, J. Ducuing, and P. S. Pershan. Interactions between light waves in a nonlinear dielectric. *Phys. Rev.*, 127:1918–1939, Sep 1962.

[34] M. Yamada, N. Nada, M. Saitoh, and K. Watanabe. First-order quasi-phase matched LiNbO3 waveguide periodically poled by applying an external field for efficient blue second-harmonic generation. *Applied Physics Letters*, 62(5):435–436, 1993.

[35] F. DeMartini, C. H. Townes, T. K. Gustafson, and P. L. Kelley. Self-steepening of light pulses. *Phys. Rev.*, 164:312–323, Dec 1967.

[36] Yuri Kivshar and Govind Agrawal. *Optical Solitons: From Fibers to Photonic Crystals*. Academic Press, 2003.

[37] Sergey V. Sazonov, Mikhail S. Mamaikin, Maria V. Komissarova, and Irina G. Zakharova. Planar light bullets under conditions of second-harmonic generation. *Phys. Rev. E*, 96:022208, Aug 2017.

[38] Robert McLeod, Kelvin Wagner, and Steve Blair. (3+1)-dimensional optical soliton dragging logic. *Phys. Rev. A*, 52:3254–3278, Oct 1995.

[39] G. D. McDonald, C. C. N. Kuhn, K. S. Hardman, S. Bennetts, P. J. Everitt, P. A. Altin, J. E. Debs, J. D. Close, and N. P. Robins. Bright solitonic matter-wave interferometer. *Phys. Rev. Lett.*, 113:013002, Jul 2014.

[40] S. A. Akhmanov, A. I. Kovrigin, A. S. Piskarskas, V. V. Fadeev, and Khokhlov R. V. Observation of parametric amplification in the optical range. *JETP Letters*, 2(7):191, 1965.

[41] J. A. Giordmaine and Robert C. Miller. Tunable coherent parametric oscillation in LiNbO3 at optical frequencies. *Phys. Rev. Lett.*, 14:973–976, Jun 1965.

[42] Donna Strickland and Gerard Mourou. Compression of amplified chirped optical pulses. *Optics Communications*, 56(3):219 – 221, 1985.

[43] A. Dubietis, G. Jonušauskas, and A. Piskarskas. Powerful femtosecond pulse generation by chirped and stretched pulse parametric amplification in BBO crystal. *Optics Communications*, 88(4):437 – 440, 1992.

[44] I.N. Ross, P. Matousek, M. Towrie, A.J. Langley, and J.L. Collier. The prospects for ultrashort pulse duration and ultrahigh intensity using optical parametric chirped pulse amplifiers. *Optics Communications*, 144(1):125 – 133, 1997.

[45] R. Butkus, R. Danielius, A. Dubietis, A. Piskarskas, and A. Stabinis. Progress in chirped pulse optical parametric amplifiers. *Applied Physics B*, 79(6):693–700, 2004.

[46] Selcuk Akturk, Xun Gu, Erik Zeek, and Rick Trebino. Pulse-front tilt caused by spatial and temporal chirp. *Opt. Express*, 12(19):4399–4410, Sep 2004.

[47] Selcuk Akturk, Xun Gu, Pamela Bowlan, and Rick Trebino. Spatio-temporal couplings in ultrashort laser pulses. *Journal of Optics*, 12(9):093001, aug 2010.

[48] Michelle Rhodes, Zhe Guang, Jerrold Pease, and Rick Trebino. Visualizing spatiotemporal pulse propagation: first-order spatiotemporal couplings in laser pulses. *Appl. Opt.*, 56(11):3024–3034, Apr 2017.

[49] Selcuk Akturk, Xun Gu, Pablo Gabolde, and Rick Trebino. The general theory of first-order spatio-temporal distortions of gaussian pulses and beams. *Opt. Express*, 13(21):8642–8661, Oct 2005.

[50] Martin Schultze, Krupa Ramasesha, C.D. Pemmaraju, S.A. Sato, D. Whitmore, A. Gandman, James S. Prell, L. J. Borja, D. Prendergast, K. Yabana, Daniel M. Neumark, and Stephen R. Leone. Attosecond band-gap dynamics in silicon. *Science*, 346(6215):1348–1352, 2014.

[51] M. Lucchini, S. A. Sato, A. Ludwig, J. Herrmann, M. Volkov, L. Kasmi, Y. Shinohara, K. Yabana, L. Gallmann, and U. Keller. Attosecond dynamical Franz-Keldysh effect in polycrystalline diamond. *Science*, 353(6302):916–919, 2016.

[52] Rick Trebino, Kenneth W. DeLong, David N. Fittinghoff, John N. Sweetser, Marco A. Krumbügel, Bruce A. Richman, and Daniel J. Kane. Measuring ultrashort laser pulses in the time-frequency domain using frequency-resolved optical gating. *Review of Scientific Instruments*, 68(9):3277–3295, 1997.

[53] Daniel J. Kane and Rick Trebino. Single-shot measurement of the intensity and phase of an arbitrary ultrashort pulse by using frequency-resolved optical gating. *Opt. Lett.*, 18(10):823–825, May 1993.

[54] Yutaka Nomura, Hideto Shirai, and Takao Fuji. Frequency-resolved optical gating capable of carrier-envelope phase determination. *Nature Communications*, 4(1):2820, 2013.

[55] J. Itatani, F. Quéré, G. L. Yudin, M. Yu. Ivanov, F. Krausz, and P. B. Corkum. Attosecond streak camera. *Phys. Rev. Lett.*, 88:173903, 2002.

[56] N. H. Burnett, H. A. Baldis, M. C. Richardson, and G. D. Enright. Harmonic generation in CO2 laser target interaction. *Applied Physics Letters*, 31(3):172–174, 1977.

[57] A. Flettner, T. Pfeifer, D. Walter, C. Winterfeldt, C. Spielmann, and G. Gerber. High-harmonic generation and plasma radiation from water microdroplets. *Applied Physics B*, 77(8):747–751, Dec 2003.

[58] P. B. Corkum. Plasma perspective on strong field multiphoton ionization. *Phys. Rev. Lett.*, 71:1994–1997, Sep 1993.

[59] H. Vincenti and F. Quéré. Attosecond lighthouses: How to use spatiotemporally coupled light fields to generate isolated attosecond pulses. *Phys. Rev. Lett.*, 108:113904, Mar 2012.

[60] G. Sansone, E. Benedetti, F. Calegari, C. Vozzi, L. Avaldi, R. Flammini, L. Poletto, P. Villoresi, C. Altucci, R. Velotta, S. Stagira, S. De Silvestri, and M. Nisoli. Isolated single-cycle attosecond pulses. *Science*, 314(5798):443–446, 2006.

[61] Mark J. Abel, Thomas Pfeifer, Phillip M. Nagel, Willem Boutu, M. Justine Bell, Colby P. Steiner, Daniel M. Neumark, and Stephen R. Leone. Isolated attosecond pulses from ionization gating of high-harmonic emission. *Chemical Physics*, 366(1):9 – 14, 2009. Attosecond Molecular Dynamics.

[62] J. Gagnon and V. S. Yakovlev. The direct evaluation of attosecond chirp from a streaking measurement. *Applied Physics B*, 103(2):303–309, 2011.

[63] Thomas Gaumnitz, Arohi Jain, Yoann Pertot, Martin Huppert, Inga Jordan, Fernando Ardana-Lamas, and Hans Jakob Wörner. Streaking of 43-attosecond soft-X-ray pulses generated by a passively CEP-stable mid-infrared driver. *Opt. Express*, 25(22):27506–27518, Oct 2017.

[64] Steve Gilbertson, Ximao Feng, Sabih Khan, Michael Chini, He Wang, Hiroki Mashiko, and Zenghu Chang. Direct measurement of an electric field in femtosecond Bessel-Gaussian beams. *Opt. Lett.*, 34(16):2390–2392, Aug 2009.

[65] M. Pastorino. *Microwave Imaging.* John Wiley & Sons, 2010.

[66] H. Hamster, A. Sullivan, S. Gordon, W. White, and R. W. Falcone. Subpicosecond, electromagnetic pulses from intense laser-plasma interaction. *Phys. Rev. Lett.*, 71:2725–2728, Oct 1993.

[67] D. J. Cook and R. M. Hochstrasser. Intense terahertz pulses by four-wave rectification in air. *Opt. Lett.*, 25(16):1210–1212, Aug 2000.

[68] Fabrizio Buccheri and Xi-Cheng Zhang. Terahertz emission from laser-induced microplasma in ambient air. *Optica*, 2(4):366–369, Apr 2015.

[69] Paul C. M. Planken, Han-Kwang Nienhuys, Huib J. Bakker, and Tom Wenckebach. Measurement and calculation of the orientation dependence of terahertz pulse detection in ZnTe. *J. Opt. Soc. Am. B*, 18(3):313–317, Mar 2001.

[70] Nick C. J. van der Valk, Tom Wenckebach, and Paul C. M. Planken. Full mathematical description of electro-optic detection in optically isotropic crystals. *J. Opt. Soc. Am. B*, 21(3):622–631, Mar 2004.

[71] C. Winnewisser, P. Uhd Jepsen, M. Schall, V. Schyja, and H. Helm. Electro-optic detection of THz radiation in LiTaO3, LiNbO3 and ZnTe. *Applied Physics Letters*, 70(23):3069–3071, 1997.

[72] R. Huber, F. Tauser, A. Brodschelm, M. Bichler, G. Abstreiter, and A. Leitenstorfer. How many-particle interactions develop after ultrafast excitation of an electron–hole plasma. *Nature*, 414(6861):286–289, 2001.

[73] Alexej Pashkin, Alexander Sell, Tobias Kampfrath, and Rupert Huber. Electric and magnetic terahertz nonlinearities resolved on the sub-cycle scale. *New Journal of Physics*, 15(6):065003, jun 2013.

[74] P. Gaal, W. Kuehn, K. Reimann, M. Woerner, T. Elsaesser, and R. Hey. Internal motions of a quasiparticle governing its ultrafast nonlinear response. *Nature*, 450(7173):1210–1213, 2007.

[75] Josef Kröll, Juraj Darmo, Sukhdeep S. Dhillon, Xavier Marcadet, Michel Calligaro, Carlo Sirtori, and Karl Unterrainer. Phase-resolved measurements of stimulated emission in a laser. *Nature*, 449(7163):698–701, 2007.

[76] Jie Shan, Aniruddha S. Weling, Ernst Knoesel, Ludwig Bartels, Mischa Bonn, Ajay Nahata, Georg A. Reider, and Tony F. Heinz. Single-shot measurement of terahertz electromagnetic pulses by use of electro-optic sampling. *Opt. Lett.*, 25(6):426–428, Mar 2000.

[77] Masahiko Tani, Kazuki Horita, Tetsuya Kinoshita, Christopher T. Que, Elmer Estacio, Kohji Yamamoto, and Michael I. Bakunov. Efficient electro-optic sampling detection of terahertz radiation via Cherenkov phase matching. *Opt. Express*, 19(21):19901–19906, Oct 2011.

[78] E. A. Mashkovich, A. I. Shugurov, S. Ozawa, E. Estacio, M. Tani, and M. I. Bakunov. Noncollinear electro-optic sampling of terahertz waves in a thick GaAs crystal. *IEEE Transactions on Terahertz Science and Technology*, 5(5):732–736, Sep. 2015.

[79] J. A. Riordan, F. G. Sun, Z. G. Lu, and X.-C. Zhang. Free-space transient magneto-optic sampling. *Applied Physics Letters*, 71(11):1452–1454, 1997.

[80] Patrick O'Shea, Mark Kimmel, Xun Gu, and Rick Trebino. Highly simplified device for ultrashort-pulse measurement. *Opt. Lett.*, 26(12):932–934, Jun 2001.

[81] Selcuk Akturk, Mark Kimmel, Patrick O'Shea, and Rick Trebino. Measuring spatial chirp in ultrashort pulses using single-shot frequency-resolved optical gating. *Opt. Express*, 11(1):68–78, Jan 2003.

[82] Selcuk Akturk, Mark Kimmel, Patrick O'Shea, and Rick Trebino. Measuring pulse-front tilt in ultrashort pulses using grenouille. *Opt. Express*, 11(5):491–501, Mar 2003.

[83] Pamela Bowlan, Pablo Gabolde, and Rick Trebino. Directly measuring the spatio-temporal electric field of focusing ultrashort pulses. *Opt. Express*, 15(16):10219–10230, Aug 2007.

[84] Benjamín Alonso, Í nigo J. Sola, Óscar Varela, Juan Hernández-Toro, Cruz Méndez, Julio San Román, Amelle Zaïr, and Luis Roso. Spatiotemporal amplitude-and-phase reconstruction by Fourier-transform of interference spectra of high-complex-beams. *J. Opt. Soc. Am. B*, 27(5):933–940, May 2010.

[85] Pablo Gabolde and Rick Trebino. Single-shot measurement of the full spatio-temporal field of ultrashort pulses with multi-spectral digital holography. *Opt. Express*, 14(23):11460–11467, Nov 2006.

[86] Pablo Gabolde and Rick Trebino. Self-referenced measurement of the complete electric field of ultrashort pulses. *Opt. Express*, 12(19):4423–4429, Sep 2004.

[87] Miguel Miranda, Marija Kotur, Piotr Rudawski, Chen Guo, Anne Harth, Anne L'Huillier, and Cord L. Arnold. Spatiotemporal characterization of ultrashort laser pulses using spatially resolved Fourier transform spectrometry. *Opt. Lett.*, 39(17):5142–5145, Sep 2014.

[88] G. Pariente, V. Gallet, A. Borot, O. Gobert, and F. Quéré. Space–time characterization of ultra-intense femtosecond laser beams. *Nature Photonics*, 10(8):547–553, 2016.

[89] Antonin Borot and Fabien Quéré. Spatio-spectral metrology at focus of ultrashort lasers: a phase-retrieval approach. *Opt. Express*, 26(20):26444–26461, Oct 2018.

[90] Pablo Gabolde and Rick Trebino. Self-referenced measurement of the complete electric field of ultrashort pulses. *Opt. Express*, 12(19):4423–4429, Sep 2004.

[91] F. Bragheri, D. Faccio, F. Bonaretti, A. Lotti, M. Clerici, O. Jedrkiewicz, C. Liberale, S. Henin, L. Tartara, V. Degiorgio, and P. Di Trapani. Complete retrieval of the field of ultrashort optical pulses using the angle-frequency spectrum. *Opt. Lett.*, 33(24):2952–2954, Dec 2008.

[92] Seth L. Cousin, Juan M. Bueno, Nicolas Forget, Dane R. Austin, and J. Biegert. Three-dimensional spatiotemporal pulse characterization with an acousto-optic pulse shaper and a Hartmann–Shack wavefront sensor. *Opt. Lett.*, 37(15):3291–3293, Aug 2012.

[93] Dane R. Austin, Tobias Witting, Sébastien J. Weber, Peng Ye, Thomas Siegel, Paloma Matía-Hernando, Allan S. Johnson, John W.G. Tisch, and Jonathan P. Marangos. Spatio-temporal characterization of intense few-cycle 2 μm pulses. *Opt. Express*, 24(21):24786–24798, Oct 2016.

[94] Olga Razskazovskaya. *Infrared waveform synthesis for applications in attosecond science*. PhD thesis, Ludwig–Maximilians–Universität München, 2017.

[95] Michael Porer, Jean-Michel Ménard, and Rupert Huber. Shot noise reduced terahertz detection via spectrally postfiltered electro-optic sampling. *Opt. Lett.*, 39(8):2435–2438, Apr 2014.

[96] Kyung Taec Kim, Chunmei Zhang, Andrew D. Shiner, Bruno E. Schmidt, François Légaré, D. M. Villeneuve, and P. B. Corkum. Petahertz optical oscilloscope. *Nature Photonics*, 7(12):958–962, 2013.

[97] Z. G. Lu, P. Campbell, and X.-C. Zhang. Free-space electro-optic sampling with a high-repetition-rate regenerative amplified laser. *Applied Physics Letters*, 71(5):593–595, 1997.

[98] Zhiping Jiang, X. G. Xu, and X.-C. Zhang. Improvement of terahertz imaging with a dynamic subtraction technique. *Appl. Opt.*, 39(17):2982–2987, Jun 2000.

[99] Xinke Wang, Ye Cui, Wenfeng Sun, JiaSheng Ye, and Yan Zhang. Terahertz polarization real-time imaging based on balanced electro-optic detection. *J. Opt. Soc. Am. A*, 27(11):2387–2393, Nov 2010.

[100] Xinke Wang, Ye Cui, Wenfeng Sun, JiaSheng Ye, and Yan Zhang. Terahertz real-time imaging with balanced electro-optic detection. *Optics Communications*, 283(23):4626 – 4632, 2010.

[101] Mayuko Takai, Masatoshi Takeda, Manabu Sasaki, Takehiro Tachizaki, Naoya Yasumatsu, and Shinichi Watanabe. Video-rate terahertz electric-field vector imaging. *Applied Physics Letters*, 105(15):151103, 2014.

[102] Q. Wu, T. D. Hewitt, and X.-C. Zhang. Two-dimensional electro-optic imaging of THz beams. *Applied Physics Letters*, 69(8):1026–1028, 1996.

[103] Zhen Wu, Xinke Wang, Wenfeng Sun, Shengfei Feng, Peng Han, Jiasheng Ye, and Yan Zhang. Vector characterization of zero-order terahertz Bessel beams with linear and circular polarizations. *Scientific Reports*, 7(1):13929, 2017.

[104] Jingwen He, Xinke Wang, Dan Hu, Jiasheng Ye, Shengfei Feng, Qiang Kan, and Yan Zhang. Generation and evolution of the terahertz vortex beam. *Opt. Express*, 21(17):20230–20239, Aug 2013.

[105] B. B. Hu and M. C. Nuss. Imaging with terahertz waves. *Opt. Lett.*, 20(16):1716–1718, Aug 1995.

[106] S Hunsche, M Koch, I Brener, and M.C Nuss. THz near-field imaging. *Optics Communications*, 150(1):22 – 26, 1998.

[107] Hou-Tong Chen, Roland Kersting, and Gyu Cheon Cho. Terahertz imaging with nanometer resolution. *Applied Physics Letters*, 83(15):3009–3011, 2003.

[108] Richard M. Koehl, Satoru Adachi, and Keith A. Nelson. Direct visualization of collective wavepacket dynamics. *The Journal of Physical Chemistry A*, 103(49):10260–10267, 12 1999.

[109] F. Blanchard, A. Doi, T. Tanaka, H. Hirori, H. Tanaka, Y. Kadoya, and K. Tanaka. Real-time terahertz near-field microscope. *Opt. Express*, 19(9):8277–8284, Apr 2011.

[110] F. Blanchard, K. Sumida, C. Wolpert, M. Tsotsalas, T. Tanaka, A. Doi, S. Kitagawa, D. G. Cooke, S. Furukawa, and K. Tanaka. Terahertz phase contrast imaging of sorption kinetics in porous coordination polymer nanocrystals using differential optical resonator. *Opt. Express*, 22(9):11061–11069, May 2014.

[111] François Blanchard, Xin Chai, Tomoko Tanaka, Takashi Arikawa, Tsuneyuki Ozaki, Roberto Morandotti, and Koichiro Tanaka. Terahertz microscopy assisted by semiconductor nonlinearities. *Opt. Lett.*, 43(20):4997–5000, Oct 2018.

[112] Takashi Arikawa, Tomoki Hiraoka, Shohei Morimoto, Francois Blanchard, Shuntaro Tani, Tomoko Tanaka, Kyosuke Sakai, Hiroki Kitajima, Keiji Sasaki, and Koichiro Tanaka. Selective excitation of multipolar spoof plasmons using orbital angular momentum of light, 2019.

[113] François Blanchard and Koichiro Tanaka. Improving time and space resolution in electro-optic sampling for near-field terahertz imaging. *Opt. Lett.*, 41(20):4645–4648, Oct 2016.

[114] Bradley Ferguson and Xi-Cheng Zhang. Materials for terahertz science and technology. *Nature Materials*, 1(1):26–33, 2002.

[115] Nanfang Yu, Patrice Genevet, Mikhail A. Kats, Francesco Aieta, Jean-Philippe Tetienne, Federico Capasso, and Zeno Gaburro. Light propagation with phase discontinuities: Generalized laws of reflection and refraction. *Science*, 334(6054):333–337, 2011.

[116] N. Yu, P. Genevet, F. Aieta, M. A. Kats, R. Blanchard, G. Aoust, J. Tetienne, Z. Gaburro, and F. Capasso. Flat optics: Controlling wavefronts with optical antenna metasurfaces. *IEEE Journal of Selected Topics in Quantum Electronics*, 19(3):4700423–4700423, May 2013.

[117] Francesco Aieta, Patrice Genevet, Nanfang Yu, Mikhail A. Kats, Zeno Gaburro, and Federico Capasso. Out-of-plane reflection and refraction of light by anisotropic optical antenna metasurfaces with phase discontinuities. *Nano Letters*, 12(3):1702–1706, 03 2012.

[118] Lukas Novotny and Niek van Hulst. Antennas for light. *Nature Photonics*, 5(2):83–90, 2011.

[119] Jonathan A. Fan, Chihhui Wu, Kui Bao, Jiming Bao, Rizia Bardhan, Naomi J. Halas, Vinothan N. Manoharan, Peter Nordlander, Gennady Shvets, and Federico Capasso. Self-assembled plasmonic nanoparticle clusters. *Science*, 328(5982):1135–1138, 2010.

[120] Hideki T. Miyazaki and Yoichi Kurokawa. Controlled plasmon resonance in closed metal/insulator/metal nanocavities. *Applied Physics Letters*, 89(21):211126, 2006.

[121] Yuanmu Yang, Wenyi Wang, Parikshit Moitra, Ivan I. Kravchenko, Dayrl P. Briggs, and Jason Valentine. Dielectric meta-reflectarray for broadband linear polarization conversion and optical vortex generation. *Nano Letters*, 14(3):1394–1399, 03 2014.

[122] Boris Desiatov, Noa Mazurski, Yeshaiahu Fainman, and Uriel Levy. Polarization selective beam shaping using nanoscale dielectric metasurfaces. *Opt. Express*, 23(17):22611–22618, Aug 2015.

[123] Yao-Wei Huang, Wei Ting Chen, Wei-Yi Tsai, Pin Chieh Wu, Chih-Ming Wang, Greg Sun, and Din Ping Tsai. Aluminum plasmonic multicolor meta-hologram. *Nano Letters*, 15(5):3122–3127, 05 2015.

[124] Avi Niv, Gabriel Biener, Vladimir Kleiner, and Erez Hasman. Spiral phase elements obtained by use of discrete space-variant subwavelength gratings. *Optics Communications*, 251(4):306 – 314, 2005.

[125] Xiaohu Zhang, Jinjin Jin, Yanqin Wang, Mingbo Pu, Xiong Li, Zeyu Zhao, Ping Gao, Changtao Wang, and Xiangang Luo. Metasurface-based broadband hologram with high tolerance to fabrication errors. *Scientific Reports*, 6(1):19856, 2016.

[126] Francesco Aieta, Patrice Genevet, Mikhail A. Kats, Nanfang Yu, Romain Blanchard, Zeno Gaburro, and Federico Capasso. Aberration-free ultrathin flat lenses and axicons at telecom wavelengths based on plasmonic metasurfaces. *Nano Letters*, 12(9):4932–4936, 09 2012.

[127] Yunpei Deng, Alexander Schwarz, Hanieh Fattahi, Moritz Ueffing, Xun Gu, Marcus Ossiander, Thomas Metzger, Volodymyr Pervak, Hideki Ishizuki, Takunori Taira, Takayoshi Kobayashi, Gilad Marcus, Ferenc Krausz, Reinhard Kienberger, and Nicholas Karpowicz. Carrier-envelope-phase-stable, 1.2 mJ, 1.5 cycle laser pulses at 2.1 µm. *Opt. Lett.*, 37(23):4973–4975, Dec 2012.

[128] Clemens Jacubeit. *High Harmonic Generation using 2 µm OPCPA*. PhD thesis, Ludwig–Maximilians–Universität München, 2019.

[129] Enrico Ridente, Matthew Weidman, Mikhail Mamaikin, Clemens Jakubeit, Ferenc Krausz, and Nicholas Karpowicz. Hybrid phase-matching for optical parametric amplification of few-cycle infrared pulses. *Optica*. accepted.

[130] I. Pupeza, D. Sánchez, J. Zhang, N. Lilienfein, M. Seidel, N. Karpowicz, T. Paasch-Colberg, I. Znakovskaya, M. Pescher, W. Schweinberger, V. Pervak, E. Fill, O. Pronin, Z. Wei, F. Krausz, A. Apolonski, and J. Biegert. High-power sub-two-cycle mid-infrared pulses at 100 MHz repetition rate. *Nature Photonics*, 9(11):721–724, 2015.

[131] Hanieh Fattahi, Alexander Schwarz, Sabine Keiber, and Nicholas Karpowicz. Efficient, octave-spanning difference-frequency generation using few-cycle pulses in simple collinear geometry. *Opt. Lett.*, 38(20):4216–4219, Oct 2013.

[132] Andrius Baltuška, Takao Fuji, and Takayoshi Kobayashi. Controlling the carrier-envelope phase of ultrashort light pulses with optical parametric amplifiers. *Phys. Rev. Lett.*, 88:133901, Mar 2002.

[133] Thomas Metzger, Alexander Schwarz, Catherine Yuriko Teisset, Dirk Sutter, Alexander Killi, Reinhard Kienberger, and Ferenc Krausz. High-repetition-rate picosecond pump laser based on a Yb:YAG disk amplifier for optical parametric amplification. *Opt. Lett.*, 34(14):2123–2125, Jul 2009.

[134] Hanieh Fattahi, Alexander Schwarz, Xiao Tao Geng, Sabine Keiber, Dong Eon Kim, Ferenc Krausz, and Nicholas Karpowicz. Decoupling chaotic amplification and nonlinear phase in high-energy thin-disk amplifiers for stable OPCPA pumping. *Opt. Express*, 22(25):31440–31447, Dec 2014.

[135] Alexander Schwarz, Moritz Ueffing, Yunpei Deng, Xun Gu, Hanieh Fattahi, Thomas Metzger, Marcus Ossiander, Ferenc Krausz, and Reinhard Kienberger. Active stabilization for optically synchronized optical parametric chirped pulse amplification. *Opt. Express*, 20(5):5557–5565, Feb 2012.

[136] Alexander Schwarz. *Few-cycle phase-stable infrared OPCPA.* PhD thesis, Ludwig–Maximilians–Universität München, 2014.

[137] H. A Macleod. *Thin-film optical filters.* Institute of Physics Publishing, London, 1986.

[138] Saima Ahmed, Janne Savolainen, and Peter Hamm. Detectivity enhancement in thz electrooptical sampling. *Review of Scientific Instruments*, 85(1):013114, 2014.

[139] M. Hohenleutner, F. Langer, O. Schubert, M. Knorr, U. Huttner, S. W. Koch, M. Kira, and R. Huber. Real-time observation of interfering crystal electrons in high-harmonic generation. *Nature*, 523(7562):572–575, 2015.

[140] W. Kuehn, P. Gaal, K. Reimann, M. Woerner, T. Elsaesser, and R. Hey. Terahertz-induced interband tunneling of electrons in GaAs. *Phys. Rev. B*, 82:075204, Aug 2010.

[141] Selcuk Akturk, Xun Gu, Pamela Bowlan, and Rick Trebino. Spatio-temporal couplings in ultrashort laser pulses. *Journal of Optics*, 12(9):093001, 2010.

[142] Achut Giree, Mark Mero, Gunnar Arisholm, Marc J. J. Vrakking, and Federico J. Furch. Numerical study of spatiotemporal distortions in noncollinear optical parametric chirped-pulse amplifiers. *Opt. Express*, 25(4):3104–3121, 2017.

[143] Z Bouchal, J Wagner, and M Chlup. Self-reconstruction of a distorted nondiffracting beam. *Optics Communications*, 151(4):207 – 211, 1998.

[144] Jun Chen, Jack Ng, Zhifang Lin, and C. T. Chan. Optical pulling force. *Nature Photonics*, 5(9):531–534, 2011.

[145] Jian Wang. Advances in communications using optical vortices. *Photon. Res.*, 4(5):B14–B28, Oct 2016.

[146] D. Cojoc, V. Garbin, E. Ferrari, L. Businaro, F. Romanato, and E. Di Fabrizio. Laser trapping and micro-manipulation using optical vortices. *Microelectronic Engineering*, 78-79:125 – 131, 2005. Proceedings of the 30th International Conference on Micro- and Nano-Engineering.

[147] Akira Shirakawa, Isao Sakane, and Takayoshi Kobayashi. Pulse-front-matched optical parametric amplification for sub-10-fs pulse generation tunable in the visible and near infrared. *Opt. Lett.*, 23(16):1292–1294, Aug 1998.

[148] Audrius Zaukevičius, Vytautas Jukna, Roman Antipenkov, Vilija Martinėnaitė, Arūnas Varanavičius, Algis Petras Piskarskas, and Gintaras Valiulis. Spatial chirp and angular dispersion dynamics in femtosecond noncollinear OPCPA. In *Lasers, Sources, and Related Photonic Devices*, page AM4A.28. Optical Society of America, 2012.

[149] Alexander Kessel. *Generation and parametric amplification of few-cycle light pulses at relativistic intensities*. PhD thesis, Ludwig–Maximilians–Universität München, 2017.

[150] O. Razskazovskaya, F. Krausz, and V. Pervak. Multilayer coatings for femto- and attosecond technology. *Optica*, 4(1):129–138, Jan 2017.

[151] A. Wirth, M. Th. Hassan, I. Grguraš, J. Gagnon, A. Moulet, T. T. Luu, S. Pabst, R. Santra, Z. A. Alahmed, A. M. Azzeer, V. S. Yakovlev, V. Pervak, F. Krausz, and E. Goulielmakis. Synthesized light transients. *Science*, 334(6053):195–200, 2011.

[152] Robert K. Shelton, Long-Sheng Ma, Henry C. Kapteyn, Margaret M. Murnane, John L. Hall, and Jun Ye. Phase-coherent optical pulse synthesis from separate femtosecond lasers. *Science*, 293(5533):1286–1289, 2001.

[153] Günther Krauss, Sebastian Lohss, Tobias Hanke, Alexander Sell, Stefan Eggert, Rupert Huber, and Alfred Leitenstorfer. Synthesis of a single cycle of light with compact erbium-doped fibre technology. *Nature Photonics*, 4(1):33–36, 2010.

[154] Kotaro Okamura and Takayoshi Kobayashi. Octave-spanning carrier-envelope phase stabilized visible pulse with sub-3-fs pulse duration. *Opt. Lett.*, 36(2):226–228, Jan 2011.

[155] Nicholas Fang, Hyesog Lee, Cheng Sun, and Xiang Zhang. Sub-diffraction-limited optical imaging with a silver superlens. *Science*, 308(5721):534–537, 2005.

[156] R. A. Shelby, D. R. Smith, and S. Schultz. Experimental verification of a negative index of refraction. *Science*, 292(5514):77–79, 2001.

[157] D. Schurig, J. J. Mock, B. J. Justice, S. A. Cummer, J. B. Pendry, A. F. Starr, and D. R. Smith. Metamaterial electromagnetic cloak at microwave frequencies. *Science*, 314(5801):977–980, 2006.

[158] M. Mamaikin, Y.-L. Li, E. Ridente, W. T. Chen, J.-S. Park, A. Y. Zhu, F. Capasso, M. Weidman, M. Schultze, F. Krausz, and N. Karpowicz. Electric-field-resolved near infrared microscopy. submitted.

[159] Joon-Suh Park, Shuyan Zhang, Alan She, Wei Ting Chen, Peng Lin, Kerolos M. A. Yousef, Ji-Xin Cheng, and Federico Capasso. All-glass, large metalens at visible wavelength using deep-ultraviolet projection lithography. *Nano Letters*, 19(12):8673–8682, 2019.

[160] Mohammadreza Khorasaninejad, Wei Ting Chen, Robert C. Devlin, Jaewon Oh, Alexander Y. Zhu, and Federico Capasso. Metalenses at visible wavelengths: Diffraction-limited focusing and subwavelength resolution imaging. *Science*, 352(6290):1190–1194, 2016.

[161] Wei Ting Chen, Mohammadreza Khorasaninejad, Alexander Y. Zhu, Jaewon Oh, Robert C. Devlin, Aun Zaidi, and Federico Capasso. Generation of wavelength-independent subwavelength Bessel beams using metasurfaces. *Light: Science & Applications*, 6(5):e16259–e16259, 2017.

[162] Francesco Aieta, Mikhail A. Kats, Patrice Genevet, and Federico Capasso. Multiwavelength achromatic metasurfaces by dispersive phase compensation. *Science*, 347(6228):1342–1345, 2015.

[163] Anders Pors, Michael G. Nielsen, René Lynge Eriksen, and Sergey I. Bozhevolnyi. Broadband focusing flat mirrors based on plasmonic gradient metasurfaces. *Nano Letters*, 13(2):829–834, 2013. PMID: 23343380.

[164] Xingjie Ni, Naresh K. Emani, Alexander V. Kildishev, Alexandra Boltasseva, and Vladimir M. Shalaev. Broadband light bending with plasmonic nanoantennas. *Science*, 335(6067):427–427, 2012.

[165] Dianmin Lin, Pengyu Fan, Erez Hasman, and Mark L. Brongersma. Dielectric gradient metasurface optical elements. *Science*, 345(6194):298–302, 2014.

[166] S. Pancharatnam. Generalized theory of interference and its applications. *Proceedings of the Indian Academy of Sciences - Section A*, 44(6):398–417, 1956.

[167] M.V. Berry. The adiabatic phase and Pancharatnam's phase for polarized light. *Journal of Modern Optics*, 34(11):1401–1407, 1987.

[168] Guoxing Zheng, Holger Mühlenbernd, Mitchell Kenney, Guixin Li, Thomas Zentgraf, and Shuang Zhang. Metasurface holograms reaching 80% efficiency. *Nature Nanotechnology*, 10(4):308–312, 2015.

[169] Lingling Huang, Xianzhong Chen, Holger Mühlenbernd, Guixin Li, Benfeng Bai, Qiaofeng Tan, Guofan Jin, Thomas Zentgraf, and Shuang Zhang. Dispersionless phase discontinuities for controlling light propagation. *Nano Letters*, 12(11):5750–5755, 11 2012.

[170] Ze'ev Bomzon, Gabriel Biener, Vladimir Kleiner, and Erez Hasman. Space-variant Pancharatnam–Berry phase optical elements with computer-generated subwavelength gratings. *Opt. Lett.*, 27(13):1141–1143, Jul 2002.

[171] Ki-Hwan Kim, Kwan-Il Lee, Heung-Ryoul Noh, Jong-An Kim, M. Ohtsu, and Wonho Jhe. Cold atomic beam from an axicon trap. In *International Quantum Electronics Conference*, page QFG8. Optical Society of America, 1998.

[172] O. Ren and R. Birngruber. Axicon: a new laser beam delivery system for corneal surgery. *IEEE Journal of Quantum Electronics*, 26(12):2305–2308, Dec 1990.

[173] Zhihua Ding, Hongwu Ren, Yonghua Zhao, J. Stuart Nelson, and Zhongping Chen. High-resolution optical coherence tomography over a large depth range with an axicon lens. *Opt. Lett.*, 27(4):243–245, Feb 2002.

[174] J Arlt, V Garces-Chavez, W Sibbett, and K Dholakia. Optical micromanipulation using a Bessel light beam. *Optics Communications*, 197(4):239 – 245, 2001.

[175] John H. McLeod. The axicon: A new type of optical element. *J. Opt. Soc. Am.*, 44(8):592–597, Aug 1954.

[176] James Lloyd, Kanglin Wang, Adrian Barkan, and Daniel M Mittleman. Characterization of apparent superluminal effects in the focus of an axicon lens using terahertz time-domain spectroscopy. *Optics Communications*, 219(1):289 – 294, 2003.

[177] W. R. Edmonds. The reflaxicon, a new reflective optical element, and some applications. *Appl. Opt.*, 12(8):1940–1945, Aug 1973.

[178] U. Dürig, D. W. Pohl, and F. Rohner. Near-field optical-scanning microscopy. *Journal of Applied Physics*, 59(10):3318–3327, 1986.

[179] M.A. Paesler and P.J. Moyer. *Near-Field Optics*. Wiley, New-York, 1996.

[180] Yasushi Oshikane, Toshihiko Kataoka, Mitsuru Okuda, Seiji Hara, Haruyuki Inoue, and Motohiro Nakano. Observation of nanostructure by scanning near-field optical microscope with small sphere probe. *Science and Technology of Advanced Materials*, 8(3):181–185, 2007.

[181] B. Knoll and F. Keilmann. Near-field probing of vibrational absorption for chemical microscopy. *Nature*, 399(6732):134–137, 1999.

[182] M. Eisele, T. L. Cocker, M. A. Huber, M. Plankl, L. Viti, D. Ercolani, L. Sorba, M. S. Vitiello, and R. Huber. Ultrafast multi-terahertz nano-spectroscopy with sub-cycle temporal resolution. *Nature Photonics*, 8(11):841–845, 2014.

[183] Tyler L. Cocker, Vedran Jelic, Manisha Gupta, Sean J. Molesky, Jacob A. J. Burgess, Glenda De Los Reyes, Lyubov V. Titova, Ying Y. Tsui, Mark R. Freeman, and Frank A. Hegmann. An ultrafast terahertz scanning tunnelling microscope. *Nature Photonics*, 7(8):620–625, 2013.

[184] S. Morimoto, T. Arikawa, F. Blanchard, K. Sakai, K. Sasaki, and K. Tanaka. Observation and control of spoof localized surface plasmons using terahertz near-field microscope. In *41st International Conference on Infrared, Millimeter, and Terahertz waves (IRMMW-THz)*, pages 1–3, Sep. 2016.

[185] Ran Damari, Omri Weinberg, Daniel Krotkov, Natalia Demina, Katherine Akulov, Adina Golombek, Tal Schwartz, and Sharly Fleischer. Strong coupling of collective intermolecular vibrations in organic materials at terahertz frequencies. *Nature Communications*, 10(1):3248, 2019.

[186] Katsuaki Tanabe. Field enhancement around metal nanoparticles and nanoshells: A systematic investigation. *The Journal of Physical Chemistry C*, 112(40):15721–15728, 10 2008.

[187] K. Lance Kelly, Eduardo Coronado, Lin Lin Zhao, and George C. Schatz. The optical properties of metal nanoparticles: The influence of size, shape, and dielectric environment. *The Journal of Physical Chemistry B*, 107(3):668–677, 01 2003.

[188] Jianxun Liu, Huilin He, Dong Xiao, Shengtao Yin, Wei Ji, Shouzhen Jiang, Dan Luo, Bing Wang, and Yanjun Liu. Recent advances of plasmonic nanoparticles and their applications. *Materials (Basel, Switzerland)*, 11(10):1833, 09 2018.

[189] N. C. J. van der Valk and P. C. M. Planken. Electro-optic detection of subwavelength terahertz spot sizes in the near field of a metal tip. *Applied Physics Letters*, 81(9):1558–1560, 2002.

[190] Zhiping Jiang and X.-C. Zhang. Single-shot spatiotemporal terahertz field imaging. *Opt. Lett.*, 23(14):1114–1116, Jul 1998.

[191] C. Riek, D. V. Seletskiy, A. S. Moskalenko, J. F. Schmidt, P. Krauspe, S. Eckart, S. Eggert, G. Burkard, and A. Leitenstorfer. Direct sampling of electric-field vacuum fluctuations. *Science*, 350(6259):420–423, 2015.

[192] Abijith S. Kowligy, Henry Timmers, Alexander J. Lind, Ugaitz Elu, Flavio C. Cruz, Peter G. Schunemann, Jens Biegert, and Scott A. Diddams. Infrared electric field sampled frequency comb spectroscopy. *Science Advances*, 5(6), 2019.

Acknowledgements

I would like to take this as an opportunity to express gratitude to my friends and colleagues without whom I would not have been able to successfully finish my three-year work on the dissertation. These people and many of those who are not in the list below guaranteed one of the best working environments I have ever experienced. I am especially thankful to:

- Ferenc Krausz for giving me the opportunity to be a member of his big research group. Working in a such well-equipped and advanced lab is a dream for a young scientist.

- Nick Karpowicz for being an excellent supervisor and always ready to give me a hand in the lab and more. Without your brilliant ideas and precious advice, it would have been hard to achieve all the results.

- Matthew Weidman for supporting me and my goals as the new ATTO group leader. Your kind attention to every student made a positive and productive atmosphere in our small team.

- Enrico Ridente, Najd Altwaijry, Yik Long Li, Yang Cui and Ludwig Lorenz for being the coolest officemates. Constant fun and countless parties in the office and outside of it are unforgettable. I am surprised that we were able to find time for secondary things like work.

- Muhammad Qasim, Dmitry Zimin for being good friends and assisting me if needed. Our daily table tennis games with Enrico were an enjoyable distraction from the routine activities.

- Keyhan Golyari, Florian Siegrist, Julia Gessner, Marcus Ossiander, Martin Schultze and former members of Martin's research group for being helpful and all the time we spent together.

- Other colleagues with whom I took pleasure to communicate and be in close contact with in our institute: Vladislav Yakovlev, Clemens Jakubeit, Sambit Mitra, Hanieh Fattahi, Olga Razskazovskaya, Shawn Sederberg, Hadil Kassab and Simon Reiger.